The Dissertation Committee for Alexander John Headley Certifies that this is the approved version of the following dissertation:

Dynamic Modeling and Analysis of Proton Exchange Membrane Fuel Cells for Control Design

Committee:

Dongmei Chen, Supervisor

Joseph Beaman

Ofodike Ezekoye

Wei Li

Charles Mullins

Dynamic Modeling and Analysis of Proton Exchange Membrane Fuel Cells for Control Design

by

Alexander John Headley, BSME; MSE

Dissertation

Presented to the Faculty of the Graduate School of

The University of Texas at Austin

in Partial Fulfillment

of the Requirements

for the Degree of

Doctor of Philosophy

The University of Texas at Austin

May 2016

Acknowledgements

First off, I would like to thank my parents for being lifelong examples of the power and importance of higher education. Thank you both for raising us all to know that we can do anything we work hard for, and that dreams are worth chasing. I also have to thank my brothers Jon and Aaron for being supportive this whole time and for sparking my scientific curiosity from a young age. Some of the fondest memories I have are of us taking apart all of our toys to see how they work, putting them back together (or at least trying to), making parachutes out of bed sheets, and designing jets that we could build at home using aerosol cans for fuel injectors (not bad, but I think we grossly underestimated the thermal issues).

I'd also like to thank all of the students that I have taught throughout my time here. My interactions with all of you motivated me to keep going when it felt like it just might not be worth it. I also have to thank the UT Austin community. This university has given me so many great experiences, exposed me to so much knowledge, and connected me to many lifelong colleagues and friends.

Most importantly, thanks to my beautiful, in every sense of the word, wife Hannah, for everything she has done for me over the years. It is a difficult thing to move across the country, away from your family, friends and the place that you have called your home for most of your life with no real knowledge of the area you are going to or even having visited your new city. All of this is that much more difficult when it is not even for *your* dream. Thank you for your relentless commitment to teaching, for keeping me grounded, and for all the funny stories from your classroom. Thank you Hannah for supporting me throughout this adventure, and for being with me for all the others that we have and will share.

Thank You Jesus.

Dynamic Modeling and Analysis of Proton Exchange Membrane Fuel Cells for Control Design

Alexander John Headley, PhD

The University of Texas at Austin, 2016

Supervisor: Dongmei Chen

This dissertation seeks to address a number of issues facing the advancement of Proton Exchange Membrane (PEM) fuel cell technology by improving control-oriented modeling strategies for these systems. Real-time control is a major ongoing challenge for PEM fuel cell technologies, particularly with regards to water and temperature dynamics. This can lead to a number of operational concerns, such as membrane flooding and dehydration, which can seriously diminish the efficiency, reliability, and long term health of the system. To combat these issues, comprehensive models that are capable of capturing the dynamics of the key operating conditions and can be processed in real time are needed. Also, given the inherently distributed nature of the system, such a model would ideally account for the changes in the conditions from cell-to-cell in the stack, which can be very significant.

With this goal in mind, the main focus of this dissertation is the development and experimental validation of control-oriented modeling techniques for PEM fuel cell stacks. The first major work in this study was the verification of a relative humidity model in response to varying loads. Through this work, a multiple control volume (CV) approach was developed and experimentally validated to model the distribution of operating

conditions more accurately while keeping the computational expense sufficiently low. To optimize the modeling efforts, further analysis of the temperature and vapor distribution was performed starting from first principles. This led to the creation of various techniques to optimally size CVs based on the parameters and operating conditions of the system in question. Finally, it was noted throughout the testing that the performance of the membrane electrolyte assemblies in the test stack declined significantly from their initial state. To compensate for this, a Kalman filter was implemented to quantify the membrane degradation. SEM analysis of membranes from the test stack confirmed the validity of this technique. This work can be used to significantly improve real-time models for PEM fuel cells for model-based control applications.

Table of Contents

List of Tables x

List of Figures xi

Chapter I: Introduction 1

Literature Review 7

Cathode Channel Flooding and Water Transport 7

Membrane Aging Effects in Fuel Cells 10

Research Objectives 12

Chapter II: Distributed Dynamic PEM Fuel Cell Model for Control Design 14

Modeling Methodology 14

Mass Conservation 16

Relative Humidity and Water Transport 17

Water transport by electro-osmotic drag 18

Water transport due to osmotic diffusion 19

Stack Voltage 20

Activation Loss 21

Ohmic Loss 21

Model Tuning and Experimental Setup 22

Cross Flow Experiments and Modeling 25

One CV and Multi-CV Model Comparisons 31

Stack Voltage Model Calibration 35

Model Validation Test 38

Distributed Simulation Results 41

Summary 45

Chapter III: PEM Fuel Cell Thermal Model Scaling and Modeling Implications 47

Motivation 47

Energy Equation and Scaling Arguments 50

Agreement with the Simulink Model and Potential CV Sizing Results 55

Thermal Scaling Study Implications 58

Reducing the Order of the Distributed Model 59
Original Multi-CV Thermal Modeling Methodology.....60
Modified Modeling Methodology.....61
Simulation Results and Discussion.....65
Computational Expense Reduction.....67
Chapter IV: Analysis of the Relative Humidity Profile in the Cathode Channel ..69
Motivation.....69
Methodology.....70
Concentration Gradient Based Vapor Diffusion.....73
Current Dominated Vapor Diffusion and Generation.....75
Final RH Profile Solution 77
Analytical Modeling Results.....78
Effect of Varying Various Inputs.....81
Sizing Methodology Using the RH Profile.....84
Defining a Correction Factor for Fully Lumped Model to Accurately Predict Flooding Conditions.....87
Equations for Adjustment 88
Summary.....91
Chapter V: Individual Membrane Voltage Response and Drive Cycle Experimental Validation 93
Motivation.....93
Standard Drive Cycle Tests 95
Individual Cell Voltage Model Tuning.....98
Extended Kalman Filter for Fuel Cell Membrane Parameters.....103
General Extended Kalman Filtering Algorithm.....104
Extended Kalman Filtering Algorithm for Membrane State Estimates.....106
Modification of the EKF for Additional Membrane State Estimates.....109
HWFET EKF Tuning Results.....111
FTP-75 EKF Tuning Validation 114

EKF State Estimation Discussion and Aging Differences Between Cells 116
Ex-Situ Membrane Health Verification 122
Chapter VI: Conclusions 128
Control Oriented Fuel Cell Model Development and Validation 129
System Analysis and Model Optimization 130
EKF Membrane State Estimations 132
Future Work 134
Dynamic System Modeling 134
Membrane State Estimates and Prognostics 135
References 137
Vita 145

List of Tables

Table 1: Experimental Fuel Cell Stack Dimensions 24

Table 2: Relative Humidity and Voltage Error Calibration Test (0-8.5A) 38

Table 3: Relative Humidity and Voltage Error Validation Test (0-15A) 40

Table 4: Control Volume Temperature Predictions using the Simulink Model and Simplified Equation Approximation 55

Table 5: Critical Lengths, Low Flow, ΔT=35K 56

Table 6: Critical Lengths, Low Flow, ΔT=10K 57

Table 7: Critical Lengths, High Flow, ΔT=35K 58

Table 8: Modeling time for each model iteration 68

Table 9: Specifications for the standard vehicle used to represent 96

Table 10: FTP-75 Test Stack Inlet Conditions 98

Table 11: Voltage Model Error Using Different Tuning Methods 116

List of Figures

Figure 1: PEM Fuel Cell Schematic [5].....3

Figure 2: Representative control volumes of a fuel cell stack (CV1: Fuel Cell Body & MEA, CV2: Anode, CV3: Cathode, CV4: Coolant Water) 14

Figure 3: The 2 kW PEM fuel cell stack used for model validation.....24

Figure 4: Measured pressure vs. mass flow rate – full system 26

Figure 5: Measured pressure vs. mass flow rate – sensor housings only 27

Figure 6: Calculated mass flow rate vs. pressure drop– stack only.....28

Figure 7: Representative pressure for a one CV model 29

Figure 8: Representative pressure for a four CV model 29

Figure 9: Mass flow rate vs. pressure for a one CV model.....30

Figure 10: Mass flow rate vs. pressure for a six CV model.....31

Figure 11: Experimental and modeled relative humidity response with one CV model - Calibration Test 32

Figure 12: A comparison of relative humidity responses between experiment and a six CV model - Calibration test.....33

Figure 13: One and six CV model RH response comparison 35

Figure 14: Experimental and six CV model voltage responses before tuning.....36

Figure 15: Experimental and one CV model voltage responses 37

Figure 16: Experimental and six CV model RH responses in a validation test.....39

Figure 17: Experimental and six CV modeled voltage responses in a validation test 39

Figure 18: Experimental and six CV modeled voltage responses in a validation test 40

Figure 19: Relative Humidity along the cathode Channel Length (1=Inlet; 6=Outlet) Calibration Test 41
Figure 20: Voltage Response from Selected CVs and Stack Average Calibration Test 42
Figure 21: Pressure Response along Cathode Channel Calibration Test 43
Figure 22: Relative Humidity along Channel Length (1=Inlet; 6=Outlet) Validation Test 44
Figure 23: Voltage Response from Selected CVs and Stack Average Validation Test 45
Figure 24: Pressure Response along Cathode Channel Validation Test 45
Figure 25: Modeled and Experimental Voltage Step Load Test 47
Figure 26: Individual Cell Performance during the Validation Test 48
Figure 27: Proposed Thermal Modeling Schematic 50
Figure 28: Conceptual Determination of Control Volume Sizes 54
Figure 29: Relative Humidity Response Single Temperature CV Model (Left) Individual Temperature CVs Model (Right) 65
Figure 30: Distributed Relative Humidity Response Single Temperature CV Model (Left) Individual Temperature CVs Model (Right) 66
Figure 31: Voltage Response Single Temperature CV Model (Left) Individual Temperature CVs Model (Right) 66
Figure 32: Distributed Voltage Response Single Temperature CV Model (Left) Individual Temperature CVs Model (Right) 67
Figure 33: Representative control volumes of a fuel cell stack (CV_1: Fuel Cell Body & MEA, CV_2: Anode, CV_3: Cathode, CV_4: Coolant Water) [76] 69

Figure 34: Linearization of the membrane water content with respect to the vapor activity; $0<a_i\leq 1$ 74
Figure 35: Linearization of the electro-diffusion coefficient with respect to the membrane water content 76
Figure 36: Analytical Profile and Simulation comparison of calculated RH in 6 evenly spaced CVs (T_{FC} = 345.77K, 3A demand, *RH,an* = 89.95%, *RH,in*=70%, 5 Lpm inlet flow rate) 79
Figure 37: Analytical Profile and Simulation comparison of calculated RH in 6 evenly spaced CVs (TFC = 347.75 K, 5 A demand, RH,an = 88.2%, RH,in = 70%, 10 nLpm inlet flow rate) 80
Figure 38: Analytical Profile and Simulation comparison of calculated RH in 6 evenly spaced CVs (TFC = 351.12 K, 10 A demand, RH,an = 90.1%, RH,in = 70%, 15 nLpm inlet flow rate 80
Figure 39: Analytical profile response to varying current demands (T_{FC} = 348.15 K, *RH,in* = 70%, Inlet Flow =15 nLpm) 82
Figure 40: Analytical profile response to varying the cathode inlet flow rate (T_{FC} = 348.15 K, *RH,in* = 70%, Ist = 10 A) 82
Figure 41: Analytical profile response to varying the cathode inlet relative humidity (T_{FC} = 348.15 K, I_{st} = 10 A, Inlet Flow = 15 nLpm) 83
Figure 42: Unevenly spaced CV sizing algorithm results (T_{FC}=352K, 7A demand, RH,an = 90%, RH,in=70%, 15nLpm inlet flow rate) 86
Figure 43: Unevenly spaced CV sizing algorithm results (T_{FC}=345.77K, 3A demand, RH,an = 89.95%, RH,in=70%, 5nLpm inlet flow rate) 86
Figure 44: Experimental validation of the one CV model adjustment algorithm – Max load test phase.....89

Figure 45: Experimental validation of the one CV model adjustment algorithm – No load pre-test 91
Figure 46: FTP-75 Speed Profile (Blue) and Scaled Power (Red) 97
Figure 47: HWFET Speed Profile (Blue) and Scaled Power (Red) 98
Figure 48: FTP-75 Stack Voltage Response No Tuning 99
Figure 49: FTP-75 Cell #8 Voltage Response No Tuning 100
Figure 50: FTP-75 Cell #2 Voltage Response No Tuning 100
Figure 51: FTP-75 Stack Voltage Response c1=76 & K_{ohm}=3.35 101
Figure 52: FTP-75 Cell #8 Voltage Response c1=76 & K_{ohm}=3.35 102
Figure 53: FTP-75 Cell #2 Voltage Response c1=76 & K_{ohm}=3.35 102
Figure 54: HWFET Voltage Response During the EKF Tuning Process 112
Figure 55: HWFET Voltage Response During EKF Tuning Cell #2 113
Figure 56: HWFET Voltage Response During EKF Tuning Cell #8 113
Figure 57: EMSA EKF Tuning During HWFET test cycle 114
Figure 58: FTP-75 Stack Voltage Response After HWFET EKF Tuning 115
Figure 59: EMSA EKF Tuning During FTP-75 Test Cycle 117
Figure 60: Voltage Dynamics During Fast Load Changes in the FTP-75 Test 119
Figure 61: Final EMSA Estimations From the HWFET and FTP-75 Tests 120
Figure 62: Cell 8 Anode Catalyst Overview 1.50k Magnification 123
Figure 63: Cell 1 Anode Catalyst Pitting 15.0k Magnification 123
Figure 64: Cell 1 SE and BSE Image Comparison 90k Magnification 124
Figure 65: Cell 2 SE and BSE Image Comparison 90k Magnification 124
Figure 66: Cell 8 SE and BSE Image Comparison 90k Magnification 125
Figure 67: Cell 1 SE and BSE Image Comparison 180k Magnification 125
Figure 68: Cell 2 SE and BSE Image Comparison 180k Magnification 126

Figure 69: Cell 8 SE and BSE Image Comparison 180k Magnification 126
Figure 70: Cell 8 (Left) and Cell 2 (Right) SE Comparison 450k Magnification127

Chapter I: Introduction

In recent years, hydrogen has attracted interest in the search for cleaner, more sustainable sources of energy to replace fossil fuels. Hydrogen can be produced domestically from a number of sources, thereby reducing the dependence on fossil fuel imports. It is also an exceptionally clean fuel, which produces no greenhouse gases (GHGs) or NOx emissions when used in low temperature power generating devices. To complement the versatility of hydrogen as a fuel, proton exchange membrane (PEM) fuel cells have been extensively researched in both academia and industry. Their fast response times to load changes, high efficiency, and scalability make them an ideal technology for a wide range of applications [1].

Fuel cells are electrochemical devices that utilize the potential of the water formation reaction to generate electrical power. Figure 1 shows a schematic of a PEM fuel cell. Either pure oxygen or air is fed into the cathode of the fuel cell, while hydrogen is fed into the anode. Catalysts are used to break down the molecules and drive the following reactions:

Anode:

$$H_2 \rightleftarrows 2H^+ + 2e^- \tag{1}$$

Cathode:

$$\frac{1}{2}O_2 + 2H^+ + 2e^- \rightleftarrows H_2O \tag{2}$$

Overall:

$$H_2 + \frac{1}{2}O_2 \rightleftarrows H_2O \quad (3)$$

Specialized membranes that only allow protonic current flow are used, such that the electrons must pass through an external circuit to complete the reaction, thereby supplying power to the external circuit. The load in the external circuit can be any electrically powered device, which makes PEM fuel cells versatile power generation sources. For instance, fuel cells have the potential for considerably higher energy densities than conventional Li-ion battery technologies, positioning them as good candidates for powering portable electronic devices [2]. They have also been extensively investigated for the transportation sector and distributed power generation applications because of their unique qualities [3]. For vehicles, hydrogen powered PEM fuel cells are one of the few clean energy sources that can provide similar performance, range, and refill times to conventional internal combustion engine (ICE) vehicles [4]. As such, a number of automotive manufacturers, including Honda, Toyota, GM, and Hyundai have created demonstration fleets of fuel cell vehicles over the last decade and exclusively research PEM fuel cells versus other fuel cell technologies because of their high power density and quick dynamic response [3].

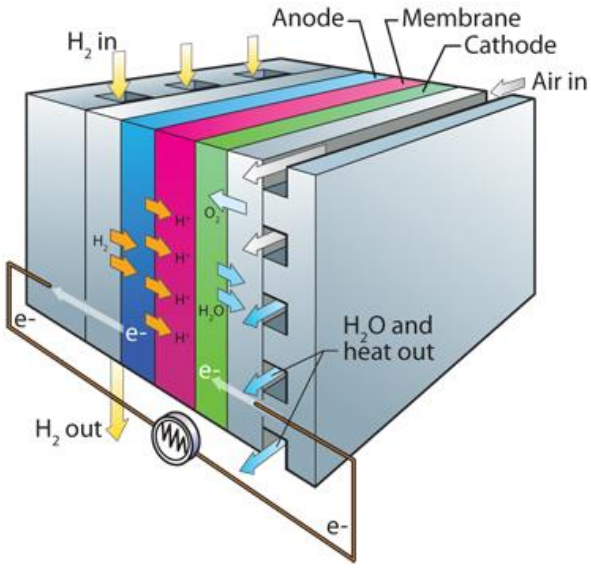

FIGURE 1: PEM FUEL CELL SCHEMATIC [5]

PEM fuel cells have marked advantages as compared to battery powered electric vehicles (EVs). For instance, range anxiety is often cited as a major hindrance to widespread EV adoption [6, 7] as many consumers are concerned about the limited range of EVs and the lack of a public EV charging network to alleviate these concerns. In the event that an EV charging infrastructure is established, there are still concerns regarding charge times for EVs, which can range from 30 minutes with rapid charging technologies, up to 10 hours or more with the conventional, stage 1 charging systems [8]. By contrast, fuel cell electric vehicles (FCEVs) can provide a comparable range to ICE vehicles and be refilled quickly. In fact, Hyundai claims that their new 2015 Tucson fuel cell SUV can refill from completely empty in approximately 10 minutes and has an EPA rated, 265 mile range [9], which is large enough to alleviate most range concerns.

PEM fuel cells are also well-suited for distributed power generation needs because they respond quickly to load changes, can operate efficiently at partial loads, and are easily

scalable to fit various grid requirements [10]. Additionally, they operate quietly, cleanly, and with few moving parts, making them ideal for residential installations [11]. With proper planning, they can also be used in combined heat and power (CHP) configurations, in which case the system efficiency can exceed 80% [12]. Their ability to quickly change their power output makes them a good addition to systems using high levels of intermittent power generation sources, such as solar or wind power. With proper development and advancement of the technology, fuel cells could play an important role in the future of islanded microgrids and backup power generation applications.

However, while research and development of PEM fuel cells has advanced significantly in the past few decades, there are significant technical hurdles that must be addressed before the technology can reach its full potential and market viability. Most of these challenges can be categorized into three major areas: the hydrogen infrastructure, system cost, and robustness.

The lack of a comprehensive hydrogen fueling network is a significant hindrance to the proliferation of PEM fuel cell technologies, particularly in the transportation sector. Though the charging infrastructure for EVs needs to be expanded to alleviate range anxiety [13], the range capabilities of FCEVs are not currently advantageous, as the number of hydrogen fueling stations is extremely limited. However, there are a number of developments in progress to expand the availability of hydrogen fuel. In California, they have slated $20 million to construct the “Hydrogen Highway”, which would facilitate travel between San Francisco and Los Angeles [14, 15] using only hydrogen fuel. In support of this initiative, and to advance the FCEV economy, both Honda and Toyota

announced that they would provide financial assistance to FirstElement Fuel to build more fueling stations in California (totaling almost $30 million in investments) [16, 17]. Toyota is also funding the installation of 12 hydrogen fueling stations throughout the Northeastern US [17]. These installations will significantly expand the hydrogen fuel infrastructure from its current level and serve as good case studies for future developments. This brings the focus to the last two areas of concern with PEM fuel cells, the cost and robustness of the systems.

The proton exchange membranes are the most expensive components in fuel cell systems as they use precious metals (typically Pt) to catalyze the electrode reactions. Presently, the high Pt loading in the membranes is cost prohibitive, and large-scale fuel cell manufacture could potentially lead to a worldwide platinum shortage [18]. In response to this issue, extensive research has been undertaken to reduce the Platinum loading in the catalysts [19]. However, the membranes are not the only expensive component of the system; the control systems can also be rather costly. Numerous sensors and complex control schemes are currently required because the dynamics of the system are not entirely understood, particularly with regard to the humidification levels. As a result, the sensors and controller represent a significant portion of the balance-of-plant cost [20]. To reach the target cost of $40/kW to be competitive with modern ICE vehicles, the cost of both the membranes and balance-of-plant needs to be reduced [21].

Robustness is also a major hindrance in terms of the control stability, long-term health of the components, and maintenance costs. Water management is frequently cited as an extremely important aspect of fuel cell control [22, 23, 24], but to date, no fully

satisfactory, stack-level control schemes have surfaced because of the lack of understanding of the physical phenomena. Both externally humidified and dry gas operation schemes have been pursued, but these approaches have led to conflicting issues [25]. With externally humidified control schemes, the objective has classically been to maximize the protonic conductivity of the membrane, and therefore high humidity inlet gas streams have been used. However, this leads to flooding issues in the stack, which blocks activation sites in the catalyst layer and significantly reduces efficiency. Dry gas operation has also been investigated to circumvent the flooding concerns, but this has been shown to lead to relatively poor performance [26, 27, 28] as low humidity operating conditions reduce the protonic conductivity and increase the ohmic overpotential losses. Therefore, a clear motivation exists to finely control the humidity in the fuel cell stack to optimize the performance and avoid flooding issues in the stack.

The operating conditions also have major implications on the long-term health of the membranes, which is one of the largest barriers to widespread commercialization of PEM fuel cells [29, 30]. Membrane failure rates are highly dependent on the operating conditions (e.g. humidity and temperature) as these greatly affect the mechanical properties of the membrane [31, 32, 30]. Additionally, low humidity conditions can result in the formation of membrane hotspots, which can quickly lead to permanent damage [33]. Given the high cost of the membranes, replacements/maintenance operations would represent a significant operational cost and need to be minimized.

LITERATURE REVIEW

Cathode Channel Flooding and Water Transport

As previously mentioned, a crucial challenge facing PEM fuel cell technologies is stack water management in response to varying inlet and load conditions. With high relative humidities and current demands, the gas diffusion layer (GDL) in a PEM fuel cell is prone to flooding because of the water generated from the electrochemical reaction [34, 35, 36]. Flooded channels can cause significant drops in cell voltage, thereby lowering the overall fuel cell stack efficiency [37].

However, humidity control in PEM fuel cells is challenging because of the interactions between the operating temperature, RH, electrochemical reactions, and mass transport phenomena in the system. The inlet gas conditions, cell temperature, current demand, and cooling system all significantly affect the water vapor content in the stack [38, 39]. Additionally, the humidity levels can vary significantly along the length of the channel, depending on the demand and flow conditions. This issue is more pronounced for multi-cell stacks, where the spatial variations in the operating conditions can be considerable. To understand and properly control membrane humidification in real time, an accurate, low-order, dynamic fuel cell model that can accurately capture variations in vapor content along the stack is needed.

There are three major sources of water flux to the cathode channel of a PEM fuel cell in addition to the bulk flow: 1) electro-osmotic drag from the anode channel, 2) back diffusion, and 3) water that is produced from the electrochemical reaction [40]. Electro-

osmotic drag results from water molecules being dragged through the membrane from the anode to the cathode along with the protons that complete the oxygen reduction reaction in the cathode. As such, the risk of flooding in the cathode increases with the demanded current because this increases both the electro-osmotic drag flux and water generation rate. This issue can be alleviated by back diffusion, diffusion driven by the concentration gradient between the anode and cathode channels, but the combined effects of electro-osmotic drag and water generation tend to dominate, leading to flooding concerns [33].

To properly model the humidification dynamics in the stack, all of these water transport effects need to be accounted for. Modeling of these effects will be discussed in Chapter II.

A number of multi-dimensional PEM fuel cell models have been developed to predict the distributions of reactant species, power density, and liquid formation using computational fluid dynamics (CFD) methods. Many of these models have achieved good agreement with experimental data and been used to improve the understanding of localized phenomena in the gas diffusion layer and channels [41, 42, 43, 44, 45, 46, 47]. For instance, You et al. developed a two-dimensional (2D), two-phase flow model to predict the water transport phenomena in a fuel cell [46]. The study included the determination of limiting current densities to avoid liquid formation in the cathode channel. However, this model and other similar models are limited to steady state considerations. While there are multi-dimensional models that can be used to predict transient behavior [47], in general CFD models are well-suited for design analysis but are far too computationally intensive to implement in real-time controllers.

Nevertheless, these high order models do have implications for control design purposes that should not be ignored. Most notably, they show that the operating conditions can change significantly along the length of the stack and offer valuable insight into the spatial variations seen in PEMFCs. The distribution in the humidity levels along the length of the stack has also been corroborated by experimental results. Weng et al. ran a series of experiments with a specialized PEM cell that allowed them to independently measure the output from 8 segments in series from the inlet to the outlet [48]. These experiments clearly show that the increase in humidity from the inlet to the outlet that occurs due to the water generated as a result of the applied load significantly alters the response from each segment, even within a unicellular system. This effect increases as more cells are added in series, leading to a larger difference in the humidification levels from the inlet to the outlet of the stack. These results imply that the distributions in the system, particularly those of the humidity levels, are sufficiently large so as to necessitate consideration when developing low-order models. The need for such considerations will be discussed further and shown in Chapter II.

For real-time control considerations, several reduced-order models have been developed to describe the transient dynamics of PEM fuel cells [49, 50, 51, 52, 53, 54, 55]. Rather than using multi-dimensional representations of the fuel cell, these models instead use a small number of lumped control volumes to represent various sections of the stack. In this way, the computational expense can be drastically reduced as compared to highly discretized, CFD models. Several of these studies have performed experimental validation

of their models and reported good agreement with the temperature and stack voltage responses of the systems [52, 54, 55].

Del Real et. al, developed a dynamic, control-oriented model that simulated the voltage, temperature, and liquid water flooding effects in the anode for an air-cooled, Ballard PEM fuel cell [52]. While they did experimentally validate the voltage and temperature response of their model, they were concerned with anode flooding in dead ended operation scenarios and ignored the potential for flooding concerns in the cathode channel. However, many studies cite cathode flooding as being the main source of concern [23, 56, 48]. Also, as is the case with all of the published PEM fuel cell reduced order models, no experimental validation of the humidity dynamics was performed, and no consideration was given to the spatial variations in the operating conditions.

Though lumped models are well-suited to control design, an inherently distributed system cannot be accurately represented with a lumped model without additional treatment. This additional treatment has not been performed before for PEM fuel cell models in a manner that can still be used for control design, and is the main goal of this research.

Membrane Aging Effects in Fuel Cells

Through the course of this research, it was found that the performance of the membranes used for experimental validation degraded significantly from their un-aged capabilities. This necessitated extensive re-tuning of the model to match the observed stack output, and demonstrates the need for membrane aging considerations for long-term deployments of PEM systems. The mechanisms of membrane aging in fuel cells are a topic

of ongoing research in the PEM fuel cell community as early membrane failures would lead to major expenditures for any sustained fuel cell operations. There are many factors that accelerate the degradation of PEMs, many of which are directly tied to the operating conditions of the membranes (i.e. load cycling, temperature, RH, etc.) [57]. In particular, multiple studies have shown that membrane dehydration can cause hot spots and irreparable damage to the membrane itself [38, 58, 59]. It has also been shown that repeated cycling between wet and dry conditions can cause significant mechanical stresses that can be responsible for early failures as well [57].

Given these issues, again we see that control of humidity levels is crucial to the performance and health of PEM fuel cell stacks. Ideally, the relative humidity (RH) should be held just below 100% across the entire stack at all times to minimize ohmic losses and membrane damage while avoiding membrane flooding. However, because the RH changes along the length of the channel with the current, which is a system disturbance, it is not possible to satisfy this condition for every cell in the stack. As a result, membranes within a multi-cellular stack will likely all age at different rates, as the inlet cells being the most problematic do not benefit from the passive humidification from the product water as cells further down the stack length do. This needs to be considered to create control strategies that are truly optimal for the overall performance and health of the stack.

Another aspect of membrane aging that has not been heavily researched with regards to long term control implementation is the decline in the voltage output with time. Though mechanisms have been identified for the degradation of the catalyst and the resulting voltage loss [57], no correlations currently exist that can be implemented with

any real-time control strategies. As such, predetermined operating points and control decisions based on new systems may become unfeasible as the system ages. This could lead to instabilities in real operations. An Extended Kalman Filter (EKF) method to dynamically update the model to account for degradation is discussed in Chapter V.

Though there are other studies that have used Kalman filters for PEM fuel cell applications, none have investigated physical membrane parameters on an individual cell basis or provided experimental validation of the effectiveness of the filter. Many of these studies have used filters for water level and flooding predictions [60, 61, 62]. Others have investigated Kalman filters to tune general stack impedance parameters and also generally assume a known and consistent load profile [63, 64, 60]. Zhang et al [65] used a UKF implementation to estimate the effective membrane surface area degradation of a fuel cell stack. They used this information to inform a prognostics model. However, this work did not include actual experimental data, and assumed that a consistent prescribed load profile was used. Furthermore, they did not consider differences in aging between cells in the stack.

RESEARCH OBJECTIVES

Based on the literature survey, one can see that there is a clear need to improve the understanding of real-time variations in PEM fuel cell operating conditions. This research seeks to target the cost and robustness concerns associated with the humidity dynamics by:

i. Developing a comprehensive, control-oriented PEM fuel cell model that can accurately predict the operating condition fluctuations in real time, particularly the humidity level.

ii. Experimentally validating the multi-CV model to fill the gap of data regarding RH dynamics in the literature.
iii. Improving the understanding of the onset of flooding phenomena through an analytical study of the vapor distribution in the stack.
iv. Implementing a filtering technique to track membrane aging effects within the fuel cell stack.

This research effort would lead to a number of improvements over the current control paradigms. With a higher degree of confidence in the modeling accuracy, control could be performed with fewer sensors to reduce the balance of plant cost. A controller based on this model could potentially be used to simultaneously avoid flooding and dehumidification issues, thereby greatly improving the efficiency and robustness of operation as well as reducing the long-term aging effects associated with poor humidity control.

Chapter II: Distributed Dynamic PEM Fuel Cell Model for Control Design[1]

MODELING METHODOLOGY

The model developed for this study is an extension of a previously validated dynamic thermal model [66, 67]. The physics-based model used to describe the transient response of a PEM fuel cell, utilizes four basic CVs as shown in Figure 2. The four basic CVs used in the model are the anode channel, cathode channel, fuel cell body, and coolant channel. The membrane electrolyte assembly (MEA) is included in the fuel cell body CV.

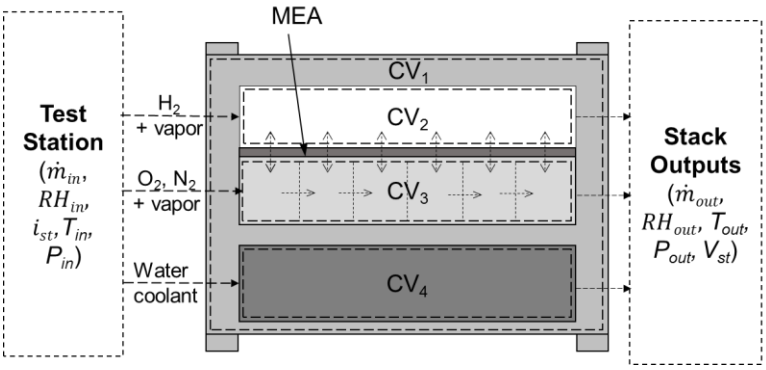

FIGURE 2: REPRESENTATIVE CONTROL VOLUMES OF A FUEL CELL STACK (CV1: FUEL CELL BODY & MEA, CV2: ANODE, CV3: CATHODE, CV4: COOLANT WATER)

In Figure 2, *T* and *P* represent temperature and pressure respectively in each CV. The states in each CV are calculated based on the conservation of energy and mass. The known inputs to the fuel cell stack from a test station are inlet flow rates, RH, pressures

[1] Some of the work in this chapter has been published in the IEEE Journal of Mechatronics: Headley, A., Yu, V., Borduin, R., Chen, D., & Li, W. (2015). Development and Experimental Validation of a Physics-based PEM Fuel Cell Model for Cathode Humidity Control Design.

and temperatures for each CV, and current demand. The outputs of this system are the temperatures of each channel, RH of the anode and cathode channels, and stack voltage. Gases in the system are assumed to follow the ideal gas law. A complete description of the energy and mass conservation equations is provided in reference [66], and will not be shown in its entirety here. The following discussion in this chapter will focus predominantly on the water mass conservation equations for the system. The energy conservation equations used to model the system temperature will be presented and analyzed in Chapter III.

A better understanding of the RH distribution along the channels is necessary to accurately model the system. However, expanding the model to incorporate a highly discretized one-dimensional (1D) representation of the channels would be computationally expensive and ill-suited for real-time control development. To improve the fidelity of the model while limiting additional computational complexity, the basic cathode channel CV (CV_3) is further sub-divided into a series of smaller, lumped sub-volumes. The cathode was chosen for further discretization because it was the focus of the experimental validation and is typically the greater concern for water management in PEM fuel cell stacks [68], as mentioned previously. While further accuracy could be obtained by discretizing the anode channel (CV2) as well, it was found that this was not necessary to obtain accurate experimental agreement, as will be shown in the following sections.

The number of sub-volumes used to describe the cathode can be chosen based on the desired modeling accuracy and computational expense. Previous work showed that the

use of six sub-volumes offered a good balance of accuracy and computational expense for our system [67].

Mass Conservation

Tracking the concentrations of various species in each CV is important to accurately model the system. In the anode, the species considered are hydrogen and water that enters the channel, either from a humidifier or by diffusion through the membrane. In the cathode, oxygen, nitrogen, and water are all present. Mass conservation is applied to each CV as follows.

$$\frac{dm_k}{dt} = \dot{m}_{k,gen} - \dot{m}_{k,reac} + \sum \dot{m}_{k,in} - \sum \dot{m}_{k,out} \tag{4}$$

where m represents the mass, k denotes the type of species, and the subscripts *gen*, *reac, in,* and *out* refer to generated, reacted, inlet, and outlet species, respectively. The species' reaction and generation rates are functions of the electrical current.

The mass flow rates of the species into and out of each CV are due to bulk flow along the length of the channel, and in the case of water vapor, transport through the MEA. For a fully lumped cathode channel model, the inlet flow rate is a known input from the test station, and the outlet flow rate is calculated from an empirical correlation relating the difference between the CV pressure and the outlet pressure to the mass flow rate.

To extend this concept to six CVs, thereby capturing the distributed nature of the system, the modeling equations were modified. For the first CV (CV_1), the inlet flow is a known measurement from the test station. However, the outlet flow rate is a function of the difference in pressure from CV_1 to CV_2. For all subsequent CVs, the inlet flow is

equivalent to the outlet flow of the previous CV, and the outlet flow is a function of the drop in pressure from the current CV to the following CV, or the outlet manifold in the case of CV_6:

$$\begin{aligned} \dot{m}_{in,k,CVj} &= \dot{m}_{out,k,CVj-1} \\ \dot{m}_{out,CVj} &= \dot{m}_{out,CVj}\left(\Delta P_{j\rightarrow j+1}\right) \end{aligned} \tag{5}$$

Individual specie flow rates are then calculated by multiplying the mass fraction of the specie in the CV by the total mass flow rate. The correlations relating the pressure drop to the mass flow rate, and the associated tests to obtain them will be discussed in the following section.

Given the mass flow rates of each specie in to and out of each CV, the species masses can be calculated dynamically by solving Eqn. (4).

Relative Humidity and Water Transport

Relative humidity is directly related to the saturation pressure in the CV. The following fourth-order empirical relation is used to obtain the saturation pressure from the CV temperature [53]:

$$\begin{aligned} log_{10}\left(P_{sat}\right) = &\text{-}1.69\times10^{\text{-}10}T^4 + 3.85\times10^{\text{-}7}T^3 \\ &\text{-}3.39\times10^{\text{-}4}T^2 + 0.143T - 20.92 \end{aligned} \tag{6}$$

where P_{sat} is the saturation pressure and T is the CV temperature. From the saturation pressure, the ideal gas law is used to calculate the saturation mass:

$$m_{sat} = \frac{P_{sat}V}{RT} \tag{7}$$

where m_{sat} is the saturation mass, R is the ideal gas constant, and V is the volume of the CV.

The mass conservation equation represented by Eqn. (4), in conjunction with the vapor transfer models, is used to dynamically compute the mass of water in each CV. If the mass of water in a given CV is less than the saturation mass, all of the water is considered to exist in the vapor phase. Any water mass in excess of the saturation limit is considered to exist in the liquid phase. Once the mass of water in the CV is determined the RH can be calculated as

$$RH = \frac{m_{vap}}{m_{sat}} \tag{8}$$

where m_{vap} is the vapor mass in the CV. Water transferred through the MEA also affects the RH dynamics in each CV. Water is transported through the membrane mainly by two phenomena: 1) electro-osmotic drag and 2) osmotic diffusion.

Water transport by electro-osmotic drag

Electro-osmotic drag arises as hydrogen ions drag water molecules through the membrane as they propagate from the anode channel to the cathode channel. This process can be modeled using the following equation [53]:

$$\dot{N}_{electro} = n_d \frac{i}{F} \tag{9}$$

where $\dot{N}_{electro}$ is the molar flow rate of water molecules due to electro-osmotic drag, n_d is the electro-osmotic drag coefficient for the membrane and i is the current density.

The electro-osmotic drag coefficient is determined from the following empirical equation [53].

$$n_d = 0.0029\lambda_m^2 + 0.05\lambda_m - 3.4\times10^{-19} \tag{10}$$

where λ_m is the membrane water content given by [53].

$$\lambda_m = 0.043 + 17.81a_m - 39.85a_m^2 + 36.00a_m^3 \tag{11}$$

where a_m is the RH in the membrane. For this study, the membrane RH is assumed to be the average of the anode and cathode relative humidities.

Water transport due to osmotic diffusion

Diffusion through the membrane also occurs due to disparities in water concentration between the anode and cathode channels. This osmotic process is governed by the following equation [69]:

$$\dot{N}_{diffusion} = D_w \frac{c_{v,ca} - c_{v,an}}{t_m} \tag{12}$$

Here $\dot{N}_{diffusion}$ is the molar flow rate of water molecules due to diffusion, D_w is the vapor diffusion coefficient, t_m is the thickness of the membrane, and $c_{v,ca}$ and $c_{v,an}$ are the concentrations of water in the anode and cathode channels defined as [53]

$$c_{v,an} = \frac{\rho_{m,dry}}{M_{m,dry}} \lambda_{an} \tag{13}$$

$$c_{v,ca} = \frac{\rho_{m,dry}}{M_{m,dry}} \lambda_{ca} \tag{14}$$

where $\rho_{m,dry}$ and $M_{m,dry}$ are the membrane dry equivalent density and equivalent weight, respectively. The water contents of the anode and cathode channels are λ_{an} and λ_{ca},

respectively, which can be calculated using Eqn. (11) by replacing a_m with the activity of the respective channel. The vapor diffusion coefficient is also a function of the membrane activity, and is determined using the following equation [70]:

$$D_w = D_\lambda \, exp\left(2416\left(\frac{1}{303} - \frac{1}{T_{cell}} \right) \right) \tag{15}$$

where T_{cell} is the fuel cell body temperature and D_λ is

$$D_\lambda = \begin{cases} 10^{-10} & \lambda_m < 2 \\ 10^{-10}\left(1+2\left(\lambda_m - 2\right)\right) & 2 \le \lambda_m \le 3 \\ 10^{-10}\left(3-1.67\left(\lambda_m - 3\right)\right) & 3 < \lambda_m < 4.5 \\ 1.25\times 10^{-10} & \lambda_m \ge 4.5 \end{cases} \tag{16}$$

Equations (12)-(16) were incorporated into the fuel cell thermal model that was previously developed by the authors [66] to simulate the RH dynamics.

Stack Voltage

The ideal cell voltage relates to the change in free energy during the reaction and accounts for the difference between the operating conditions and the standard state value [53, 71, 69]. This ideal voltage is unattainable due to losses inherent to the system. The actual cell output voltage is reduced from the ideal open circuit value due to activation, ohmic, and concentration over-potential losses [72, 73]. In this model, each cell within a given CV is assumed to have the same voltage. Accounting for the voltage losses, the stack voltage output can be expressed as

$$V_{CV} = \left(V_{ideal} - V_{act} - V_{ohm} - V_{conc}\right) \times n_{cells,CV} \tag{17}$$

where V_{act}, V_{ohm}, and V_{conc} are the activation, ohmic, and concentration losses, respectively and $n_{cells,CV}$ is the number of cells in the CV. The total stack voltage is then the sum of the voltage output from each CV. The activation and ohmic overpotential losses are particularly important in this study, and will be discussed briefly below.

Activation Loss

The activation loss arises due to the energy required to drive the chemical reactions at the anode and cathode electrode surfaces. This overpotential loss is determined by the catalytic activity of the electrodes, and can be modeled using the following equation [53]:

$$V_{act} = V_0 + V_a\left(1 - e^{-c_1 \cdot i}\right) \tag{18}$$

where V_0, V_a and $c_1$depend on the oxygen partial pressure and temperature. These values can be determined from a regression of experimental data [53].

Ohmic Loss

The ohmic loss results from the resistance of the membrane to proton transfer and the electrode and collector plate to electron transfer. Ohmic losses can be expressed as

$$V_{ohm} = i \cdot R_{ohm} \tag{19}$$

where R_{ohm}, the membrane's internal electrical resistance, is the ratio of the membrane thickness t_m to its electrical conductivity σ_m,

$$R_{ohm} = \frac{t_m}{\sigma_m} \tag{20}$$

The membrane conductivity is a function of the membrane water content and is found using the empirical relations.

$$\sigma_m = b_1 exp\left(b_2\left(\frac{1}{303} - \frac{1}{T_{fc}}\right)\right) \tag{21}$$

$$b_1 = \left(b_{11}\lambda_m - b_{12}\right) \tag{22}$$

where b_2, b_{11}, and b_{12} are empirically determined constants specific to the membrane being used. Given the strong dependence of this term on the membrane humidity, the ohmic losses can vary substantially with the humidity level.

The dynamic model equations describing the heat and mass transfer, electrochemical reactions, and thermodynamics of the system, were implemented in the Matlab/Simulink environment. Experiments were conducted for model validation.

MODEL TUNING AND EXPERIMENTAL SETUP

The developed model was experimentally validated using a 2 kW PEM fuel cell stack. Dimensions of the stack are shown in Table 1. Each cell of the fuel cell stack has a five–layer membrane electrolyte assembly (MEA), which consists of the catalysts, 50 μm thick Nafion 212, and 190 μm thick hydrophobic Toray 160 carbon paper gas diffusion layers (GDLs). The flow fields were created from graphite plates with machined serpentine patterns for the anode and cathode channels in a cross-flow configuration. The test station used for the experiments was an FCATS G100 made by Greenlight Innovation. The fuel cell stack and location of the sensor used for validation of the RH model are shown in

Figure 3. The test station controls the temperature, flow rate, pressure, and humidity of the reactants and coolant. The upstream and downstream flow conditions as well as the voltage output for all the cells were monitored at a 1 Hz sampling rate. Hydrogen of 99.999% purity and compressed air were used as the reactant gases.

To measure the dynamic RH response, a Vaisala HMT337 RH sensor was installed in the cathode outlet. Installation of this sensor required additional piping and a sensor housing. To match the experimental results directly, another CV was implemented in the model to compensate for the dynamics in the sensor housing using mass and energy conservation laws. The rate of change of internal energy, U_{SH}, in the sensor housing CV can be obtained from the following energy balance equation,

$$\frac{dU_{SH}}{dt} = Q_{SH,conv} + H_{SH,in} - H_{SH,out} \tag{23}$$

where $Q_{SH,conv}$ is the rate of heat lost by convection to the surroundings, $H_{SH,in}$ is the inlet enthalpy flow rate from the fuel cell stack outlet, and $H_{SH,out}$ is the outlet enthalpy flow rate leaving the sensor housing. The effective heat transfer coefficient from the sensor housing to the surroundings was experimentally determined by measuring the temperature difference across the housing at known flow rates. Inlet and outlet energy flows were treated similarly as in the cathode channel as discussed in Chapter III.

TABLE 1: EXPERIMENTAL FUEL CELL STACK DIMENSIONS

Anode:	
Active area	5000 mm^2
Channel length	2400.3 mm
Channel width	0.864 mm
Channel depth	0.56 mm
Total exposed area	2400.3 x 0.864 = 2133.87 mm^2
Exposed to active ratio	2133.87 / 5000 x 100% = 42.7%
Total channel volume	2400.3 x 0.864 x 0.056 = 1161.36 mm^3
Cathode:	
Active area	70.75 x 70.75 = 5000 mm^2
Channel length	1768.8 mm
Channel width	1.5748 mm
Channel depth	1.27 mm
Total exposed area	1768.8 x 1.5748 = 2785.5 mm^2
Exposed to active ratio	2785.5 / 5000 x 100% = 55.7%
Total channel volume	1768.8 x 1.5748 x 1.27 = 3537.59 mm^3
Fuel cell body (graphite):	
Area	127 x 127 = 16129 mm^2
Thickness	16.6125 mm
Total surface area	127 x 16.6125 x 30 x 4 sides = 253174.5 mm^2 = 0.253 m^2
Coolant:	
Channel length	381 mm
Channel width	2.54 mm
Channel depth	1.27 mm
Total channel volume	381 x 2.54 x 1.27 = 1229 mm^3
Total exposed area	381 x 2.54 = 967.74 mm^2

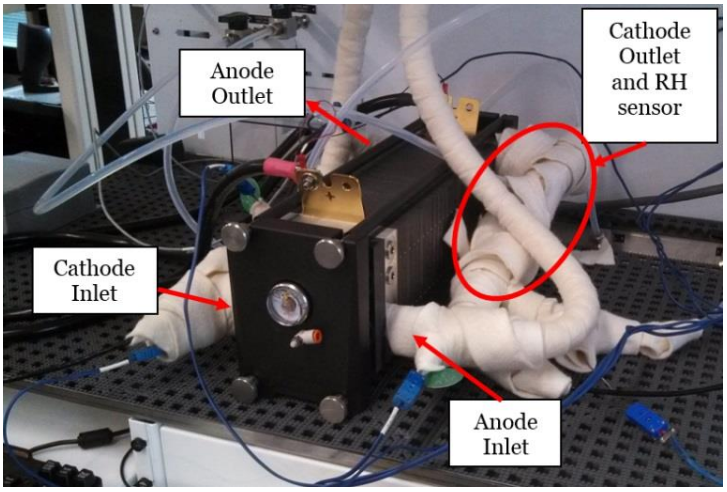

FIGURE 3: THE 2 KW PEM FUEL CELL STACK USED FOR MODEL VALIDATION.

CROSS FLOW EXPERIMENTS AND MODELING

It should be noted that the RH response is also very sensitive to the CV pressure. Therefore, accurate correlations between the mass flow rates and pressure drops across the sensor housing and fuel cell stack were needed. To this end, a series of experiments were conducted at the nominal operating temperature (~75°C) to obtain correlations for the mass flow out of the fuel cell stack and the sensor housing of the RH sensor. To isolate the contribution of various portions of the stack (e.g. stack vs. sensor housing), the test was repeated for various configurations of the system. For each configuration that was tested, the inlet flow rate was varied over the achievable range on the test station (~1-65 nLpm) and the inlet pressure, outlet pressure, temperature, RH, and dry air flow rate were all logged such that the total flow rate could be calculated. This data was then used to create correlations for the total mass flow rate as a function of the pressure drop across the system.

The first configuration tested (4) included the full fuel cell stack with both the inlet and outlet RH sensor housings in line. The test station only records the dry air mass flow rate, so the vapor flow rate needed to be calculated to obtain correlations for the total flow rate through the system. The vapor flow rate was calculated from the reported values of the inlet temperature, pressure, dry air flow rate, and RH by calculating the humidity ratio of the flow. This was done using the following equations:

$$P_{vap} = \frac{RH\%}{100} P_{sat}\left(T_{in}\right) \tag{24}$$

$$\omega = \frac{P_{vap}}{P_{in} - P_{vap}} \frac{M_{vap}}{M_{air}} \tag{25}$$

$$\dot{m}_{vap} = \omega \cdot \dot{m}_{air} \tag{26}$$

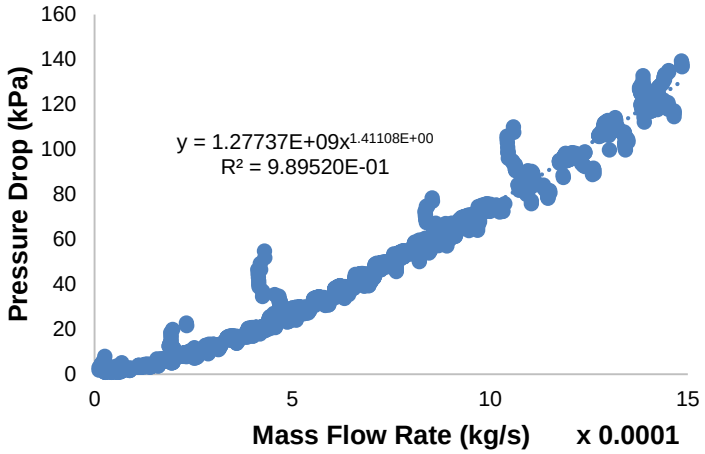

FIGURE 4: MEASURED PRESSURE VS. MASS FLOW RATE – FULL SYSTEM

For the next configuration test (5), the fuel cell stack was removed from the flow path, and the sensor housings for the inlet and outlet were directly connected. This configuration was tested over the same range of flow rates so that the contribution of the sensor housings to the total pressure drop through the system could be determined. It should be noted that some minor losses may have been incurred with the use of a short pipe to connect the two sensor housings, but were limited by minimizing the pipe length and maintaining a constant diameter through the connections to limit any expansion/contraction losses.

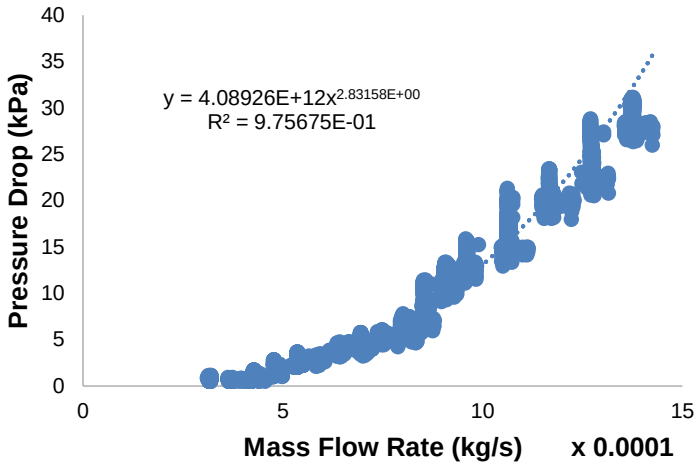

FIGURE 5: MEASURED PRESSURE VS. MASS FLOW RATE – SENSOR HOUSINGS ONLY

Given the connections required to complete the flow path in the fuel cell, it is not possible to isolate the fuel cell stack to directly measure its contribution to the pressure drop of the system. As such, the pressure drop across fuel cell stack was determined from the difference between the full system and sensor housing experiments. The pressure drop seen at a given flow rate for the total system is equivalent to the pressure drop across the sensor housings plus that of the fuel cell stack itself. The best fit equations for the pressure drop as a function of the flow rate from the two experiments were used to calculate the sensor housing contribution and isolate the fuel cell stack contribution. The difference between the total system pressure drop and sensor housing pressure drop at the associated flow rate was then taken to be the contribution of the fuel cell stack itself, and another best fit curve was generated to give the appropriate mass flow equation for the stack, as shown in Figure 6.

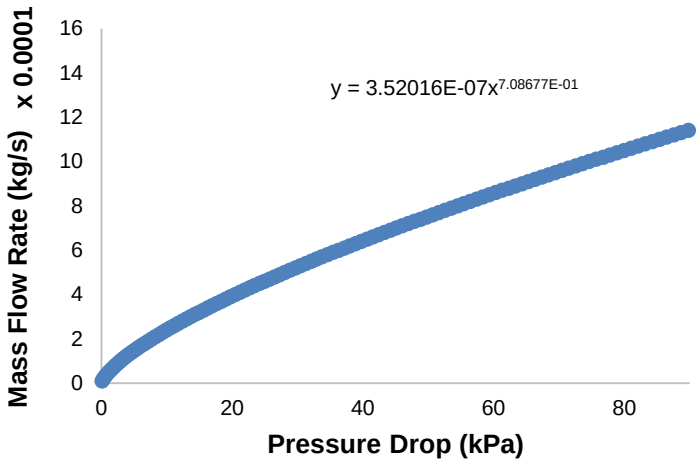

FIGURE 6: CALCULATED MASS FLOW RATE VS. PRESSURE DROP– STACK ONLY

The equation shown in Figure 6 gives a good basis for calculating the mass flow rates out of each CV as a function of the difference in pressure between successive CVs. However, this equation cannot be implemented directly because while the experimental pressure measurements are taken at both ends of the stack/sensor housing assembly, the representative stack pressure should lie somewhere between these measured pressures. In the model, the mass flow rates between CVs are determined from the pressure differences between the CVs. Subsequently, the pressure in a given CV is dependent upon the total mass and temperature within the CV. As a result, the mass flow rate equations have to be properly gauged such that the CV pressure stabilizes to the appropriate range to ensure the accuracy of the voltage and humidity responses. Assuming that the pressure declines linearly in x, estimates can be made regarding the driving pressure for the flow (e.g. the difference between the CV pressure and downstream pressure). This point is illustrated in Figure 7 and 8.

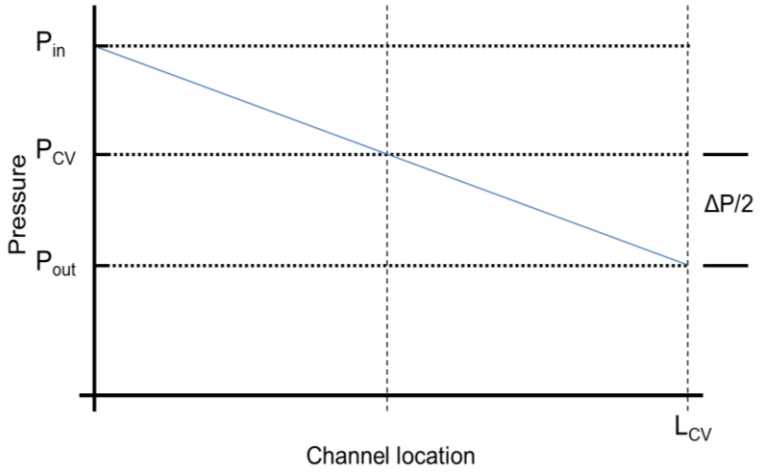

FIGURE 7: REPRESENTATIVE PRESSURE FOR A ONE CV MODEL

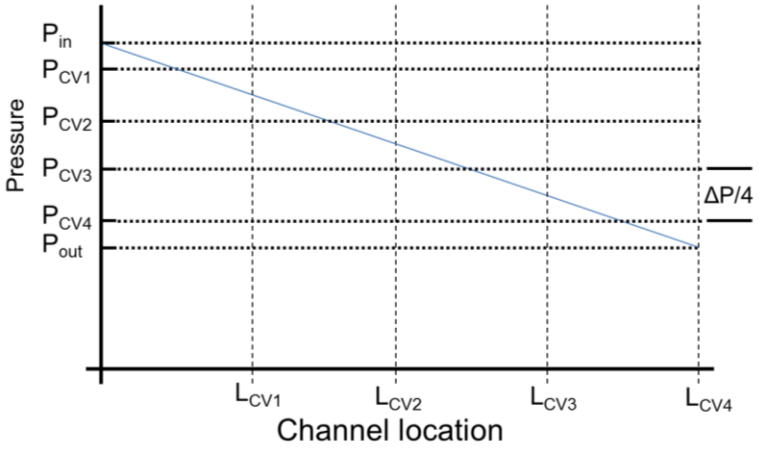

FIGURE 8: REPRESENTATIVE PRESSURE FOR A FOUR CV MODEL

For a given flow rate with a one CV model the representative pressure should be halfway between the inlet and outlet pressures of the stack, i.e. the calculated flow rate should be the same for a pressure drop that is half of the total pressure drop across the stack. In the multi-CV model, a similar argument can be made, but the same mass flow rate should be calculated for a pressure drop equal to the stack pressure drop divided by the number of CVs for flow between successive CVs (though this is slightly different for

the last CV). Figure 9 and Figure 10 show the resulting mass flow rate equations using these assumptions for a one CV and six CV model, respectively.

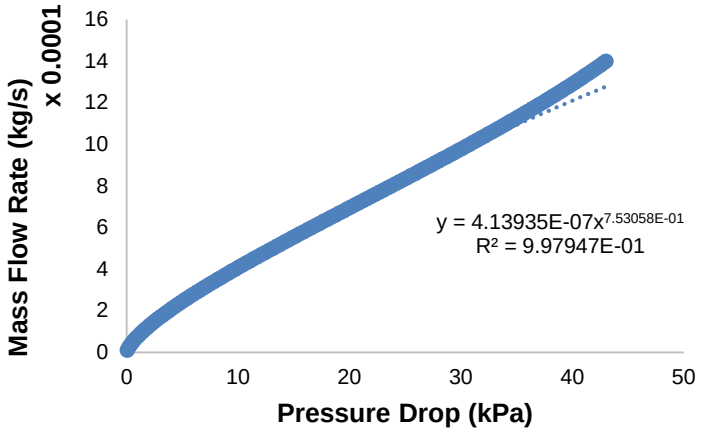

FIGURE 9: MASS FLOW RATE VS. PRESSURE FOR A ONE CV MODEL

The equations from Figure 9 and Figure 10 were used to model the flow rates out of each CV for the one CV and six CV models, respectively. Note that though these correlations are specific to our stack and test station, similar experiments could easily be run for other stack designs. It should also be noted that such experiments would most likely be required to yield reasonable estimates of the water levels in stack in question as general channel flow correlations are not likely to lead to the requisite accuracy. Experimental validation of the full model is discussed in the following section.

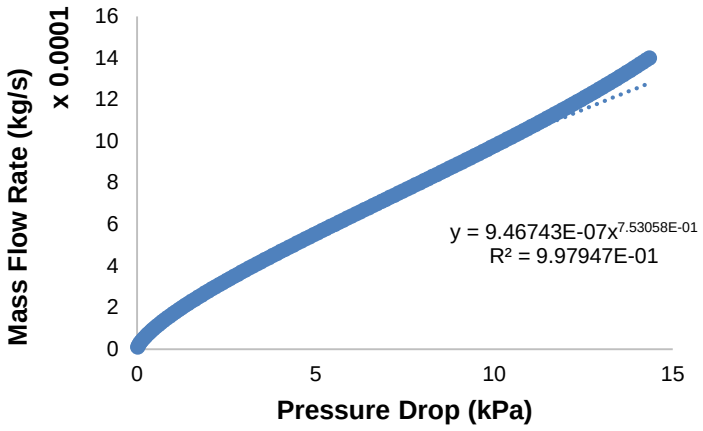

FIGURE 10: MASS FLOW RATE VS. PRESSURE FOR A SIX CV MODEL

ONE CV AND MULTI-CV MODEL COMPARISONS

An experiment was conducted to tune various parameters in the model. The current load was varied from 0 to 8.5 A, the coolant temperature was set to 75°C, and the anode and cathode inlet temperatures were set at 80°C. Figure 11 shows the modeled and experimental cathode RH response using one CV to represent the entire channel from this experiment. It shows that the modeled response is not able to capture the peaks and dynamics of the measured response. Note that the modeled RH prediction in the sensor housing is slightly higher than that in the cathode CV because the temperature in the sensor housing is lower than that in the fuel cell stack due to heat lost to the surroundings. Table 2 (at the end of this section) summarizes the error in the RH and voltage simulations for both the one CV and six CV modeling techniques at the end of this section.

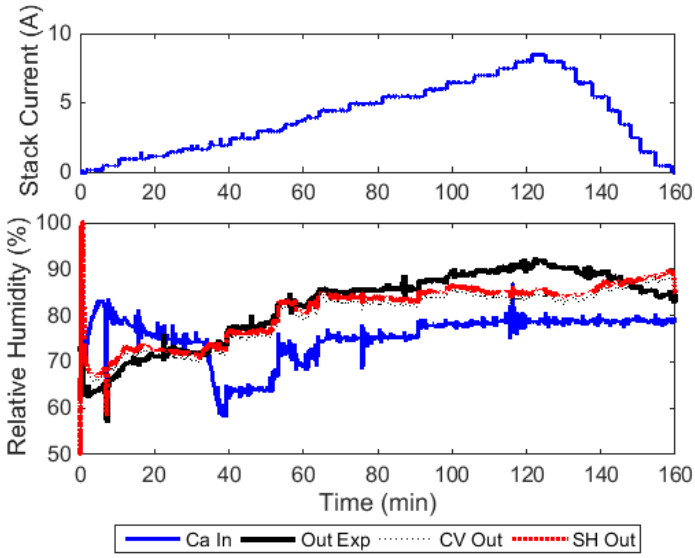

FIGURE 11: EXPERIMENTAL AND MODELED RELATIVE HUMIDITY RESPONSE WITH ONE CV MODEL - CALIBRATION TEST

Using a single lumped CV, the RMS error for the entire experiment was 2.74% RH. However, the one CV model showed the greatest disagreement with experimental data at high loads when more water vapor was generated in the stack. During the peak current section of the test (8.5 A; starting at t= 120 min), the RMS error was 5.95% RH and the maximum error was 6.52% RH. Since the entire cathode channel is represented by only one CV, the model cannot account for the accumulation of the water vapor generated by the reaction toward the stack outlet. This result shows that a one CV model cannot predict the onset of flooding towards the end of the stack, which is a major concern in real-time operation. A flooding control algorithm using this model structure would inherently lead to flooding issues in the outlet cells at high loads, resulting in significant efficiency reductions when demand is highest, unless an expensive RH sensor was in the outlet for direct feedback control.

To improve the model prediction, six CVs were used to discretize the cathode channel. Again, six, evenly sized CVs were chosen to represent the cathode channel as a result of previous work that showed that six CVs could capture the spatial variations without and excessive increase in the computational expense [67]. In the model, each successive CV feeds into the next, making it possible to predict the accumulation of water vapor at the stack outlet. This improves the agreement between the model prediction and the experimental RH data measured in the sensor housing significantly. Figure 12 shows the measured and simulated sensor housing RH using six CVs to represent the cathode channel in response to the current profile shown in Figure 11.

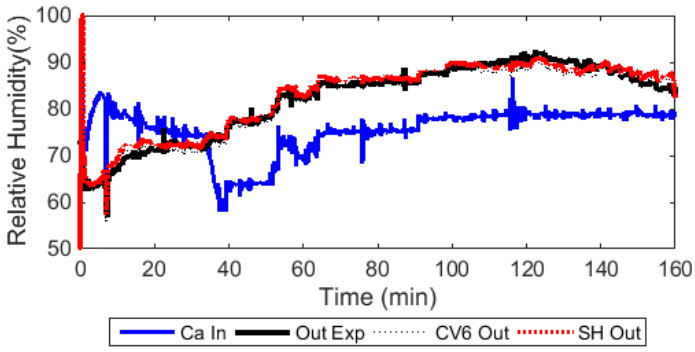

FIGURE 12: A COMPARISON OF RELATIVE HUMIDITY RESPONSES BETWEEN EXPERIMENT AND A SIX CV MODEL - CALIBRATION TEST

The discretized cathode model greatly improves the agreement between the model prediction and experimental data, and is able to capture the dynamics of the RH response with varying loads. Using this method, the average RMS error for the entire test was reduced to 1.19% RH. More importantly, during the peak current section of the test, the average RMS and maximum errors were reduced to 1.09% and 1.94% RH, respectively. This implies that the model can be used for more accurate predictions of cathode flooding conditions. In Simulink, the six CV model required ~100s to simulate the 160 minutes of

experimental data, versus ~10s with the one CV model. Despite the increase in simulation time, the computational cost is still sufficiently low for control design, and the improvement in accuracy justifies the additional computational expense. Furthermore, before use in a real-time controller, the model would be converted to C code, which will significantly increase the calculation speed.

To further emphasize the advantage of the distributed modeling technique for the RH and the shortcoming of a fully lumped model, Figure 13 compares the RH response of selected CVs from the six CV model to the fully lumped model response. The one CV model prediction lies between the predicted values of the first and last CVs in the six CV model. It can be seen that the one CV prediction is very near the average of the six CVs and inlet RH. A single CV should represent the weighted average of the profile for the entire stack. Consequently, a single CV cannot accurately model the increase in RH beyond the weighted average value that is seen towards the end of the stack. This limits the applicability of the one CV model for control design, as flooding near the stack outlet is a major concern. It will be shown later that the prediction of stack voltage is also improved somewhat, as the ohmic overpotential prediction is highly dependent on the RH. When the RH prediction is improved, so is the stack voltage prediction.

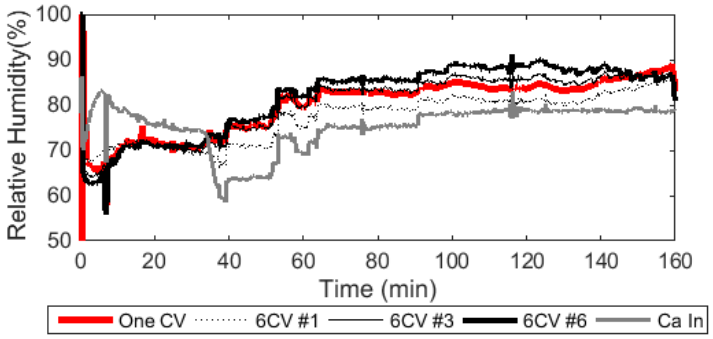

FIGURE 13: ONE AND SIX CV MODEL RH RESPONSE COMPARISON

STACK VOLTAGE MODEL CALIBRATION

Figure 14 shows the simulated and measured stack voltage using the same voltage parameters found in [53, 66], as well as the results of the tuning process to be discussed here. It can be seen that using the previously reported values, the measured voltages are significantly lower than the model predictions. Though the overall trends in the voltage response were similar, the low-load loss seen in the experimental data was much larger than the simulated losses. This was due to membrane aging effects. Note that the previous voltage calibration was done four years before the current the experiments presented in this chapter. Over time, the membrane resistance to proton flow could have increased for a number of reasons, as mentioned previously. The parameters published in reference [53] were experimentally determined based on new membranes, and do not apply to significantly aged membranes.

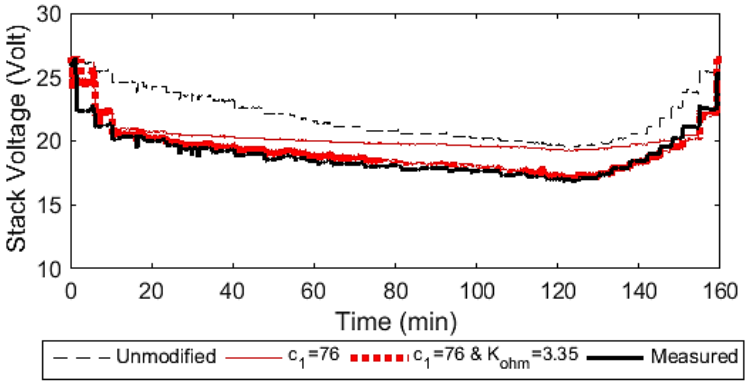

FIGURE 14: EXPERIMENTAL AND SIX CV MODEL VOLTAGE RESPONSES BEFORE TUNING

To compensate for the changes in the voltage model, the model parameters were tuned to reflect the aging of the membranes using the Simulink Design Optimization toolbox in MATLAB/Simulink. The first discrepancy seen in Figure 14 was the sharp decrease in the voltage at low currents. Parameter c_1 in Eqn. (18) was selected to correct the low current loss. By increasing the value from 10, the value associated with new membranes, to 76, the activation overpotential contribution was shifted to lower current densities without altering the magnitude, as shown in Figure 14.

This alteration corrected the low voltage loss issue. However, the experiment still showed a larger voltage decline with increasing currents than the model prediction. This suggested that the ohmic resistances through the membranes had also increased with age. A gain of 3.35 was added to the ohmic loss term in Eqn. (17) to compensate for this change. The result of this adjustment is also shown in Figure 14.

After applying both adjustments to the six CV cathode model, the predicted and experimental voltage responses were in close agreement. The improved RH model with multiple cathode CVs enhanced the accuracy of the voltage prediction by accurately

predicting the ohmic loss contributions, which are highly sensitive to the membrane RH. The discretized cathode model also compensates for the decrease in pressure along the channel in the voltage model, which further improves the model accuracy.

To compare the performances of the model with one and six control volumes for the cathode channel, the voltage response of the one CV model was obtained using the parameters for the aged membranes. The result is shown in Figure 15.

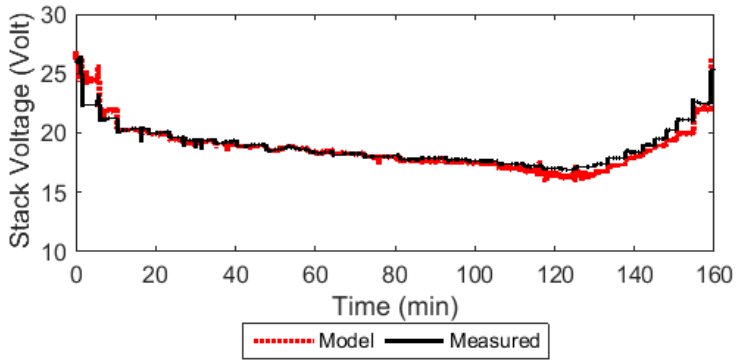

FIGURE 15: EXPERIMENTAL AND ONE CV MODEL VOLTAGE RESPONSES

All modeling parameters were kept the same between the one CV and six CV model simulations. Though the voltage response using the one CV model is reasonably accurate, it can be seen that the voltage response with the one CV model deviated from the experimental result due to the inaccuracy of the RH prediction. Since the one CV model does not predict the higher humidity levels that exist towards the end of the channel at high loads, it cannot predict the reduction in the ohmic overpotential in the latter sections of the channel. As a result, the one CV model voltage response was lower than that seen experimentally at these higher loads. This suggests the inability of a single lumped

parameter model to properly predict dehydration or flooding and the importance of local humidity conditions on the prediction of stack voltage output.

Table 2: Relative Humidity and Voltage Error Calibration Test (0-8.5A)

	#CVs	Full test	$I_{peak, RMS}$	$I_{peak, max error}$
RH	1	2.74%	5.95%	6.52%
	6	1.19%	1.09%	1.94%
Voltage	1	0.80 V	0.55 V	0.62 V
	6	0.57 V	0.26 V	0.47 V

Model Validation Test

Once the model was calibrated, it was used to model a validation test to assess the accuracy of the RH and voltage response of the tuned model under various input and load conditions. For the validation test, the current was varied from 0 to 15 A, the coolant temperature was set to 75°C, and the anode and cathode inlet temperatures were set to 80°C.

Figure 16 and 17 compare the measured and predicted responses of the RH and voltage, respectively. Figure 16 confirms the validity of the tuning of the six CV RH model. The simulated RH response tracks the validation test results closely, even with sharp increases in the current (i.e., water generation rate) and changes to the RH of the inlet flow.

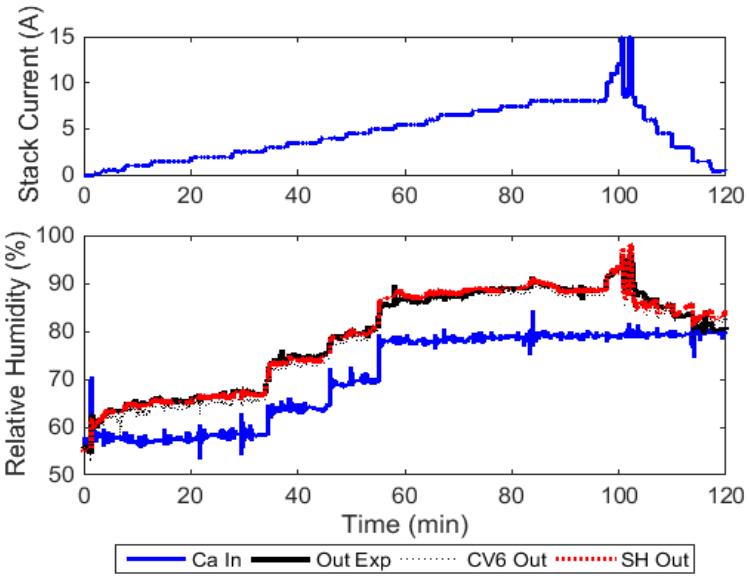

FIGURE 16: EXPERIMENTAL AND SIX CV MODEL RH RESPONSES IN A VALIDATION TEST

It can be seen in Figure 17 that the model also accurately predicts the stack voltage from the validation test. Table 3 reports the error in the RH and voltage response of both the one and six CV models for the validation test. For both the RH and voltage, the fast output fluctuations due to sudden changes in the stack load are captured with the six CV model. However, the one CV model deviated from the data the most during this section of the test.

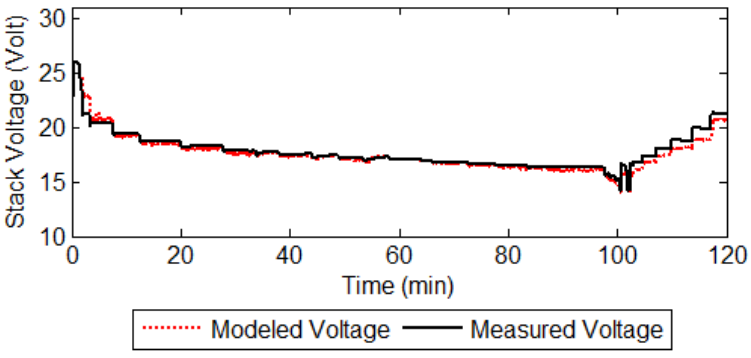

FIGURE 17: EXPERIMENTAL AND SIX CV MODELED VOLTAGE RESPONSES IN A VALIDATION TEST

Table 3: Relative Humidity and Voltage Error Validation Test (0-15A)

	#CVs	FULL TEST	$I_{PEAK, RMS}$	$I_{PEAK, MAX ERROR}$
RH	1	3.60%	8.56%	9.22%
	6	1.06%	1.45%	1.78%
VOLTAGE	1	1.29 V	1.56 V	1.73 V
	6	0.48 V	0.33 V	0.40 V

Figure 18 shows the RH and voltage for the series of sharp increases in current around the 100 min mark of the validation test. It can be seen that the magnitude and timing of the extrema in the measured responses are accurately predicted. However, when the current drops, the predicted RH decreases more quickly than the measured response. The voltage prediction is slightly lower than the measured with these current drops as well. This may be caused by the low RH prediction leading to higher prediction of the ohmic losses.

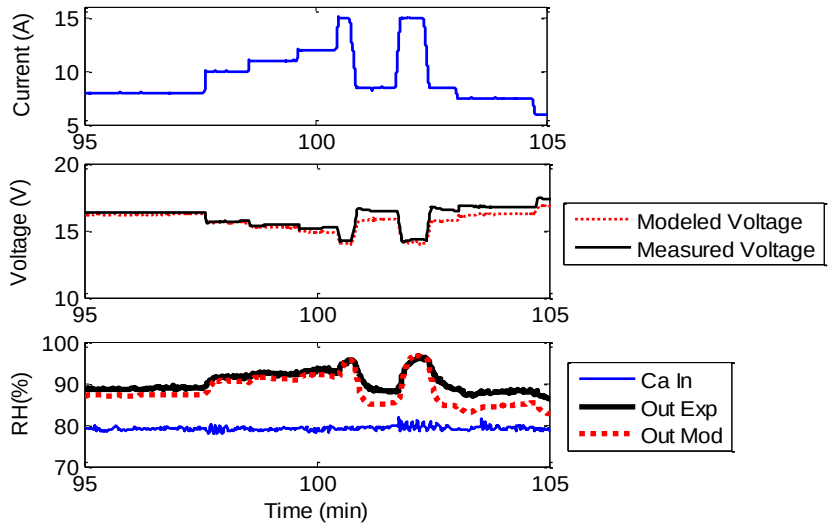

FIGURE 18: EXPERIMENTAL AND SIX CV MODELED VOLTAGE RESPONSES IN A VALIDATION TEST

Despite these errors, the model is far more capable of capturing the fast dynamics of both the voltage and RH responses in the stack than a single CV model. The accurate model prediction using six CVs shows the advantage of using multiple volumes for the cathode channel. For specific applications, a tradeoff analysis can be done to find the

optimal number of CVs to balance the modeling accuracy and computational cost for the given system. Methods to more accurately size CVs based on the system parameters will be discussed in Chapters III and IV.

DISTRIBUTED SIMULATION RESULTS

Though the RH in the individual cells cannot be measured directly, the accuracy of the model with the experimental output shows the advantage of the new, multi-CV approach. The voltage response also improved as compared to the one-CV model despite the large differences in humidification states along the channel that the model shows. This section will now look at the simulated response in the six CVs associated with the calibration and validation experiments.

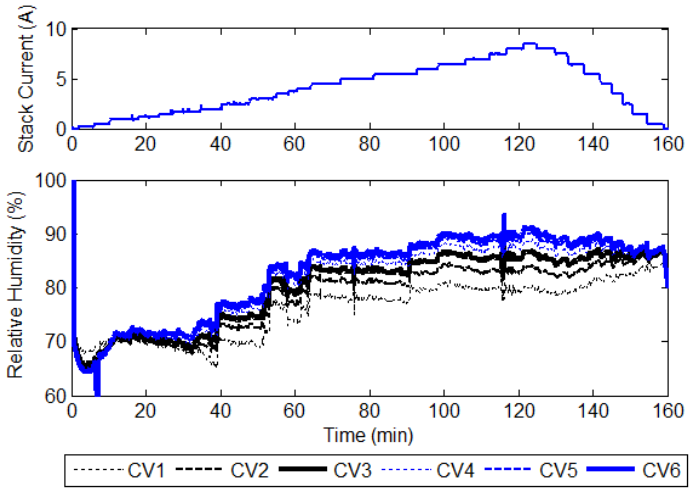

FIGURE 19: RELATIVE HUMIDITY ALONG THE CATHODE CHANNEL LENGTH (1=INLET; 6=OUTLET) CALIBRATION TEST

Figure 19 shows the relative humidity response from the individual sections of the stack in the model from the calibration test. This figure shows the broad range of humidities covered across the channel, and also how the RH increases along the length of

the channel. The new modeling method properly accounts for the accumulation of vapor towards the end of the stack, which makes it possible for the model to accurately predict the experimental outlet RH.

Figure 20 shows the voltage response from selected sections of the stack and the stack average during the calibration test. Only the response from the first and second CVs are shown because the difference between the remaining CVs is minimal.

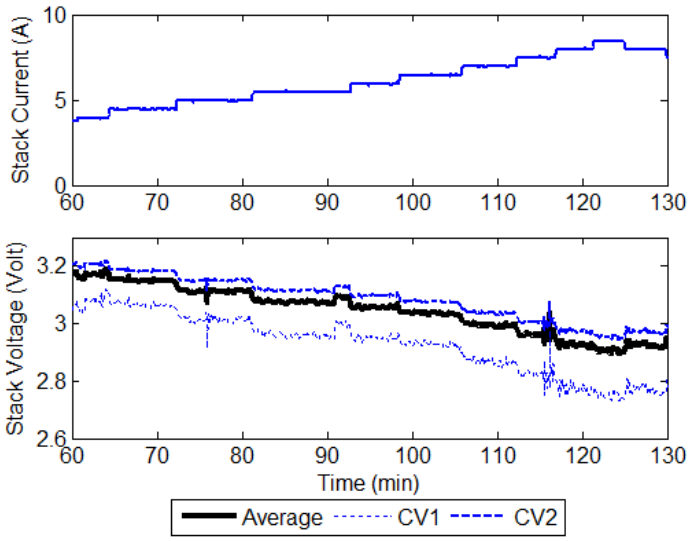

FIGURE 20: VOLTAGE RESPONSE FROM SELECTED CVS AND STACK AVERAGE CALIBRATION TEST

The voltage output of the first CV is much lower than the stack average due to the relatively low RH in this CV causing a high ohmic overpotential loss. The water generated in the first CV feeds into the second, which increases the RH in the second CV. This reduces the ohmic losses in the second CV, which improves the voltage output considerably. From the second CV to the last, the voltage output decreases slightly in each successive CV due to the decreasing pressure along the length of the stack, as shown in the following figure.

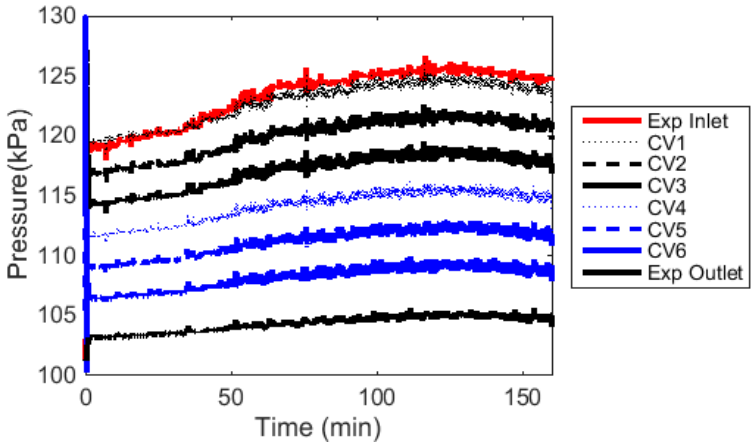

FIGURE 21: PRESSURE RESPONSE ALONG CATHODE CHANNEL CALIBRATION TEST

Note that in Figure 21 the differences in pressure between the measured points and the ends of the stack are due to the resistances from the housings used to accommodate the sensors at the inlet and outlet. The mass flow rate between each CV is modeled based on the pressure differences between CVs. This leads to the pressure decline along the length of the stack. As the pressure also dictates the species concentrations, the voltage declines slightly due to this affect as well.

The modeling results from the calibration test show the advantage of using multiple submodels for the cathode, as issues in specific areas of the stack can be isolated readily. Particularly, in this case, the model predicts a lower voltage from the inlet cells, which is often the case for PEM fuel cells in operation and can be the limiting factor in the selection of operating conditions. In the test performed for validation, around the 100min mark, the 15A load had to be removed due to low voltage warnings in the first cell. The model predicts a similar drop in voltage with high loads in the first CV. This shows the potential

for this model to be used in conjunction with an on-board controller to regulate the output of individual sections of the stack.

Figure 22, 23, and 24 show the simulated response of the RH, voltage, and pressure from each CV corresponding to the validation test, respectively. Similar trends can be seen with these plots as were noted with the plots from the calibration test.

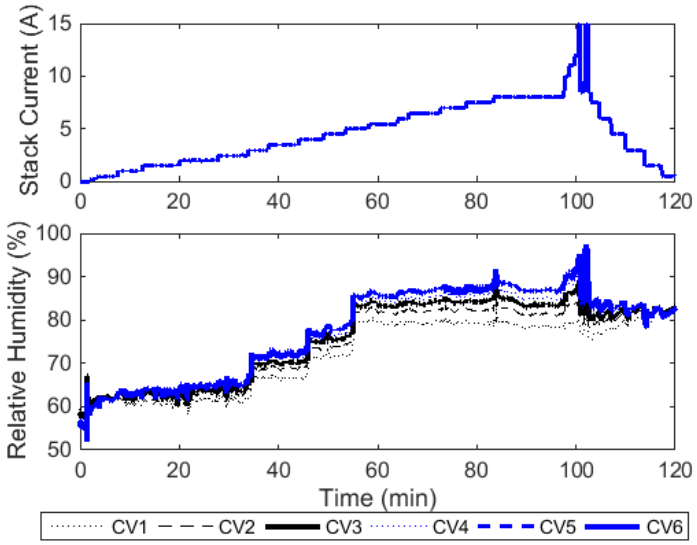

FIGURE 22: RELATIVE HUMIDITY ALONG CHANNEL LENGTH (1=INLET; 6=OUTLET) VALIDATION TEST

Figure 22 shows a large increase in the relative humidity from the inlet CV to the outlet CV, in excess of 10% at the higher loads. However, the RH differences between successive CVs decrease toward the outlet. This is due to the influence of the concentration driven back diffusion, which works to stabilize the RH between the anode and cathode. As the cathode RH increases, further increases become more difficult as more water vapor is driven to the anode. As such, towards the end of the stack, the RH tends to stabilize for a given load. This suggests that an uneven spacing of the CVs in the cathode may be useful to improve the granularity between each CV. This will be discussed further in Chapter IV.

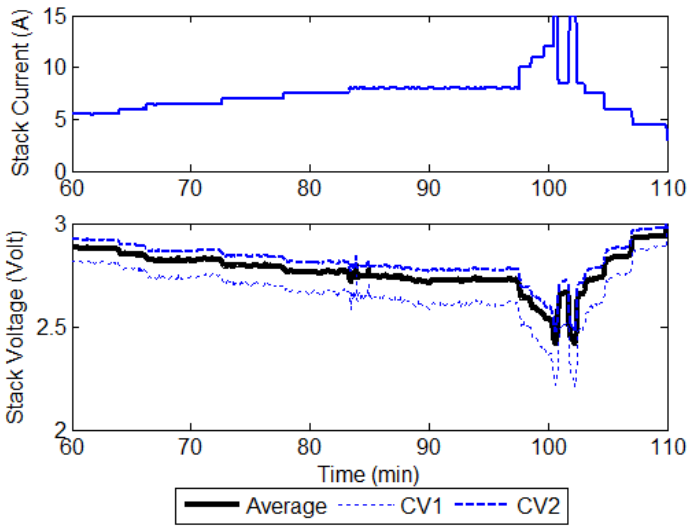

FIGURE 23: VOLTAGE RESPONSE FROM SELECTED CVS AND STACK AVERAGE VALIDATION TEST

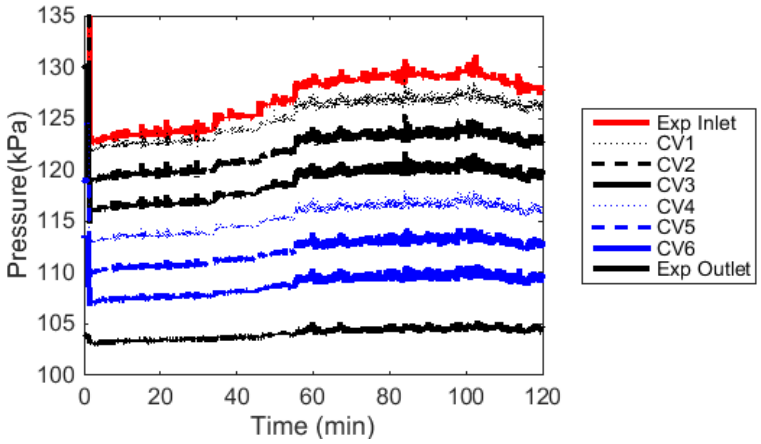

FIGURE 24: PRESSURE RESPONSE ALONG CATHODE CHANNEL VALIDATION TEST

SUMMARY

The subdivided cathode model accounts for the accumulation of vapor towards the end of the stack, which is necessary to properly predict membrane flooding conditions. Modeling results using six CVs to represent the cathode channel provided good agreement with the experimental data of the RH response with varying current demands and inlet RH

levels. This was not possible using a single CV to represent the cathode channel due to the significant spatial variations inherent to PEM fuel cell systems. Modeling the cathode channel with six CVs also begins to capture the relatively poor voltage response seen in the inlet cells of the stack. This information could be key to properly manage membrane health across the entire fuel cell assembly. Meanwhile, the computation time remained acceptable for real-time control applications.

Chapter III: PEM Fuel Cell Thermal Model Scaling and Modeling Implications[2]

MOTIVATION

Local relative humidity levels contribute heavily to cell performance. In low flow regimes of fuel cell operation, channel flooding can be severe, and cause a significant drop in voltage and efficiency [74]. And as previously stated, low humidity levels lead to significant ohmic losses within the membrane, which reduces efficiency and causes damage to the membrane [75, 58].

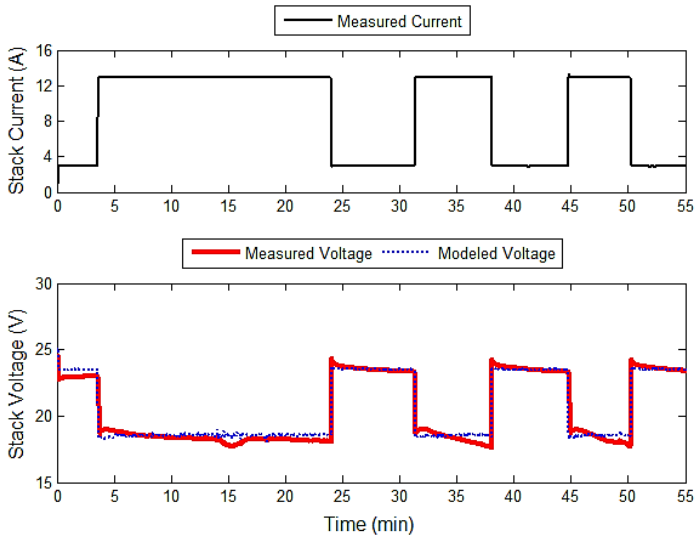

FIGURE 25: MODELED AND EXPERIMENTAL VOLTAGE STEP LOAD TEST

[2] Some of the work of this chapter has been published in the International Journal of Hydrogen Energy: Headley, Alexander J., and Dongmei Chen. "Critical control volume sizing for improved transient thermal modeling of PEM fuel cells." *International Journal of Hydrogen Energy* 40.24 (2015): 7762-7768.

In addition to the need for better RH control, this research aims to pinpoint the source of some of the cell-to-cell performance variations seen in past experiments. Figure 25 shows the experimental stack voltage response from an early test. This figure shows that the lumped model leads to a good overall correlation. However, closer inspection of the data revealed some lost dynamics in the voltage model. When the stack was subjected to high loads, particularly for the second and third load steps in the test, there was a steady decline in voltage that the model does not predict. Further investigation of the experimental results showed that a localized phenomenon led to the decline in the average voltage. Figure 26 shows the voltage response of a few of the key cells from the step profile test.

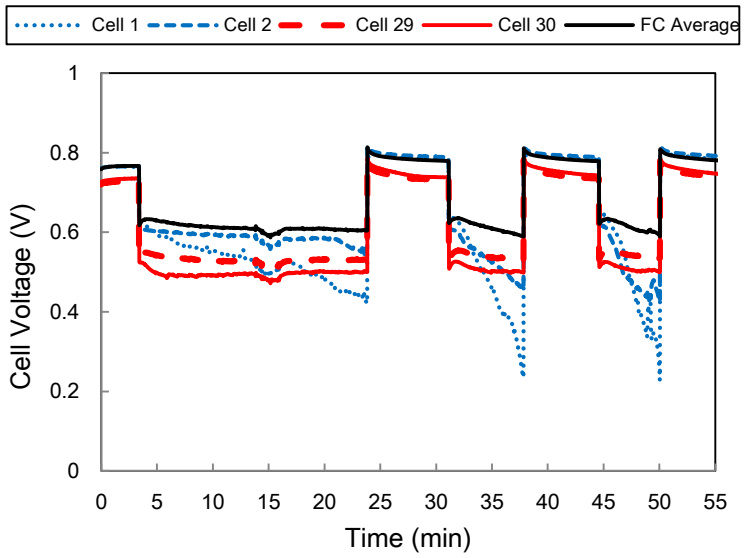

FIGURE 26: INDIVIDUAL CELL PERFORMANCE DURING THE VALIDATION TEST

As the figure shows, the large decline in performance in the first and second cells of the stack led to the trend seen in the stack average that the model was unable to predict. High ohmic resistances at the inlet cells were very likely the main contributor to the localized phenomena (here Cell 1 is the inlet and Cell 30 is the outlet). It should also be

noted that though the slight drop in the total stack voltage may seem insignificant, during this test, it was necessary to remove the load to avoid any permanent damage to the inlet cells.

In operation of larger stacks, controllers often need to adjust to accommodate the response of only a few cells. Typically, the end cells are of the utmost concern. This fact, typified by our experimental results and the modeling results presented in Chapter II, show that the lumped value approach is insufficient for larger fuel cell stacks as there are localized effects that need to be considered to determine the operating conditions for the stack. However, as discussed previously, individual modeling of each cell would be computationally expensive, and thereby poorly suited for dynamic control design and implementation. Therefore, the questions becomes how to optimize the accuracy of the reduced order models that are required for control design while limiting the additional computational expense.

Proper thermal modeling is a vital prerequisite to accurate relative humidity modeling. As such, the goal of this investigation was to develop a method by which to properly size control volumes in the cathode channel for thermal accuracy along the flow channel, which would thereby enable an appropriate study of the relative humidity profile in the stack. This needed be done while minimizing the number of CVs, thereby limiting the computation expense of the model as well. To this end, decision criteria were also needed to determine the minimum number of CVs needed to obtain the desired accuracy. The proposed model schematic is shown in Figure 27.

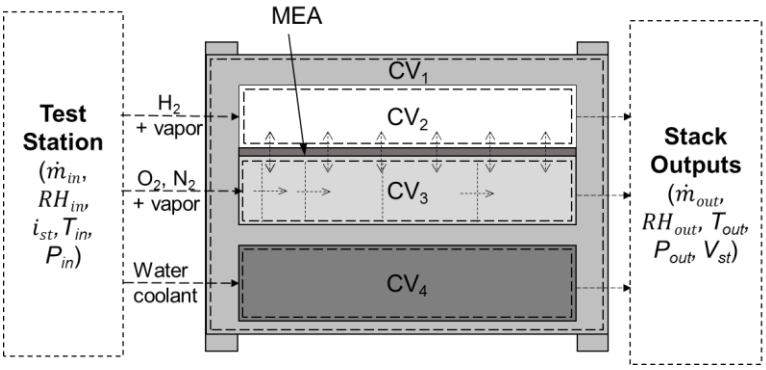

FIGURE 27: PROPOSED THERMAL MODELING SCHEMATIC

This model structure would improve accuracy along the length of the channel as the majority of the CVs would be limited to the areas of the channel with the largest temperature gradients.

ENERGY EQUATION AND SCALING ARGUMENTS

To begin the analysis, the cathode channel energy balance was expressed in a one-dimensional form:

$$\rho c_p \frac{\partial T}{\partial t} + \frac{\dot{m} c_p}{A}\frac{\partial T}{\partial x} - k\frac{\partial^2 T}{\partial x^2} + \frac{hP}{A}\left(T - T_{fc}\right) - \frac{\left[\left(\dot{m}''_{H_2O,gen} + \dot{m}''_{H_2O,MEA}\right)c_{p,H_2O}T_{fc} - \dot{m}''_{O_2,reac}c_{p,O_2}T\right]}{d} = 0 \qquad (27)$$

The terms in Eqn. (27) are 1) energy storage in the differential element, 2) advection through the element, 3) conduction through the element, 4) convection to the fuel cell body, and 5) reacted and generated mass enthalpy flows in the CV, respectively. In Eqn. (27), T refers to the temperature in the CV and T_{fc} is the temperature of the fuel cell graphite body. The mass flow rate associated with the advection term is taken to be the inlet flow rate for analysis, and the convective heat transfer coefficient is assumed to be constant for the

length of the channel. To determine the relative importance of the terms in Eqn.(27), the length, temperature, and time scales were non-dimensionalized as

$$x_d = \frac{x}{L_c} \quad \theta = \frac{T - T_{fc}}{T_{ca,in} - T_{fc}} = \frac{T - T_{fc}}{\Delta T} \quad t_d = \frac{t}{t_c}. \tag{28}$$

Where L_c is the total channel length, $T_{ca,in}$ is the cathode inlet temperature, and T_{fc} is the fuel cell body temperature. The appropriate time scale was unknown at this point, and was given a generic variable to be determined later in the analysis. The non-dimensional temperature was defined based on the boundary conditions of the system. The inlet temperature is a given condition, which fixes one end of the temperature profile in the channel. Heat generated from the reaction is considered to be stored in the fuel cell body. This places a natural limit on the outlet temperature as all other heat inputs to the cathode channel are associated with the fuel cell body temperature.

With the non-dimensional variables applied, Eqn. (27) can be transformed into the following non-dimensional governing equation:

$$\frac{\partial\theta}{\partial t_d} + \frac{t_c}{L_c}\frac{\dot{m}}{\rho A}\frac{\partial\theta}{\partial x_d} - \frac{t_c}{L_c^2}\frac{k}{\rho c_p}\frac{\partial^2\theta}{\partial {x_d}^2} + \frac{hPt_c}{\rho cA}\theta - \frac{\left[\left(\dot{m}''_{H_2O,gen} + \dot{m}''_{H_2O,MEA}\right)c_{p,H_2O}\left(\frac{T}{\Delta T} - \theta\right) - \dot{m}''_{O_2,reac}c_{p,O_2}\left(\theta - \frac{T_{fc}}{\Delta T}\right)\right]t_c}{d\rho c_p} = 0 \tag{29}$$

For this analysis, the advective term was chosen to define the critical time scale:

$$t_c = \frac{\rho A L_c}{\dot{m}} \tag{30}$$

With this definition of the critical time scale, the importance of the time dependent storage term to the energy equation can be assessed. To accomplish this, the non-dimensional storage derivative was expanded as:

$$\frac{\partial \theta}{\partial t_d} = t_c \frac{\partial \theta}{\partial t} = t_c \left[\frac{T - T_{ca,in}}{\Delta T^2} \frac{\partial T_{FC}}{\partial t} - \frac{T - T_{FC}}{\Delta T^2} \frac{\partial T_{ca,in}}{\partial t} \right] \quad (31)$$

Equation (31) shows that this term is inversely proportional to the difference in temperature between the inlet and outlet. Therefore, the relative importance of this term increases when there is a small difference in the inlet and fuel cell body temperatures. However, in this case, the spatial gradients will be minimal as well, and it is therefore not of concern for the analysis. In cases with an appreciable difference between the temperatures, the significance of this term diminishes, and large changes in either the inlet or body temperature would need to occur in a very short amount of time for this term to be significant.

For example, if the inlet temperature is around 25°C and the fuel cell body is at an operating temperature of 85°C, for our system, the rate of temperature changes would have to be around 15K/s for the time-dependent term to be significant (O(1)). This would be nigh impossible for the fuel cell body given its thermal mass, and would only be a fleeting phenomena at the inlet if this occurred at all. As such, for this analysis, the system can be treated as a steady-state system, and the temporal component can be neglected.

Applying this simplification leads to the following non-dimensional form of the governing equation:

$$\frac{\partial \theta}{\partial x_d} - \frac{kA}{\dot{m} c_p L_c} \frac{\partial^2 \theta}{\partial x_d^{\,2}} + \frac{hPL_c}{\dot{m} c_p} \theta - \frac{\left[\left(\dot{m}''_{H_2O,gen} + \dot{m}''_{H_2O,MEA} \right) c_{p,H_2O} T_{fc} - \dot{m}''_{O_2,reac} c_{p,O_2} T_{ca,in} \right] w L_c}{\dot{m} c_p \Delta T} = 0 \quad (32)$$

The relative importance of each heat transfer mode to the temperature profile can be determined from the scale of the coefficients associated with each term. By performing

these calculations, it can readily be seen that the coefficient associated with the conductive term, is very small ($O(10^{-5})$), making conductive considerations insignificant. On the other hand, the coefficient with the convective term is much larger even for lower flow rates ($O(10^{5})$), making it the dominant term in the equation.

The final term in Eqn. (32) is far more case sensitive, as the water generation, membrane transfer, and oxygen consumption rates all depend on the current. This term can essentially be seen as a scaling of the flow enthalpy of the masses generated at or transferred through the membrane to the heat transported by the channel flow. The cross-flow consists of nitrogen, oxygen and water vapor, which all have comparable specific heats. At most, the total reacted oxygen rate can only account for approximately 21% of the total inlet mass flow rate because air is used as the cathode gas for our system. This rate of oxygen consumption leads to a similar rate of water vapor generation, which again, can at most be only a fraction of the inlet flow rate. This makes the scaling of the heat capacity flow rates on the order of 10^{-1} for large loads, assuming a temperature difference of 20K between the inlet and fuel cell body. In general, this term can only be relatively significant with very small differences in temperature between the inlet and fuel cell body. However, in this scenario, the need for multiple thermal control volumes is very low, as the fuel cell body temperature can easily be assumed for the entire length of the channel. As such, the analysis simplifies to only consider the advective and convective terms as significant to the profile.

$$\frac{\partial \theta}{\partial x_d} + \frac{hPL_c}{\dot{m}c_p}\theta = 0 \tag{33}$$

This leads to a concise expression of the temperature profile in the channel.

$$\begin{aligned} T(x) &= \Delta T \, exp\left[\frac{-hP}{\dot{m}c_p} x\right] + T_{fc} \\ &= \Delta T \, exp\left[\frac{-x}{\tau}\right] + T_{fc} \end{aligned} \tag{34}$$

where

$$\tau = \frac{\dot{m}c_p}{hP} \tag{35}$$

To calculate the proper CV sizes, an acceptable limit on the deviation between the actual temperature and the temperature calculated by the CV approach needs to be specified. In other words, we want to size the CV such that the difference between the weighted average temperature in the CV and the actual temperatures at the ends of the CV is no larger than some critical amount.

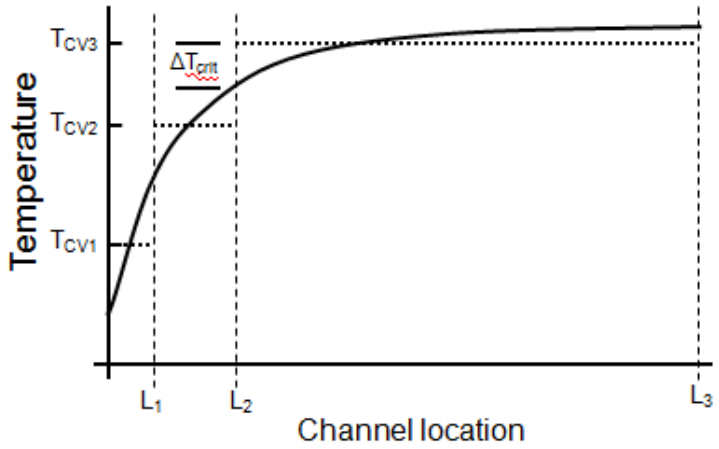

FIGURE 28: CONCEPTUAL DETERMINATION OF CONTROL VOLUME SIZES

Starting from Eqn. (34), the weighted average temperature can be calculated as

$$T_w(L_n) = \frac{\int_{L_{n-1}}^{L_n} T(x)dx}{L_n - L_{n-1}} = T_{FC} - \frac{\tau \cdot \Delta T\left(e^{(-L_n/\tau)} - e^{(-L_{n-1}/\tau)}\right)}{L_n - L_{n-1}} \tag{36}$$

Given the shape of the profile, the temperature at the start of the CV will always be further from the weighted average temperature than the temperature at the end of the CV. As such, the criteria for the selection of the CV boundaries is

$$\left|T(L_{n-1}) - T_w\left(L_{n-1} \to L_n\right)\right| = \Delta T_{crit} \Rightarrow \left|\Delta T e^{(-L_{n-1}/\tau)} + \frac{\tau \cdot \Delta T\left(e^{(-L_n/\tau)} - e^{(-L_{n-1}/\tau)}\right)}{L_n - L_{n-1}}\right| = \Delta T_{crit} \quad (37)$$

Equation (37) can then be solved numerically using parameters for the fuel cell in question to find the locations for the beginning and end of each CV. Starting from $L_{n-1}=0$, the calculation could be performed sequentially to find the length of each CV until the full channel length was reached.

AGREEMENT WITH THE SIMULINK MODEL AND POTENTIAL CV SIZING RESULTS

The following table shows the modeled temperature at selected points, and the corresponding weighted average temperature calculated using Eqn. (36). To obtain the CV temperatures with the simplified equation, parameters from the Simulink model (flow rate, temperatures, convection coefficient, etc.) were used.

Table 4: Control Volume Temperature Predictions using the Simulink Model and Simplified Equation Approximation

	SIMULINK MODEL		SIMPLIFIED EQUATION		
T_{IN}	CV1	CV2	CV1	CV2	T_{FC}
293K	337.153	341.848	337.624	342.406	342.407
323K	342.635	344.767	342.909	345.034	345.034
353K	348.272	347.72	348.17	347.635	347.635

It can be seen that the temperatures predicted by the Simulink model and Eqn. (36) are in very close agreement, with the largest difference in the temperature predicted by the

2 different methods being only 0.56K. The close agreement over the large temperature changes shows the efficacy of the scaling analysis in simplifying the governing equation, and gives us confidence in using the simplified equation as a basis for adjustments to the overall model.

Given the favorable results of the CV temperatures calculated from Eqn.(36), this equation can now be used to predict appropriate CV sizes using Eqn.(37). The following tables show examples of the resulting CV lengths for various flow and temperature conditions. Keep in mind that the flow rate and choice of the critical temperature difference greatly affect these results. For the analyses in this section, the critical temperature difference was taken to be 1K. Table 5 shows the results for a fairly typical flow case. For the fuel cell being considered, the length of the serpentine channel in a single cell is ~1.7m (51m for all 30 cells).

Table 5: Critical Lengths, Low Flow, ΔT=35K

$\dot{m}\left(\frac{kg}{s}\right)$	H (W/M^2K)	T_{IN} (K)	T_{FC} (K)
5.00E-05	78.8	323.15	358.15

CV #	L_N	L_{N-1}
1	0.014	0.000
2	0.029	0.014
3	0.047	0.029
4	0.068	0.047
5	0.094	0.068
6	0.126	0.094
7	**0.171**	**0.126**
8	0.241	0.171
9	**0.404**	**0.241**
10	**51**	**0.404**

Table 5 shows that nearly all of the temperature evolution occurs in the first quarter of the first cell in the stack. This sort of extreme temperature change in such a small space could contribute to the sort of response seen in Figure 26 as the relative humidity would plummet in a very short distance before any of the natural humidification from the stack could occur. To accurately capture the temperature profile in the channel, 10 CVs would be required as shown in Table 5. However, in practice, the number of CVs could also be limited by setting a minimum length criterion. This would cause a loss of true accuracy, but if that length was sufficiently small, the overall model response (voltage, RH, etc.) would not be significantly affected. For instance, with the minimum length set to 10% of the channel length in this scenario, three CVs could effectively capture the thermal profile.

The prior scenario shows the results for a fairly large difference between the inlet and fuel cell body temperatures (35K). Table 6 shows a similar analysis with only a 10K difference between the inlet and fuel cell body temperature. In this case, given the smaller difference between the inlet and body temperatures, reasonable accuracy can be obtained with fewer CVs. Again, we see that the multiple CV approach is limited to the first cell.

Table 6: Critical Lengths, Low Flow, ΔT=10K

$\dot{m}\left(\frac{kg}{s}\right)$	H (W/M^2K)	T_{IN} (K)	T_{FC} (K)
5.00E-05	78.8	348.15	358.15

CV #	L_N	L_{N-1}
1	0.054	0.000
2	0.148	0.054
3	0.553	0.148
4	51	0.553

Table 7 shows results with a higher flow rate. Because increasing the flow rate significantly increases the convective coefficient, the temperature stabilizes to the fuel cell body temperature in a shorter distance. Depending on the limit placed on the minimum CV length, this suggests that at higher flow rates the need for multiple thermal CVs diminishes, even with large changes in temperature.

Table 7: Critical Lengths, High Flow, ΔT=35K

$\dot{m}\left(\frac{kg}{s}\right)$	H (W/M2K)	TIN (K)	TFC (K)
3.00E-04	640	323.15	358.15

CV #	L_N	L_{N-1}
1	0.010	0.000
2	0.021	0.010
3	0.034	0.021
4	0.049	0.034
5	0.067	0.049
6	0.090	0.067
7	0.122	0.090
8	0.173	0.122
9	0.289	0.173
10	51	0.289

THERMAL SCALING STUDY IMPLICATIONS

This study was intended to improve the thermal modeling accuracy of control-oriented, lumped parameter PEM fuel cell models. The results of the analysis suggest that, depending on the situation and desired accuracy, subdivision of the first cell can be advantageous for simulating some localized issues. Particularly with low flow rates or large differences between the inlet and fuel cell body temperatures multiple thermal CVs would improve modeling accuracy. This could also be advantageous for stack designs utilizing larger cross-sectional areas, which would ultimately lead to lower cross-flow

velocities and convective coefficients. However, this analysis also showed that in many scenarios for our system, the majority of the temperature change occurs in the first quarter of the first cell. Depending on the accuracy desired, the thermal response in this section can be significant, but this effect becomes less of a concern with larger stacks and a fully lumped approximation becomes a more accurate representation of the system temperature.

The result of this study gave a good basis for a similar analysis of the relative humidity profile in the fuel cell stack. Also, this suggested that the temperature response portion of the multi-CV model could be lumped to reduce the computational expense. The latter implication will be discussed in the following section

Reducing the Order of the Distributed Model

Given the results of the thermal scaling analysis shown in the previous section, it was clear that in many cases the temperature response of the entire cathode channel could be modeled using a fully lumped CV. Furthermore, since the cathode gases quickly approach the fuel cell body temperature, the model can be further reduced by lumping the gas channels and fuel cell body into a single CV for the temperature response in the system. Note that convective heat transfer from the fuel cell body is also the dominant energy flow in the anode. This implies that the entire fuel cell stack temperature could be characterized with a single lumped CV comprised of the anode, cathode, and fuel cell body. This simplification removes seven temperature states from the six CV model, thereby reducing the computational expense significantly. The details of this simplification are discussed in the following sections.

Original Multi-CV Thermal Modeling Methodology

In the original model, the temperature is modeled by calculating heat flows between four major CVs, the anode, cathode, fuel cell body and coolant channel. The cathode channel was discretized into six CVs for both the energy and mass conservation equations. Energy conservation is applied to each CV in the following form:

$$\frac{dU}{dt} = Q_{net} + W_{net} + \sum \dot{m}_{in} h_{in} - \sum \dot{m}_{out} h_{out} \tag{38}$$

The original equation set related to temperature calculation in fuel cell model is as follows [16]:

Fuel Cell Body Control Volume

$$m_{FC} C_{FC} \frac{dT_{FC}}{dt} = Q_{gen} - Q_{an,\,conv} - Q_{ca,\,conv} - Q_{cl,\,conv} - Q_{amb,\,conv} - Q_{amb,rad} \tag{39}$$

Anode Control Volume

$$\frac{dU_{an}}{dt} = Q_{an,\,conv} + H_{an,in} - H_{an,out} \tag{40}$$

$$\frac{dU_{an}}{dt} = \left(\sum \frac{dm_{an}}{dt} C_{van} \right) T_{an} + \left(\sum m_{an} C_{van} \right) \frac{dT_{an}}{dt} \tag{41}$$

$$H_{an,in} = \left(\dot{m}_{H_2,in} C_{vH_2} + \dot{m}_{vap,in} C_{vvap} \right) T_{an,in} + \left(\dot{m}_{vap,in,MEA} C_{vvap} + m_{liq,in,MEA} C_{liq} \right) T_{an} \tag{42}$$

$$\begin{aligned} H_{an,out} = & \left(\dot{m}_{H_2,out} C_{vH_2} + \dot{m}_{vap,out} C_{vvap} \right) T_{an,out} \\ & + \left(\dot{m}_{H_2,reac} C_{vH_2} + \dot{m}_{vap,out,MEA} C_{vvap} + \dot{m}_{liq,out,MEA} C_{liq} \right) T_{an} \end{aligned} \tag{43}$$

Cathode Control Volume

$$\frac{dU_{Ca}}{dt} = Q_{ca,conv} + H_{ca,in} - H_{ca,out} \tag{44}$$

$$\frac{dU_{ca}}{dt} = \left(\sum \frac{dm_{ca}}{dt} C_{vca} \right) T_{ca} + \left(\sum m_{ca} C_{vca} \right) \frac{dT_{ca}}{dt} \tag{45}$$

$$H_{ca,in} = \left(\dot{m}_{O_2,in} C_{vO_2} + \dot{m}_{N_2,in} C_{vN_2} + \dot{m}_{vap,in} C_{vvap}\right) T_{ca,in} + \left(\dot{m}_{vap,in,MEA} C_{vvap} + \dot{m}_{vap,gen} C_{vvap} + \dot{m}_{liq,in,MEA} C_{liq}\right) T_{ca} \quad (46)$$

$$H_{ca,out} = \left(\dot{m}_{O_2,out} C_{vO_2} + \dot{m}_{N_2,out} C_{vN_2} + \dot{m}_{vap,out} C_{vvap} + \dot{m}_{liq,out} C_{liq}\right) T_{ca,out} + \left(\dot{m}_{O_2,reac} C_{vO_2} + \dot{m}_{liq,out,MEA} C_{liq}\right) T_{Ca} \quad (47)$$

Because of the six CVs used to represent the cathode channel, there are eight temperature states in total; six for the cathode, and one each for the anode and fuel cell body. All the equations are solved dynamically to find the temperature in each CV.

Modified Modeling Methodology

Using the information from the scaling analysis, the modified model uses one temperature state to represent the anode, cathode and fuel cell body. By lumping all of these control volumes into a single thermal CV, intermediate heat transfer calculations from the energy equation (i.e. convection between the body and channels and energy transfers through the membrane) can be removed, which eliminates 7 states and simplifies the calculations significantly. After applying these simplifications the contributions to the overall energy equation from each section of the fuel cell are as follows:

Fuel Cell Body

$$m_{FC} C_{FC} \frac{dT_{FC}}{dt} = Q_{gen} - Q_{cl,\,conv} - Q_{amb,\,conv} - Q_{amb,rad} \quad (48)$$

Anode Control Volume

$$\left(\Sigma \frac{dm_{an}}{dt} C_{van}\right) T_{FC} + \left(\Sigma m_{an} C_{van}\right) \frac{dT_{FC}}{dt} = H_{an,in} - H_{an,out} \quad (49)$$

Cathode Control Volume

$$\left(\sum \frac{dm_{ca}}{dt} C_{vca}\right) T_{FC} + \left(\sum m_{ca} C_{vca}\right) \frac{dT_{FC}}{dt} = H_{ca,in} - H_{ca,out} \tag{50}$$

As all of these sections share one temperature, Eqns. (48)-(50) can be combined into a single temperature calculation as follows:

$$\begin{aligned} &m_{FC} C_{FC} \frac{dT_{FC}}{dt} + \left(\sum \frac{dm_{an}}{dt} C_{van}\right) T_{FC} + \left(\sum m_{an} C_{van}\right) \frac{dT_{FC}}{dt} + \left(\sum \frac{dm_{ca}}{dt} C_{vca}\right) T_{FC} \\ &+ \left(\sum m_{ca} C_{vca}\right) \frac{dT_{FC}}{dt} = Q_{gen} - Q_{cl,\,conv} - Q_{amb,\,conv} - Q_{amb,rad} + H_{an,in} - H_{an,out} + H_{ca,in} - H_{ca,out} \end{aligned} \tag{51}$$

Re-organizing Eqn. (51) to isolate the rate of change in temperature yields:

$$\begin{aligned} \left(m_{FC} C_{FC} + \sum m_{an} C_{van} + \sum m_{ca} C_{vca}\right) \frac{dT_{FC}}{dt} &= Q_{gen} - Q_{cl,\,conv} - Q_{amb,\,conv} - Q_{amb,rad} + H_{an,in} - H_{an,out} \\ &+ H_{ca,in} - H_{ca,out} - \left(\sum \frac{dm_{an}}{dt} C_{van} + \sum \frac{dm_{ca}}{dt} C_{vca}\right) T_{FC} \end{aligned} \tag{52}$$

The RHS terms are (1) heat produced from the chemical reaction, (2) heat transferred by convection between the fuel cell body and coolant channel, (3) heat transferred from the body surface to the surroundings by natural convection, (4) heat transferred from the body surface to the surroundings by radiation, (5) enthalpy flows from the anode and cathode, and (6) partial derivatives of the internal energy with respect to mass in the anode and cathode.

On the LHS, the coefficient of the rate of temperature change is the sum of (1) the rate of change of internal energy in the fuel cell body, and (2) the partial derivatives of the internal energy with respect to temperature in the anode and cathode.

Modified Anode Modeling Methodology

Although the model by was simplified by lumping all of these control volumes into a single thermal CV, four values in the anode model, (1) the mass of the anode gases

multiplied by specific heat capacity (2) the partial derivative of the internal energy in the anode with respect to mass, (3) the enthalpy flow into the anode channel, and (4) the enthalpy flow out of the anode channel, need to be calculated.

Masses in the anode channel consist of hydrogen, water vapor, and potentially liquid water. Specific heats of these gas species are assumed to be constant. Therefore the first two terms can be expanded as follows:

$$\sum m_{an} C_{van} = m_{H_2} C_{vH_2} + m_{vap} C_{vvap} + m_{liq} C_{liq} \tag{53}$$

$$\left(\sum \frac{dm_{an}}{dt} C_{van} \right) T_{FC} = \left(\dot{m}_{H_2} C_{vH_2} + \dot{m}_{vap} C_{vvap} + \dot{m}_{liq} C_{liq} \right) T_{FC} \tag{54}$$

In the original model, inlet enthalpies entering the anode control volume consist of the hydrogen and vapor masses from the anode inlet, as well as the vapor and liquid masses that cross the membrane. However, since we use one control volume to represent both the anode and cathode channel temperatures, all the mass crossing the membrane is internal to the CV and can be left out of the calculation:

$$H_{an,in} = \left(\dot{m}_{H_2,in} C_{vH_2} + \dot{m}_{vap,in} C_{vvap} \right) T_{an,in} \tag{55}$$

The enthalpy out of the system consists of the hydrogen and vapor masses leaving the anode and the reacted hydrogen mass:

$$H_{an,out} = \left(\dot{m}_{H_2,out} C_{vH_2} + \dot{m}_{vap,out} C_{vvap} + \dot{m}_{H_2,reac} C_{vH_2} \right) T_{FC} \tag{56}$$

Modified Cathode Modeling Methodology

The changes to the cathode model are similar to those in the anode model. Four terms still need to be calculated in the cathode model; (1) the mass of the cathode gases

multiplied by their corresponding specific heat capacity (2) partial derivatives of the internal energy in the cathode with respect to the species masses, (3) the inlet enthalpies and (4) outlet enthalpies of cathode channel. Knowing that the mass in the cathode CV consists of air, water vapor, and potentially liquid water, the first two terms were expanded as.

$$\sum m_{ca} C_{vca} = m_{O_2} C_{vO_2} + m_{N_2} C_{vN_2} + m_{vap} C_{vvap} + m_{liq} C_{liq} \tag{57}$$

$$\left(\sum \frac{dm_{ca}}{dt} C_{vca} \right) T_{FC} = \left(\dot{m}_{O_2} C_{vO_2} + \dot{m}_{N_2} C_{vN_2} + \dot{m}_{vap} C_{vvap} \right) T_{FC} \tag{58}$$

Similarly to the anode calculations, the cathode flow enthalpies are expressed as:

$$H_{ca,in} = \left(\dot{m}_{O_2,in} C_{vO_2} + \dot{m}_{N_2,in} C_{vN_2} + \dot{m}_{vap,in} C_{vvap} \right) T_{ca,in} \tag{59}$$

$$H_{ca,out} = \left(\dot{m}_{O_2,out} C_{vO_2} + \dot{m}_{N_2,out} C_{vN_2} + \dot{m}_{vap,out} C_{vvap} + m_{O_2,reac} C_{vO_2} \right) T_{FC} \tag{60}$$

As there are still 6 CVs remaining in the cathode channel, the first term is the sum of the specific heat capacities in all six CVs:

$$\sum m_{ca} C_{vca} = \sum m_{O_2} C_{vO_2} + \sum m_{N_2} C_{vN_2} + \sum m_{vap} C_{vvap} + \sum m_{liq} C_{liq} \tag{61}$$

With the simplified thermal model, the enthalpy flow into the lumped CV is that coming into the first CV and the enthalpy gained from the vapor generated in all 6 CVs. The enthalpy flow out of the lumped CV is that leaving the last CV, as well as the enthalpy loss from the reacted oxygen in all 6 CVs.

$$\begin{aligned} \left(\sum \frac{dm_{ca}}{dt} C_{vca} \right) T_{FC} = (& \dot{m}_{O_2 in} C_{vO_2} + \dot{m}_{N_2 in} C_{vN_2} + \dot{m}_{vapin} C_{vvap} - \dot{m}_{O_2 out} C_{vO_2} \\ & - \dot{m}_{N_2 out} C_{vN_2} - \dot{m}_{vapout} C_{vvap} + \sum \dot{m}_{O_2 rec} C_{vO_2} + \sum \dot{m}_{vapgen} C_{vvap}) T_{FC} \end{aligned} \tag{62}$$

Simulation Results and Discussion

To test the validity of the method, the responses using multiple thermal CVs were compared to the response using a single representative temperature, focusing particularly on the overall and distributed RH and voltage responses. To be valid, the modification to the model should not have any noticeable effect on the original modeling accuracy.

Figure 29 reveals that the agreement with the experimental RH data is good using both models. While there is some difference between the experimental and simulated values, both simulation methodologies yield the same results. This shows the validity of the new methodology, in that it does not affect the prediction of the outlet RH. This suggests that the prediction of at least the last CV in the model is accurate, but the RH prediction from the earlier CVs is still in question given that the lack of multiple temperature states will affect these most significantly.

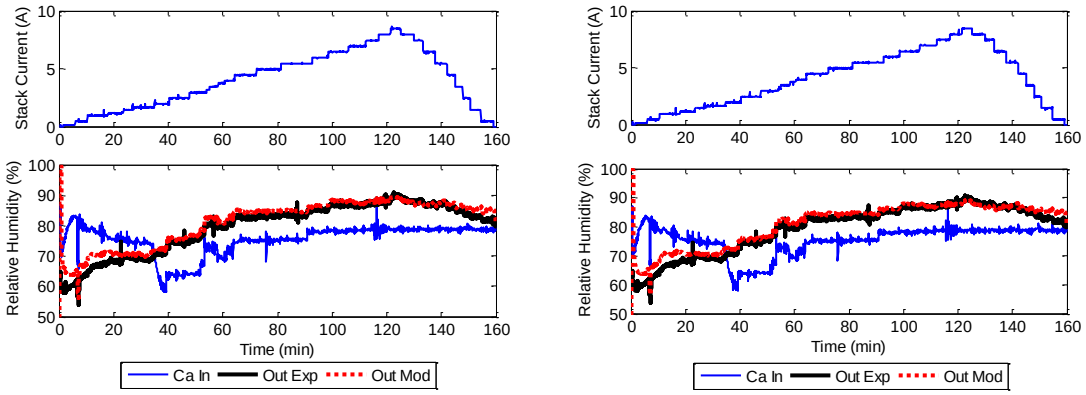

FIGURE 29: RELATIVE HUMIDITY RESPONSE SINGLE TEMPERATURE CV MODEL (LEFT) INDIVIDUAL TEMPERATURE CVS MODEL (RIGHT)

Figure 30 shows that the single temperature CV model slightly alters the RH response in CV_1 as compared to the individual temperature CV model. This is caused by a

slightly different modeled temperature in CV_1, which seems to be the only one affected significantly by the model reduction.

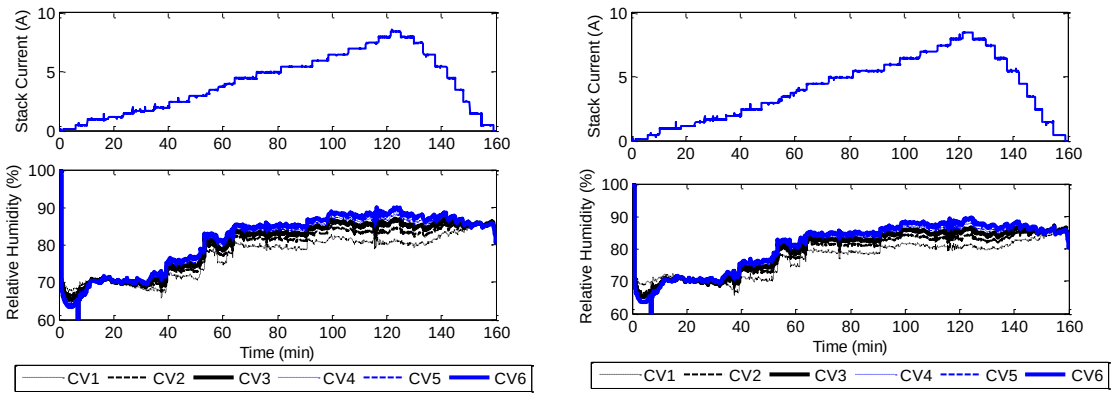

FIGURE 30: DISTRIBUTED RELATIVE HUMIDITY RESPONSE SINGLE TEMPERATURE CV MODEL (LEFT) INDIVIDUAL TEMPERATURE CVS MODEL (RIGHT)

Figure 31 shows the comparison of the stack voltage response from each model with experimental results.

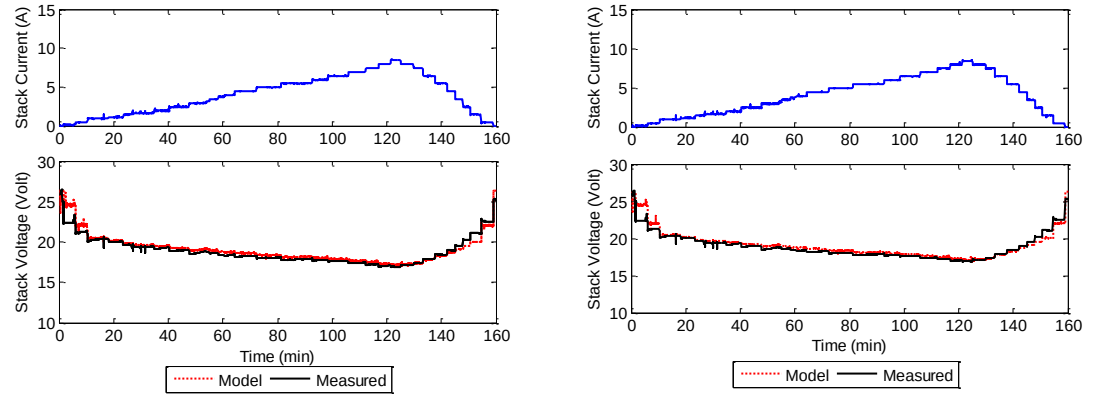

Figure 31: Voltage Response Single Temperature CV Model (Left) Individual Temperature CVs Model (Right)

This shows that the simulation results of both methodologies deviate slightly from the experimental data at the beginning and end of the test cycle, but are very accurate for

the bulk of the experiment. However, it can be seen in this figure that the new model is no less precise than the original individual temperature CV model.

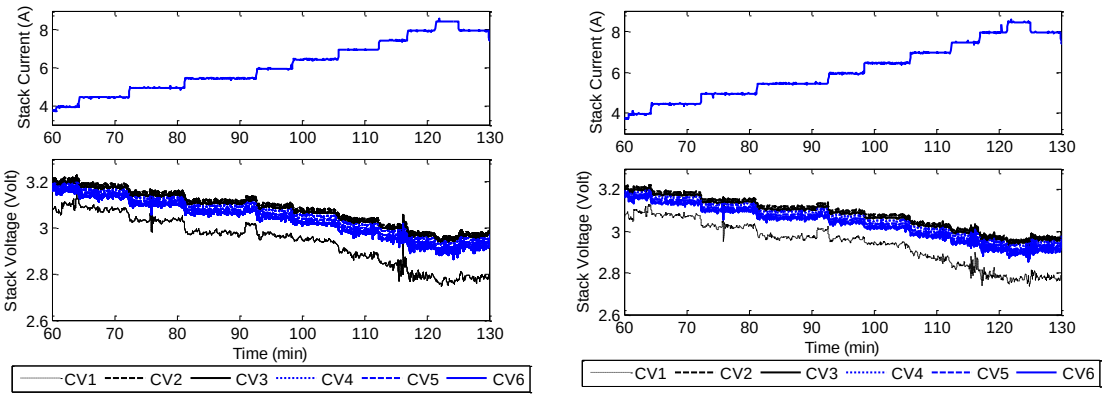

FIGURE 32: DISTRIBUTED VOLTAGE RESPONSE SINGLE TEMPERATURE CV MODEL (LEFT) INDIVIDUAL TEMPERATURE CVS MODEL (RIGHT)

Figure 32 shows the modeled voltage response from each CV. This figure shows that the distributed voltage response does not show any significant change with the new modeling methodology, including in CV_1, which has a slightly different temperature value in the two models. As such, we see that the modified model can provide the necessary insight into the individual CV voltage responses.

All of these figures suggest that the impact of reducing the number of temperature states is negligible, and that the reduced order model can be used confidently for predictions and control design of our system.

Computational Expense Reduction

After testing the reliability of the reduced order model, we compared the calculation time of four different models: 1) the original 6 individual temperature CVs model, 2) a one CV mass model (i.e. 1 CV is used to represent the masses in the cathode channel as well),

3) the reduced order single temperature CV model presented in this section, and 4) a cleaned version (removal of scopes used for tuning the Simulink model, etc.) of the reduced order model. The results are shown in Table 8.

The reduced order single temperature CV model we created reduced the computation time by approximately 40%. With additional model clean up in Simulink, the time was reduced by as much as 80% versus the original model. The calculation time of the reduced order, distributed model is still longer than the traditional, fully lumped model, but the added accuracy of the RH model justifies this slight increase.

Table 8: Modeling time for each model iteration

Model Type	Full Experiment Simulation (9600 sec)	Initializing Period (1st 200 sec)	Percent Reduction (full experiment)
Original	130.4948	59.7328	----
One CV Mass Model	14.8669	2.6832	88.6%
Reduced Order	81.6977	31.8242	37.4%

Chapter IV: Analysis of the Relative Humidity Profile in the Cathode Channel

MOTIVATION

As highlighted in previous sections, the use of six, evenly spaced CVs for the mass balance model, as shown in Figure 33, captures the spatial variations in the operating conditions within a fuel cell stack.

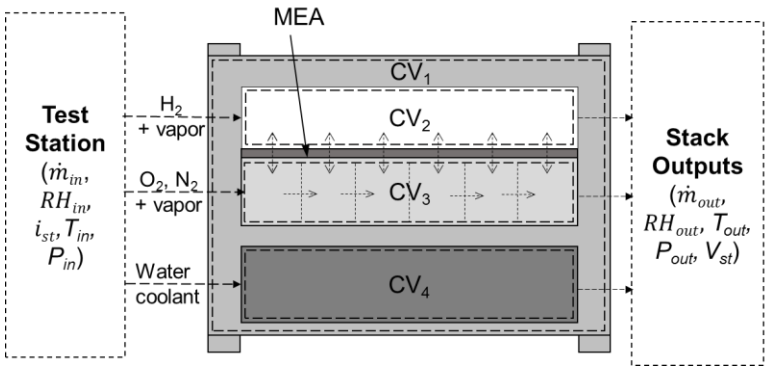

FIGURE 33: REPRESENTATIVE CONTROL VOLUMES OF A FUEL CELL STACK (CV_1: FUEL CELL BODY & MEA, CV_2: ANODE, CV_3: CATHODE, CV_4: COOLANT WATER) [76]

As discussed in Chapter II, this modeling methodology makes it possible to account for the accumulation of vapor towards the end of the stack, without an unreasonable increase in the computational expense. The experimental validation also showed that the multi-CV approach was necessary to properly predict flooding issues towards the outlet cells of the cathode channel.

However, given the inherent nonlinear profile of the RH in the channel, evenly spaced CVs cannot optimally represent the vapor distribution. Also, though a trial-and-error study was previously performed to select six CVs for this purpose, it was unclear

whether this was a truly optimal use of computation power. Additionally, modeling results of the RH, such as those shown in Figure 30 show that the predicted response of the last few CVs begins to converge, which implies that perhaps some portion of the stack model could be lumped without a significant loss in accuracy. To address these questions and maximize the use of our computational efforts, a fundamental understanding of the RH profile and all of its contingencies was necessary. This section highlights an analytical solution of the RH profile in the fuel cell stack to be used for model optimization.

METHODOLOGY

The analysis of the temperature profile in the cathode channel was a necessary prerequisite to analyzing the RH profile in the stack. Given the strong temperature dependence of RH on the local temperature, a full understanding of the RH profile could not be obtained without first understanding the spatial variations in temperature. Fortunately, one major takeaway from the thermal analysis was that the temperature is very nearly that of the fuel cell body for the entire length of the channel. As such, we could treat this as a constant for the analysis.

First, it should be noted that the analytical solution could be used in multiple ways for control design. For example, knowledge of the RH profile could be used to appropriately size CVs for the dynamic voltage, RH, and thermal model. This would in turn allow the model to function more appropriately. To simplify the analysis, the following assumptions were made:

1) The analysis was performed for the steady state RH profile. Note that though there is a temporal overshoot in RH in response to step changes in current, Zhang et al. showed that the steady state value is reached in approximately ten seconds [77]. This could be even less depending on the cross flow velocity in the channels. Therefore, any vapor concentration in excess of the steady state value should dissipate fairly quickly. This means that the analytical solution can be used for a wide range of control decisions.
2) The cross-flow velocity is constant along the entire length of the channel.
3) The gas temperature along the length of the channel is constant. This assumption is supported by the temperature profile analysis in the previous section.
4) The anode RH is known and constant along the length of the stack. Recall that for our model, which has been shown to closely match experimental results, the anode is lumped into a single CV. Though the anode RH changes with time, within the model, this value is always known and can be used to predict the RH profile accordingly.

With these assumptions in mind, we began the analysis from the water conservation equation for the cathode channel in one dimension as follows:

$$\left(A\cdot u\cdot \rho\right)_x - \left(A\cdot u\cdot \rho\right)_{x+dx} + \frac{\dot{m}_{gen,tot}}{V}\cdot A\cdot dx + \dot{m}''_{drag}\cdot w\cdot dx + \dot{m}''_{diff}\cdot w\cdot dx = 0 \qquad (63)$$

where A is the cross-sectional area of the channel, V is the total volume of the cathode channel in the stack, u is the bulk flow velocity in the x-direction, ρ is the density of water, and w is the width of the channel.

The five terms in Eqn. (63) correspond to: 1) vapor flow into the differential element (DE) due to bulk fluid motion, 2) vapor flow out of the DE due to bulk fluid motion, 3) water vapor generated in the DE, 4) vapor flow into the DE due to electro-

osmotic drag through the membrane, and 5) vapor flow into the DE due to concentration-gradient-based diffusion. Assuming that the bulk flow velocity is constant, the first two terms of Eqn. (63) can be rewritten as:

$$Au\left(\rho_x - \rho_{x+dx}\right) = -Au\frac{d\rho}{dx}\cdot dx \tag{64}$$

This formulation is then substituted into the original conservation equation to yield the following equation:

$$-Au\frac{d\rho}{dx}\cdot dx + \frac{\dot{m}_{gen,tot}}{V}\cdot A\cdot dx + w\cdot dx\left(\dot{m}_{drag}'' + \dot{m}_{diff}''\right) = 0 \tag{65}$$

Dividing Eqn. (65) by $-Audx$ and re-arranging to isolate the derivative of the density with respect to x yields:

$$\frac{d\rho^*}{dx} = \frac{1}{u}\left[\frac{\dot{m}_{gen,tot}}{V} + \frac{\dot{m}_{diff}'' + \dot{m}_{drag}''}{h}\right] \tag{66}$$

where h is the height of the channel, and ρ^* is defined by:

$$\begin{aligned}\rho^* &= \rho_{ca} - \rho_{an}\\ \frac{d\rho^*}{dx} &= \frac{d\rho_{ca}}{dx}\end{aligned} \tag{67}$$

The generation and drag terms in Eqn.(66) are heavily dependent on the current, while the osmotic diffusion term depends on the local concentration gradient between the cathode and anode. For the final solution, it is helpful to treat these components separately. First we will present the analysis for the osmotic diffusion term.

Concentration Gradient Based Vapor Diffusion

The rate equation for the osmotic diffusion can be expressed as [78]:

$$\dot{m}_{diff} = -M_{H_2O} D_w \frac{c_{ca} - c_{an}}{t_m} \tag{68}$$

where M_{H_2O} is the molar mass of water, D_w is the diffusion coefficient through the membrane, t_m is the membrane thickness, and c is the vapor concentration defined as [78]:

$$c = \frac{\rho_{memb,dry}}{W_{eq,memb,dry}} \lambda \tag{69}$$

The membrane water content, λ, is a function of the local vapor activity and has been approximated with the following form [79]:

$$\lambda_i = \begin{cases} 0.043 + 17.81 a_i - 39.85 a_i^2 + 36.0 a_i^3 & ,0 < a_i \le 1 \\ 14 + 1.4(a_i - 1) & ,1 < a_i \le 3 \end{cases} \tag{70}$$

where a_i is the activity, or RH, in channel i, defined as:

$$RH = \frac{\rho}{\rho_{sat}} \tag{71}$$

where ρ_{sat} is the vapor saturation density at the given temperature of the environment. The dependency of the diffusion term on λ over the range of interest ($0<a_i\le1$) makes it difficult to obtain a closed form solution of Eqn. (66) that could be used in any meaningful, real-time applications. To circumvent this issue, Eqn. (70) was linearized over two domains ($0<a_i\le0.7$ and $0.7<a_i\le1.0$) as shown in Figure 34.

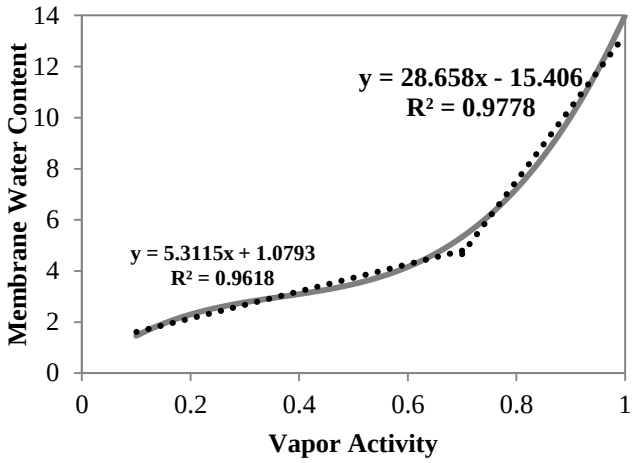

FIGURE 34: LINEARIZATION OF THE MEMBRANE WATER CONTENT WITH RESPECT TO THE VAPOR ACTIVITY; $0<A_i\leq 1$

Linearizing the membrane water content in this fashion linearizes the osmotic diffusion component of Eqn. (66). This component can then be written in the following form:

$$\lambda_i = m_\lambda \left(\frac{\rho_i}{\rho_{sat}} \right) + b_\lambda \tag{72}$$

$$\begin{aligned} \dot{m}_{diff} &= -\frac{M_{H_2O} D_w}{t_m} \frac{\rho_{memb,dry}}{W_{eq,memb,dry}} \left[m_\lambda \left(\frac{\rho_{ca}}{\rho_{sat}} \right) - m_\lambda \left(\frac{\rho_{an}}{\rho_{sat}} \right) \right] \\ &= -\frac{M_{H_2O} D_w}{t_m} \frac{\rho_{memb,dry}}{W_{eq,memb,dry}} \frac{m_\lambda}{\rho_{sat}} \rho^* \end{aligned} \tag{73}$$

For convenience in the final solution, a coefficient D^* is defined as:

$$D^* = -\frac{M_{H_2O} D_w}{uht_m} \frac{\rho_{memb,dry}}{W_{eq,memb,dry}} \frac{m_\lambda}{\rho_{sat}} \tag{74}$$

Current Dominated Vapor Diffusion and Generation

The vapor generation and electro-osmotic drag terms in Eqn. (66) are both heavily dependent on the current demand in the stack. The functional form for these two terms is [78]:

$$\dot{m}_{gen} = M_{H_2O} \frac{I_{st}}{2F} \cdot n_{cells} \tag{75}$$

$$\dot{m}_{drag}'' = M_{H_2O} n_d \frac{I_{st}}{A_{FC} F} \tag{76}$$

where I_{st} is the stack current, n_{cells} is the number of cells in the stack, F is Faraday's constant, A_{FC} is the membrane active area, and n_d is the electro-diffusion coefficient. These terms were incorporated into Eqn.(66), and the current dependent terms were combined into a single term for further analysis as

$$I^{**} = \frac{M_{H_2O} \cdot I_{st}}{uF} \left(\frac{n_{cells}}{2V} + \frac{n_d}{hA_{FC}} \right) \tag{77}$$

Both of the terms in Eqn. (77) would be entirely dependent on the current if not for the dependence of n_d on the membrane water content [70] given by

$$n_d = 0.0029\lambda_m^2 + 0.05\lambda_m - 3.4\times10^{-19} \tag{78}$$

where λ_m is the membrane water content, which in the model is assumed to be the average of the anode and cathode water contents. Again, to enable the calculation of a closed form solution for the profile, Eqn. (78) was linearized in the following form:

$$n_d = m_{n_d} \lambda_m + b_{n_d} \tag{79}$$

where the coefficients m_{nd} and b_{nd} were obtained from a linear regression of Eqn. (78) as shown in Figure 35.

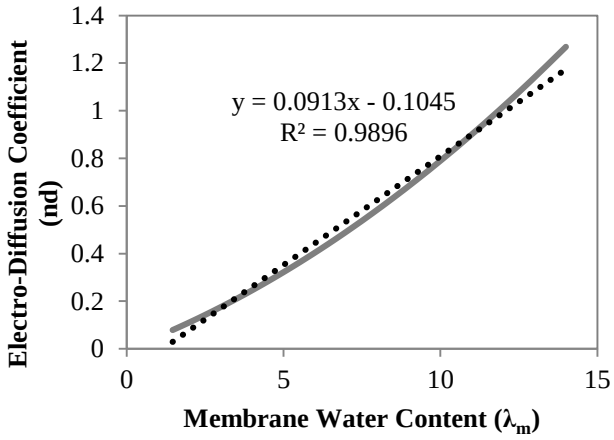

FIGURE 35: LINEARIZATION OF THE ELECTRO-DIFFUSION COEFFICIENT WITH RESPECT TO THE MEMBRANE WATER CONTENT

Incorporating Eqns. (79) and (72) into Eqn. (77) and rearranging to put the equation in terms of ρ^* yields:

$$I^{**} = \frac{M_{H_2O} \cdot I_{st}}{uF}\left(\frac{n_{cells}}{2V} + \frac{m_{n_d}\lambda_{an}}{2hA_{FC}} + \frac{m_{n_d}m_\lambda\rho_{an}}{2hA_{FC}\rho_{sat}} + \frac{m_{n_d}b_\lambda}{2hA_{FC}} + \frac{b_{n_d}}{hA_{FC}}\right) + \frac{M_{H_2O} \cdot I_{st}}{uFhA_{FC}}\frac{m_{n_d}m_\lambda}{2}\left(\frac{\rho^*}{\rho_{sat}}\right) \quad (80)$$

As you can see, I^{**} has one component that is entirely dependent on the current, and a second that is dependent on both the current and local water vapor density in the cathode (ρ^*). Equation (80) was re-written as a vapor-density-dependent coefficient and a vapor density independent term as

$$I^*_{\rho_{ca}} = \frac{M_{H_2O} \cdot I_{st}}{uhA_{FC}F}\frac{m_{n_d}m_\lambda}{2\rho_{sat}} \quad (81)$$

$$I^* = \frac{M_{H_2O} \cdot I_{st}}{uF}\left(\frac{n_{cells}}{2V} + \frac{m_{n_d}\lambda_{an}}{2hA_{FC}} + \frac{m_{n_d}m_\lambda\rho_{an}}{2hA_{FC}\rho_{sat}} + \frac{m_{n_d}b_\lambda}{2hA_{FC}} + \frac{b_{n_d}}{hA_{FC}}\right) \tag{82}$$

Final RH Profile Solution

Using the formulations described above, Eqn. (66) can be re-written as

$$\frac{d\rho^*}{dx} = I^* - K^*\rho^* \tag{83}$$

where K^* is comprised of the terms that are dependent on the local vapor density, and is defined as

$$K^* = -\left(D^* + I^*_{\rho_{ca}}\right) \tag{84}$$

It should be noted here that D^* is a negative term and larger in magnitude than $I^*_{\rho_{ca}}$, making K^* a positive number. Equation (83) can then be solved directly to obtain the vapor density as a function of the channel location given by

$$\rho(x) = Ae^{-K^*x} + \frac{I^*}{K^*} + \rho_{an} \tag{85}$$

where A can be determined from the inlet boundary condition

$$\rho(0) = \rho_{ca,in} \Rightarrow A = \rho_{ca,in} - \rho_{an} - \frac{I^*}{K^*} \tag{86}$$

Finally, the RH profile can be found by dividing Eqn. (86) by the vapor saturation density:

$$RH(x) = \frac{Ae^{-K^*x} + \frac{I^*}{K^*} + \rho_{an}}{\rho_{sat}} \tag{87}$$

where the vapor density is a function of the cathode channel temperature.

This gives a succinct solution for the RH profile in the stack that could be used in a number of ways to improve modeling and control strategies of PEM fuel cells. The following section shows the response of the analytical solution to various changes in the inlet conditions and current.

Analytical Modeling Results

To substantiate the viability of the analytical solution, the results of the analytical equation were compared to results calculated by our model. Fundamentally, the vapor density calculated for a lumped CV should be equal to the weighted averaged density of the analytical solution over the length of the CV, which is calculated as:

$$\rho_w = \frac{\int_{L_{n-1}}^{L_n} \rho(x)dx}{L_n - L_{n-1}} = \frac{\frac{-A}{K^*}\left(e^{-K^* L_n} - e^{-K^* L_{n-1}}\right)}{L_n - L_{n-1}} + \frac{I^*}{K^*} + \rho_{an} \tag{88}$$

The lumped model uses six, equally sized CVs to represent the 30 cell cathode channel. The following figures compare the RH in each CV from the model to the analytical, weighted average RH for each CV with various loads and stack conditions. For the percent error calculations, the analytical solution was averaged over the length of each corresponding CV (5 cells per CV, 1.7m serpentine channel/cell). Currents and air flow rates were chosen for the simulations such that a wide RH range would be covered, but no flooding would occur. Figure 36 compares the analytical and simulated profiles in a relatively low current and flow rate situation. For this and all following comparisons, the

model was run to steady state, and the simulated temperature and anode RH were used for the analytical profile solution.

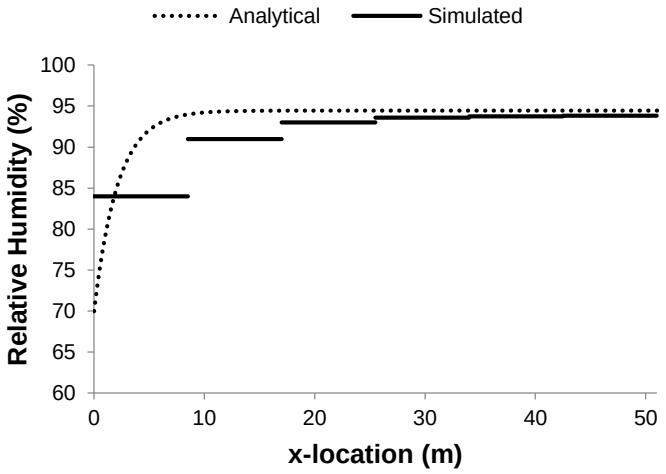

CV #	1	2	3	4	5	6
%DIFF	-3.06%	-1.65%	0.28%	0.85%	1.02%	1.07%

FIGURE 36: ANALYTICAL PROFILE AND SIMULATION COMPARISON OF CALCULATED RH IN 6 EVENLY SPACED CVS (T_{FC} = 345.77K, 3A DEMAND, $RH_{,AN}$ = 89.95%, $RH_{,IN}$=70%, 5 LPM INLET FLOW RATE)

The simulated response and analytical weighted average relative humidities are in close agreement for all six CVs representing the stack. The largest error, 3.06%, occurred with the first CV, where the largest RH gradient occurs. As the vapor content changes along the length of the stack, the pressure, and therefore the flow velocity, will change somewhat in the model as well, leading to a slight discrepancy. Regardless, this error is sufficiently small such that the analytical solution can be confidently used to modify the current fuel cell model.

Figure 37 and Figure 38 compare the analytical and simulated solutions in two cases with higher current demands and flow rates. The flow rates were increased for these

simulations to ensure that flooding conditions would be avoided for demonstration purposes.

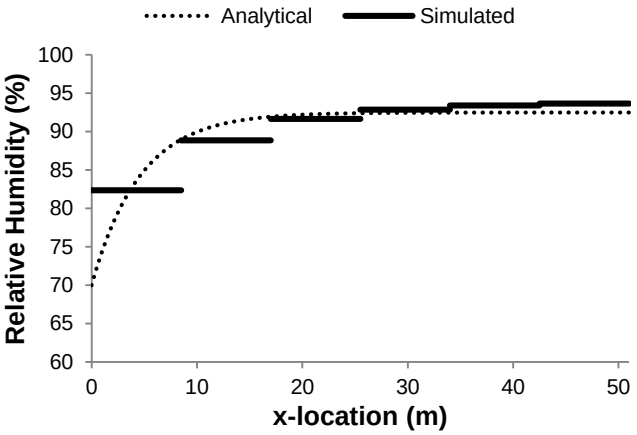

CV #	1	2	3	4	5	6
%DIFF	0.15%	-2.25%	-0.63%	0.47%	1.02%	1.27%

FIGURE 37: ANALYTICAL PROFILE AND SIMULATION COMPARISON OF CALCULATED RH IN 6 EVENLY SPACED CVS (TFC = 347.75 K, 5 A DEMAND, $RH_{,AN}$ = 88.2%, $RH_{,IN}$ = 70%, 10 NLPM INLET FLOW RATE)

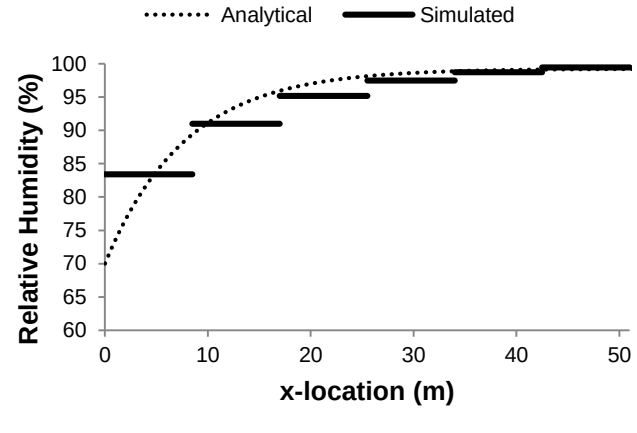

CV #	1	2	3	4	5	6
%DIFF	2.40%	-2.47%	-2.17%	-1.13%	-0.29%	0.27%

FIGURE 38: ANALYTICAL PROFILE AND SIMULATION COMPARISON OF CALCULATED RH IN 6 EVENLY SPACED CVS (TFC = 351.12 K, 10 A DEMAND, $RH_{,AN}$ = 90.1%, $RH_{,IN}$ = 70%, 15 NLPM INLET FLOW RATE)

It can be seen that the analytical solution is in good agreement with the simulated results in all cases. The largest error tends to be seen in CVs 1 or 2, where the majority of the increase in the RH occurs. This could also be due to the inaccuracy of the membrane

water content linearization around 70% RH. However, the peak RH predicted by both the analytical solution and model simulations were in close agreement for all the cases tested.

These results could have significant real-time control applications for PEM fuel cells. Firstly, the ratio I^*/K^* gives the maximum increase in the vapor density from the anode channel RH, and relates the flow rate, current, and saturation density (i.e. temperature) in a single term. This information could be used to determine the proper flow rate and inlet RH needed to avoid flooding issues at the end of the channel given the current demand and stack conditions. The analytical solution can also be used to size CVs in the model such that they remain within a critical accuracy band of the actual RH profile.

Effect of Varying Various Inputs

The analytical solution varies depending on the inlet flow rate, temperature, current, and the vapor density in the anode channel. Recall that in the model, the anode is treated as a single lumped CV across the entire stack. Thus, it can be treated as a known value at any time during the simulation. The following simulations show the response of the analytical solution to various changes to the key parameters. For all of these simulations, the anode RH was fixed at 85%. Figure 39 shows the response of the analytical solution to increasing currents.

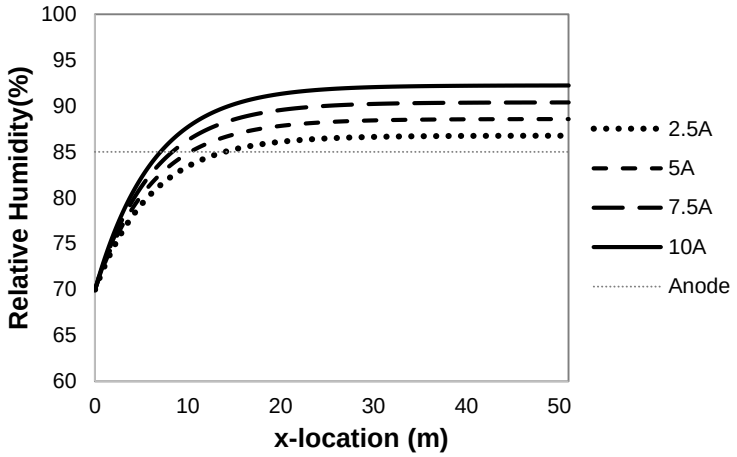

FIGURE 39: ANALYTICAL PROFILE RESPONSE TO VARYING CURRENT DEMANDS (T_{FC} = 348.15 K, $RH,_{IN}$ = 70%, INLET FLOW =15 NLPM)

As expected, the final value of the RH in the channel increases with the load, though the overall shape of the curve is largely unchanged. This is due to the accumulation of generated water vapor towards the end of the channel, and the eventual balance that is created between the rate of vapor generation and the rate of vapor transfer to the anode by diffusion.

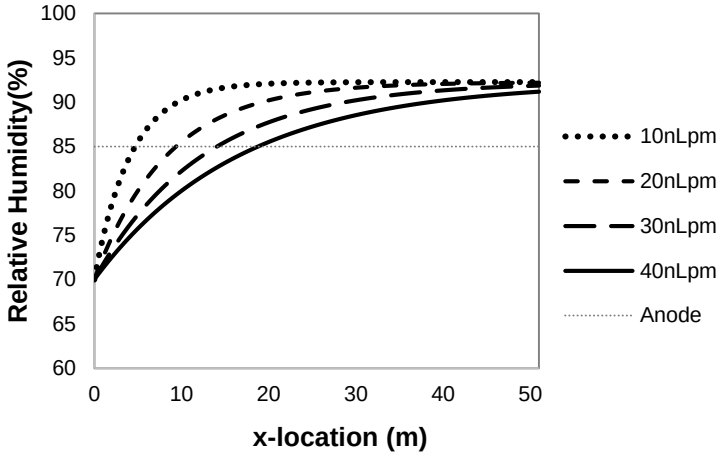

FIGURE 40: ANALYTICAL PROFILE RESPONSE TO VARYING THE CATHODE INLET FLOW RATE (T_{FC} = 348.15 K, $RH,_{IN}$ = 70%, IST = 10 A)

Figure 40 shows the response of the model to changes in the bulk flow rate in the cathode. Increasing the flow rate generally flattens the RH profile, and pushes lower humidities further into the channel. With sufficiently large flow rates, the peak RH can be reduced in the channel, though the peak value would still be obtained in a sufficiently long channel.

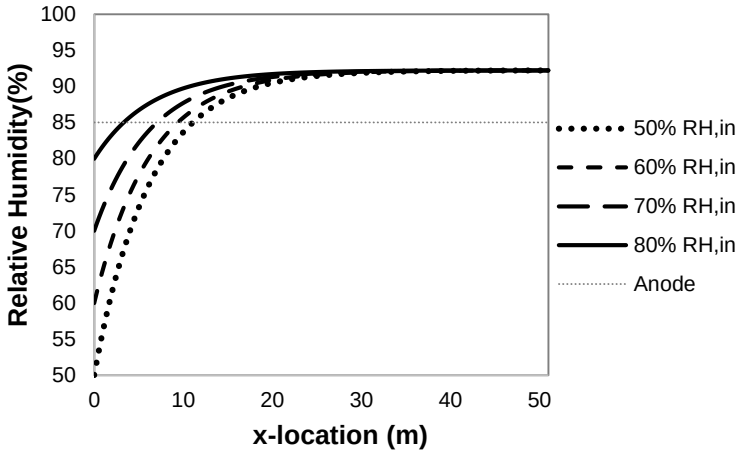

FIGURE 41: ANALYTICAL PROFILE RESPONSE TO VARYING THE CATHODE INLET RELATIVE HUMIDITY (T_{FC} = 348.15 K, I_{ST} = 10 A, INLET FLOW = 15 NLPM)

Figure 41 shows the response of the RH profile to changing the inlet relative humidity. According to the analysis presented previously, this change only affects the boundary condition, and not the final value of the channel RH, as shown in the figure. The relative humidity reaches the same peak value in all cases, though with lower inlet humidities, this value is reached slightly further down the channel. Recall, however, that for these simulations, the anode RH is fixed. In real stack operation, increasing the flow rate or reducing the RH at the cathode inlet would also reduce the steady state anode humidity, which would decrease the peak RH as well. The intent of this analysis is to augment the current fuel cell model to improve the RH simulations. The current model has

been shown to accurately model the system response using a single CV to represent the anode. Therefore, the anode RH calculated by the model could be used with this analytical solution to size the CVs in the cathode channel, which would in turn greatly improve the distributed RH simulation in the cathode channel. This will be demonstrated later in the dissertation.

SIZING METHODOLOGY USING THE RH PROFILE

Similarly to the algorithm presented previously for the sizing of control volumes to improve the temperature modeling, the 1D RH profile will be used here to size control volumes to improve the RH modeling. To calculate the CV sizes, a critical difference between the RH predicted in a control volume and the actual RH profile needs to be chosen. Given this, the control volume length can then be determined by limiting the weighted average RH over the CV length to be within the specified accuracy requirement.

Using the definition of the weighted average vapor density shown in Eqn.(88), which was shown in the previous section to correspond to the RH predicted for a given CV, a criteria can be specified to determine the proper CV length. Because the gradient of the RH profile decreases along the stack, the RH at the beginning of the CV will differ from the weighted average RH by the largest amount. Therefore, the accuracy requirement limits the difference between the RH at the beginning of the CV and the weighted average RH:

$$\left|RH(L_{n-1}) - RH_w\left(L_{n-1} \rightarrow L_n\right)\right| \leq \Delta RH_{crit}$$

$$\left|\frac{Ae^{\left(-K^* L_{n-1}\right)}}{\rho_{sat}} + \frac{A\left(e^{\left(-K^* L_n\right)} - e^{\left(-K^* L_{n-1}\right)}\right)}{K^*\left(L_n - L_{n-1}\right)\rho_{sat}}\right| \leq \Delta RH_{crit} \tag{89}$$

This criteria can be solved numerically to select CV lengths to satisfy the specification. The following figures show the CV sizes that would be selected for a scenario similar to that during the tests shown in Chapter II. To size these control volumes, the critical RH error (ΔRH_{crit}) was selected to be 3% to maximize the usefulness of a six CV model over the RH range covered. However, depending on the application, this value could be determined by a number of criteria, such as the desired number of CVs, situation of interest to be modeled, etc. Six CVs are still being used here as this number was previously found to yield far more information without an excessive increase in computational expense [76], but the total number could be determined by ΔRH_{crit} if this value was known a priori.

As shown in Figure 42 this sizing methodology locates the majority of the control volumes to the CVs towards the cathode inlet where the RH rises most drastically. In fact, the first two CVs would be limited almost entirely to the first two cells in our stack using this methodology. This corresponds to the problem areas that were seen during the experiment shown in Figure 26.

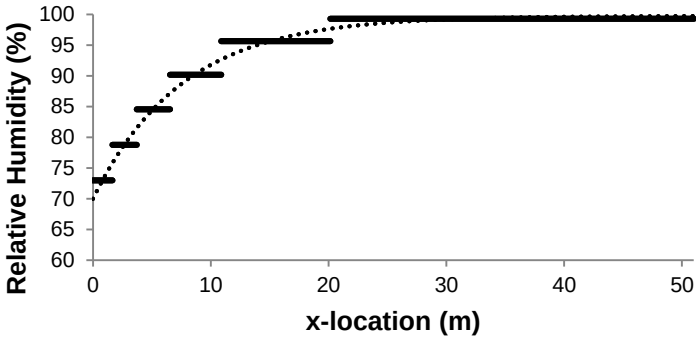

CV#	1	2	3	4	5	6
L_n	1.644	3.722	6.539	10.883	20.149	51
L_{n-1}	0.000	1.644	3.722	6.539	10.883	20.149

FIGURE 42: UNEVENLY SPACED CV SIZING ALGORITHM RESULTS (T_{FC}=352K, 7A DEMAND, RH,AN = 90%, RH,IN=70%, 15NLPM INLET FLOW RATE)

To show the adaptability of this CV sizing method to varying loads, another case with a much lower flow rate was sized using this algorithm. This case is a particularly poor candidate for evenly sized CVs, as a large majority of the RH increase occurs in a short space. For this simulation, ΔRH_{crit} was set to 2.5% to maximize the usefulness of a six CV model.

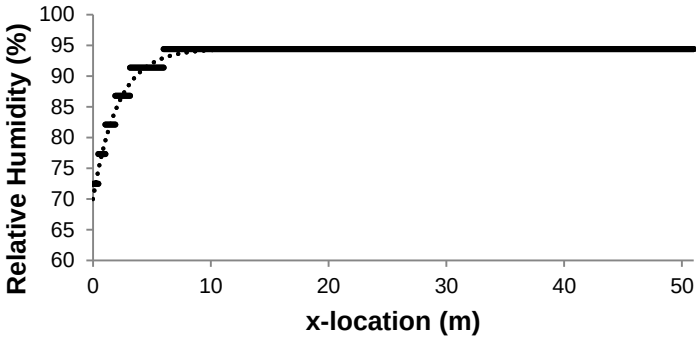

CV#	1	2	3	4	5	6
L_N	0.471	1.070	1.886	3.162	6.006	51
L_{N-1}	0.000	0.471	1.070	1.886	3.162	6.006

FIGURE 43: UNEVENLY SPACED CV SIZING ALGORITHM RESULTS (T_{FC}=345.77K, 3A DEMAND, RH,AN = 89.95%, RH,IN=70%, 5NLPM INLET FLOW RATE)

The CVs are confined to an even smaller space in the channel; the first three CVs are limited almost completely to the length of the first cell. While this would yield a more appropriate representation of the first cell, there could be diminishing returns given the extremely short length of the first few CVs. In practical applications, a minimum CV length could be determined for the system to limit the additional computational expense for such small sections of the stack.

Defining a Correction Factor for Fully Lumped Model to Accurately Predict Flooding Conditions

Given the results of the vapor density profile analysis, a number of improvements could be made to the modeling methodology in addition to optimally re-sizing the CVs for multi-CV representations. Knowledge of the RH profile in the stack also makes it possible to improve the accuracy of the one CV model for RH modeling. As shown in Chapter II, the one CV model was not able to accurately predict the RH in the sensor housing as it could not account for the accumulation of water vapor that occurs towards the end of the stack. However, the analytical profile solution makes it possible to account for this accumulation by adding a dynamic correction factor to the one CV model prediction. This would make it possible to accurately predict and avoid flooding concerns using single CV representations, which inherently have a lower computational expense than multi-CV representations.

Equations for Adjustment

To show the validity of the analytical solution, we modified the one CV model using the information contained in Eqn. (87) to accurately predict the exit conditions measured during the experiments.

Fundamentally, the vapor density calculated for a lumped CV should be equal to the weighted averaged density of the analytical solution over the length of the CV, which is calculated as:

$$\rho_w = \frac{\int_{L_{n-1}}^{L_n} \rho(x)dx}{L_n - L_{n-1}} = \frac{\frac{-A}{K^*}\left(e^{-K^* L_n} - e^{-K^* L_{n-1}}\right)}{L_n - L_{n-1}} + \frac{I^*}{K^*} + \rho_{an} \tag{90}$$

As the one CV model prediction represents the weighted average of the vapor content over the entire channel, the vapor density at the end of the stack can be found by adding the difference between the weighted average density and the outlet density predicted by the analysis. This yields the following adjustment factor:

$$\begin{aligned} \rho_{adj} &= \rho_w - \rho_{end} \\ &= \frac{\frac{-A}{K^*}\left(e^{-K^* L_{end}} - 1\right)}{L_{end}} + \frac{I^*}{K^*} + \rho_{an} - \left[Ae^{-K^* L_{end}} + \frac{I^*}{K^*} + \rho_{an} \right] \\ &= \frac{\frac{-A}{K^*}\left(e^{-K^* L_{end}} - 1\right)}{L_{end}} - Ae^{-K^* L_{end}} \end{aligned} \tag{91}$$

The proper outlet vapor density can then be calculated as:

$$\rho_{out} = \rho_{mod,CV} + \rho_{adj} \tag{92}$$

Recall that the coefficients A and K^* depend on the characteristics of the flow and the current demand. As such, this method should be able to appropriately compensate for

the difference between the outlet and bulk vapor densities for all of the conditions seen during the experiments. Experimental data was used to validate the model augmentation. The section of the experiment with the highest current, and therefore the highest potential for error between the experiment and one CV model, is shown in Figure 44.

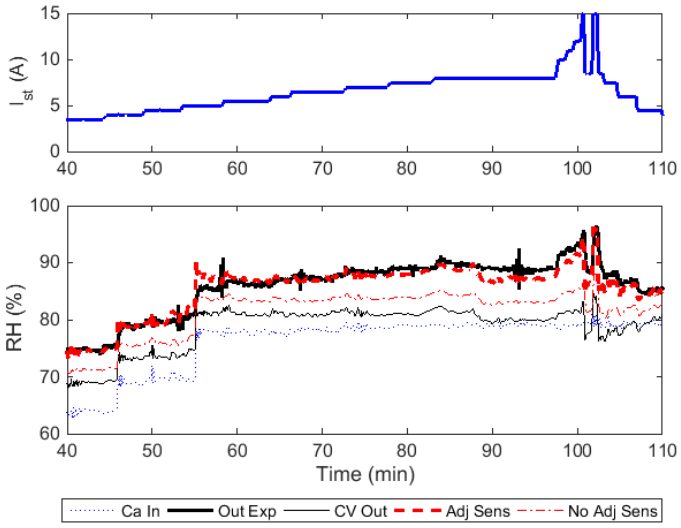

FIGURE 44: EXPERIMENTAL VALIDATION OF THE ONE CV MODEL ADJUSTMENT ALGORITHM – MAX LOAD TEST PHASE

Figure 44 shows the effectiveness of the vapor density correction of the RH response. The adjustment is particularly useful with high current loads, where one CV models are the most ineffective at predicting the vapor content at the outlet of the system due to the accumulation of generated water towards the stack outlet. This shows the efficacy of the analytical solution, and also suggests a means by which a one CV model with the proposed augmentation could be used for accurate flooding predictions.

Another useful metric for evaluating the vapor dynamics model is the dewpoint temperature. Unlike the relative humidity, the dewpoint temperature is only a function of the vapor partial pressure (i.e. vapor density) and is independent of the operating

temperature. Therefore, as the vapor density does not change between the sensor and fuel cell body, the result using the analytical adjustment to the vapor density can be directly compared to the experimental results, independently of the sensor housing temperature.

To calculate the dewpoint temperature in the model, the anode vapor density and water content, inlet volumetric flow rate, current, etc. are used to calculate the coefficients in Eqn. (85). The corrected outlet vapor density is then calculated from the Eqn. (92), and the adjusted vapor pressure is calculated as:

$$P_{w,adj} = \rho_{out} R_w T_{FC} \tag{93}$$

where R_w is the vapor gas constant and T_{FC} is the fuel cell temperature.

The dewpoint temperature is calculated using the following equation [81]

$$T_d = \frac{T_n}{\left[\frac{m}{{}^{10}log\left(\frac{P_w}{A} \right)} - 1 \right]} \tag{94}$$

where P_w is the vapor partial pressure in hPa, and T_n, m and A are constants that can be found in reference [81].

Figure 45 shows the result of the adjustment algorithm during the warm-up phase of the test where no load was applied in terms of the dewpoint temperature. This shows that the algorithm is also useful for correcting the outlet humidity for diffusion to the anode channel.

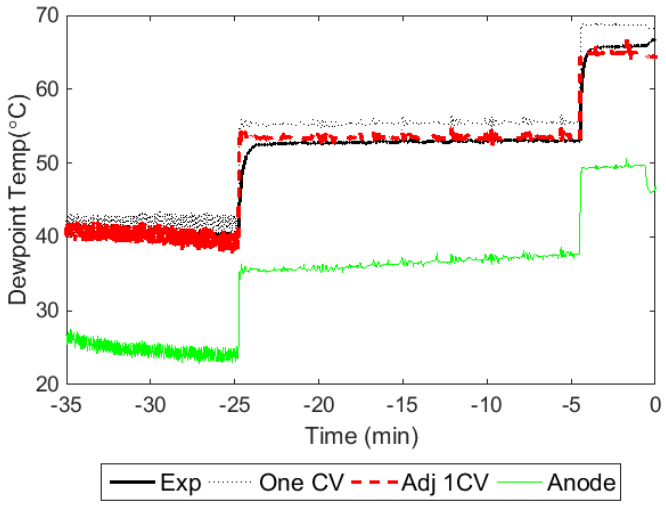

FIGURE 45: EXPERIMENTAL VALIDATION OF THE ONE CV MODEL ADJUSTMENT ALGORITHM – NO LOAD PRE-TEST

These results could have significant real-time control applications for PEM fuel cells. Firstly, the ratio I^*/K^* gives the maximum increase in the vapor density from the anode channel RH, and relates the flow rate, current, and saturation density (i.e. temperature) in a single term. This information could be used to determine the proper flow rate and inlet RH needed to avoid flooding issues at the end of the channel given the current demand and stack conditions. In addition to the corrections to a one CV model shown in this section, the analytical solution can also be used to size multiple CVs to remain within a critical accuracy band of the actual RH profile.

SUMMARY

First, a one-dimensional, steady state analytical solution for the relative humidity profile in a PEM fuel cell stack was solved for based on vapor mass conservations laws in the cathode channel. The solution adapts to account for changes in the temperature, inlet RH, flow rate, and current demand in the stack, making it applicable over a wide range of

operating conditions. The analytical solution also introduces a new coefficient that could be used for control decisions in fuel cell stacks. The ratio of I^* (vapor generation) to K^* (membrane crossover) governs the maximum increase in the vapor concentration from that in the anode channel. This ratio varies with the temperature, current, flow rate, etc. in the system, and could be easily implemented to determine the appropriate inlet flow conditions to avoid flooding.

Given the analytical profile solution, a sizing methodology was developed to improve control-oriented RH modeling in fuel cell stacks. If a critical accuracy requirement can be specified for the fuel cell stack in question, the length for each CV in the model can be determined numerically. These results could be used to significantly improve real-time modeling and control of PEM fuel cell stacks.

For instance, a correction factor can be determined from the analytical solution of the RH profile in the stack to improve the accuracy of lower order models. Previous research had shown that a model based on a single CV for estimation of the fuel cell was not capable of predicting flooding conditions at the stack outlet due to the inherent distribution of the system. In this section, it was shown that by using the appropriate correction factor based on knowledge of the humidity profile in the channel, a one CV model can be augmented to accurately predict flooding conditions and account for diffusion to the anode channel. This leads to a model with superior computation time to a more distributed model that can be used to accurately predict the onset of flooding issues in the end cells.

Chapter V: Individual Membrane Voltage Response and Drive Cycle Experimental Validation

MOTIVATION

The tuning of the voltage parameters presented in Chapter II that was required to obtain experimental agreement has a few implications. Firstly, this is indicative of significant aging effects over the life of the membranes in our system. This implies that a controller and/or lookup tables based on the loss characteristics of unaged membranes may not remain viable over the life of the fuel cell. Aging phenomenon are widely seen, and research regarding the mechanisms and rate of deterioration for proton exchange membranes is ongoing.

One key consideration that has been noted by a number of researchers is that MEAs degrade differently depending on the operating conditions they are subjected to [29, 30]. Studies have shown that the degradation rate is affected by the frequency and duration of open circuit voltage instances [57, 82, 83, 84, 32], low humidity operation [85, 86, 59, 87], high humidity operation [88, 89], and by the operating temperature. In general, degradation tends to become worse with temperatures above 75°C, the use of gases that are not fully humidified, and with load cycling, particularly if the OCV potential is included [30]. Given the inherent variability of the operating conditions both with load variations and depending on the stack location, it is difficult to determine the rate at which individual cells will become unserviceable.

Furthermore, not only will the membrane performance change significantly over the life of the fuel cell, but also that the various cells across the fuel cell stack will age at different rates as they are exposed to different local conditions during operation. Ultimately, this could lead to situations in which the pre-determined operating conditions needed to reach some power or voltage requirement would no longer be valid, and possibly the power output would be unattainable. It is also possible that though a given power could perhaps be reached by the stack, the current selected by a controller based on stack average properties could not be safely sustained by all of the cells in the stack with the chosen inlet conditions. This possibility becomes increasingly likely with high power demands. Operating the stack in this fashion could deteriorate membrane performance prematurely, leading to unexpected maintenance operations and excessive membrane replacement costs.

To combat this, it would be ideal to track the health the membranes in the stack individually. This would aid the control, as set points could be selected to reflect the changes in cell performances. This could also improve maintenance operations, as cells or sections of the stack could be selected for pre-emptive replacement based on limiting criteria of the voltage loss parameters, rather than reacting to cell failures as they arise.

To this end, this chapter covers the development and validation of a state estimation algorithm for a key voltage parameter in the model using an Extended Kalman Filter (EKF). The voltage parameter is treated as a state in the model and is estimated using the EKF. Implementing this with the multi-CV modeling approach makes it possible to investigate the differences in the voltage parameters across the length of the stack. The process is carried out using experimental data in response to load profiles based on standard

US driving cycles to estimate the health of the MEAs in the stack individually. These voltage parameter state estimations will provide a useful addition to the multi-CV modeling approach and also yield quantifiable information regarding membrane aging effects.

STANDARD DRIVE CYCLE TESTS

To test the ability of the model to predict the voltage outputs from individual cells, another set of experiments was performed. To ensure that the tuning method would perform appropriately in realistic scenarios, the load profiles were based on the FTP-75 and HWFET drive cycles. The FTP-75 drive cycle is an American driving cycle that was designed to simulate urban driving and includes frequent stops as well as time at highway speeds [90]. This test was chosen as a rigorous test of the fuel cell and voltage model during an in-city driving situation. The HWFET (Highway fuel economy test) was also selected as it is the standard test used for highway fuel economy estimates [90]. To correlate the velocity profiles to the required power in the fuel cell, the required fuel cell power to accelerate a standard vehicle was calculated then scaled to the stack size of our test station. The required power can be calculated as:

$$P_{stack}(t) = F_{stack}(t) \cdot v(t) \tag{95}$$

where v is the velocity specified by the drive cycle, and F_{stack} is the required force to match the specified speed. This force can be calculated as:

$$F_{stack} = m_{vehicle} a_{DC} + F_{RR} + F_{drag} \tag{96}$$

where a_{DC} is the acceleration calculated from the drive cycle specifications, and F_{RR} and F_{drag} are the rolling resistance and drag forces, respectively, which are estimated as follows:

$$\begin{aligned} F_{RR} &= f_r \cdot m_{vehicle} g \\ F_{drag} &= \tfrac{1}{2} \rho_{air} C_d A_f v^2 \end{aligned} \tag{97}$$

where f_r is the rolling resistance coefficient, C_d is the drag coefficient of the vehicle, and A_f is the frontal area. All of these vehicle parameters were based on a 2015 Toyota Corolla and are listed below:

Table 9: Specifications for the standard vehicle used to represent

PARAMETER	VALUE	REFERENCE
$M_{VEHICLE}$	2800 LBS	[91]
C_D	0.29	[92]
A_F	27.8 FT^2	[91]
F_R	0.012	[93]
ρ_{AIR}	1.225 KG/M^3	AT 15C AND 1 ATM

Finally, the required power was scaled to our test station using the ratio of the effective surface area of the membranes in the Toyota Mirai to the effective surface area of our test membranes. As the active area of the cells in the Mirai was unknown, this value was estimated from the maximum power output of the Mirai (114kW). It was also assumed that the maximum power output of the Mirai was designed to occur with a current density of 800mA/cm2 and cell voltage of ~0.5V, which is a conservative estimate based on the polarization curve published in [69]. As such, the scaling of the required power was as follows:

$$P_{scaled} = P_{stack} \cdot \frac{n_{cells,test} A_{fc,test}}{n_{cells,Mirai} A_{fc,Mirai}}$$
$$A_{fc,Mirai} \approx \frac{P_{max,Mirai}}{0.5V \cdot n_{cells,Mirai} \cdot 800\, mA/cm^2} \quad (98)$$

The speed profiles and scaled experimental power for the FTP-75 and HWFET drive cycles used for the validation experiments are shown in Figure 46 and 47.

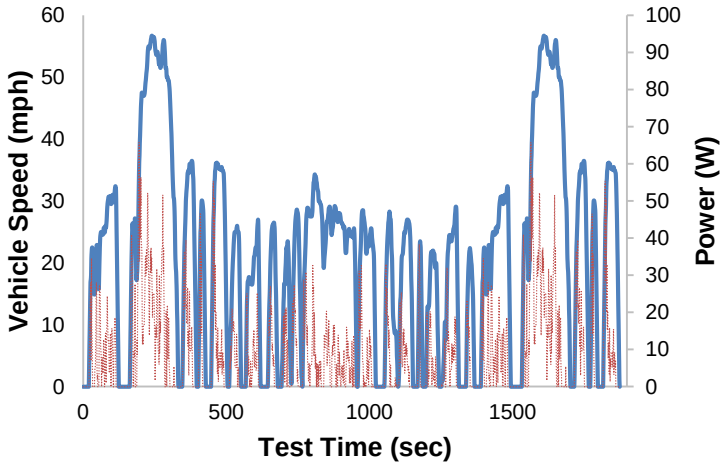

FIGURE 46: FTP-75 SPEED PROFILE (BLUE) AND SCALED POWER (DASHED RED)

Given the limitations of the inputs to the test station, these load profiles were simplified to capture their main features in a manner that could be easily translated to the test station.

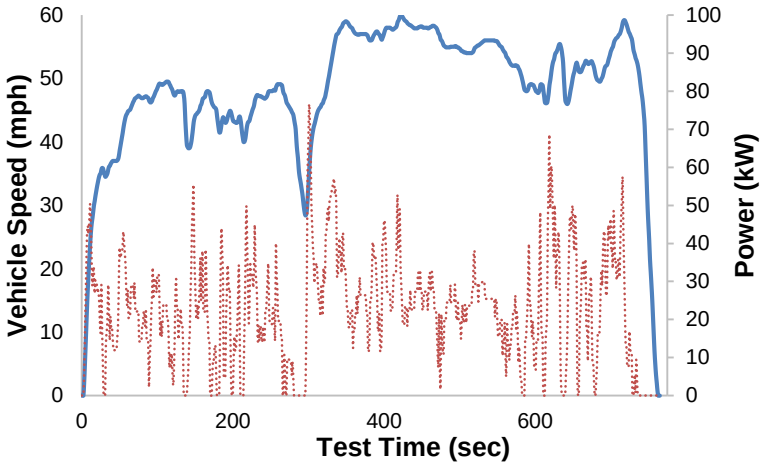

FIGURE 47: HWFET SPEED PROFILE (BLUE) AND SCALED POWER (DASHED RED)

INDIVIDUAL CELL VOLTAGE MODEL TUNING

The results from the FTP-75 drive cycle test were used to validate the tuning of the voltage model. For the experiment, the test conditions shown in Table 10 were used:

Table 10: FTP-75 Test Stack Inlet Conditions

PARAMETER	INPUT RANGE	UNIT
I_{ST}	0-7.75	AMPS
T_{CA}	77.8-80.4	°C
T_{AN}	76.6-79.8	°C
T_{CL}	76.6-80.0	°C
$\dot{V}_{AN}$	2.4-3.5	NLPM
$\dot{V}_{CA}$	13.7-16.4	NLPM
P_{AN}	24.1-79.9	KPAG
P_{CA}	89.0-107.3	KPAG
$T_{DP,CA}$	79.0-79.2	°C
$T_{DP,AN}$	76.7-80.8	°C

The following figure compares the experimental and modeled voltage response to the scaled FTP-75 load profile using membrane state variables based on a new membrane.

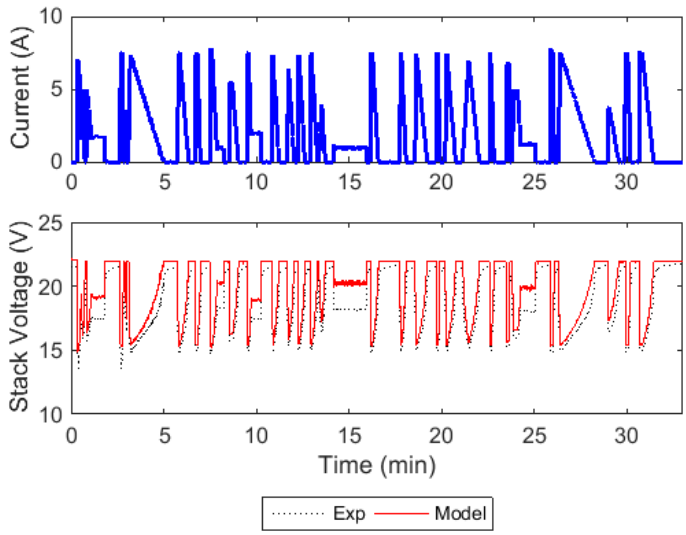

FIGURE 48: FTP-75 STACK VOLTAGE RESPONSE NO TUNING

As shown in Figure 48, using the original membrane state values, the model overpredicted the stack voltage output for the entire experiment. This is particularly evident during the sections of the test with a constant load. Furthermore, the correlation of the model to the response of individual cells differed greatly from cell to cell.

Figure 49 and 50 show the modeled and measured responses from the worst (Cell 8) and one of the best performing (Cell 2) cells from this set of tests. It can be seen that though the original membrane state parameters lead to a reasonable prediction of the output from Cell 2, it lead to a gross overprediction of the output from Cell 8 throughout the entire test cycle. This suggests a drastic difference in the health of the cells and shows the need for a method to individually tune the membrane state parameters to compensate for the different degradation rates experienced throughout the stack.

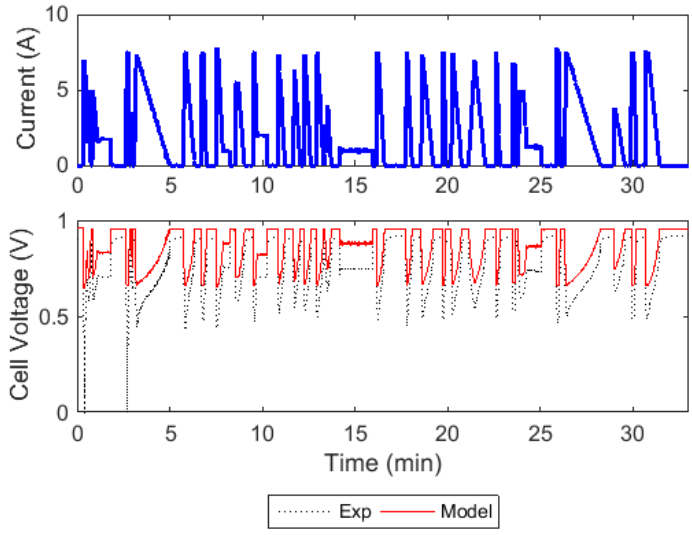

FIGURE 49: FTP-75 CELL #8 VOLTAGE RESPONSE NO TUNING

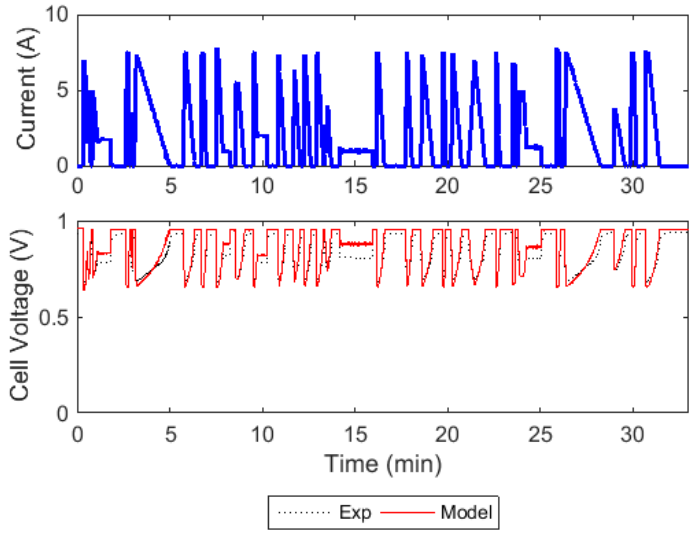

FIGURE 50: FTP-75 CELL #2 VOLTAGE RESPONSE NO TUNING

Though a general parameter tuning technique was used previously to correct the errors in the voltage model, the results had a few limitations. Firstly, the technique was based on the overall stack voltage response. As such, the results could not be used to account for differences in the state of health of individual cells. Secondly, the variables

that were previously selected for tuning do not lead to any physical understanding of the degradation. While c1 and the gain on the ohmic resistance were effective for tuning the model for the work presented in Chapter II, interpreting the significance of the new values was difficult given the empirical nature of the variables that were chosen. As a result, it would be difficult to define any kind of criteria for the limits of these variables for maintenance scheduling.

Thirdly, the previous results were only applicable to the stack at the time that the experiments used for tuning were performed. As the membranes continue to age, these parameters would not represent the further changes in the membrane health. The following figures show the voltage response of the stack as well as Cells 2 and 8 using the tuning results from the previous experiments.

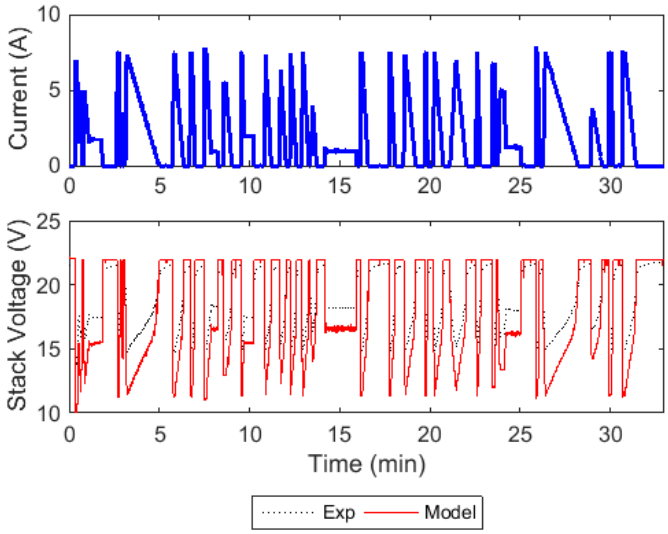

FIGURE 51: FTP-75 STACK VOLTAGE RESPONSE C1=76 & K_{OHM}=3.35

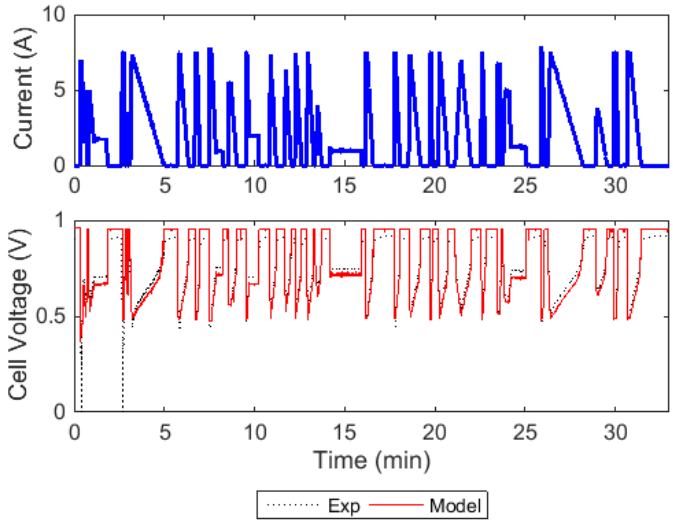

FIGURE 52: FTP-75 CELL #8 VOLTAGE RESPONSE C1=76 & K_{OHM}=3.35

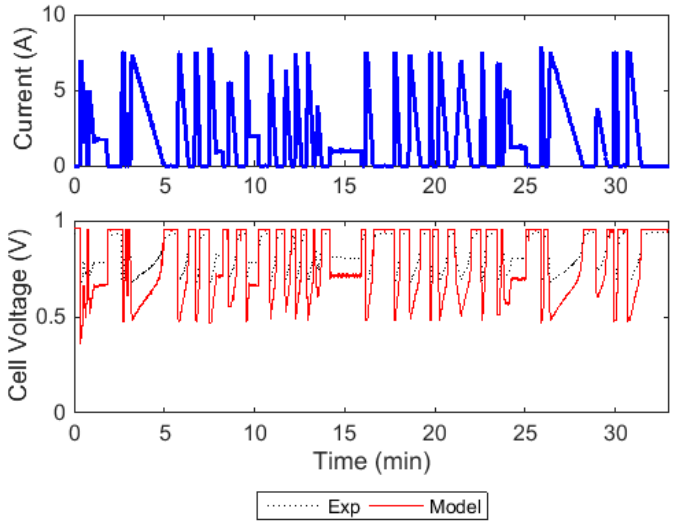

FIGURE 53: FTP-75 CELL #2 VOLTAGE RESPONSE C1=76 & K_{OHM}=3.35

Figure 51, 52, and 53 clearly show the shortcomings of the previous tuning method. Using these variables led to a significant underprediction of the stack voltage. Also, while this did yield a reasonable result for Cell 8, it also led to a severe underprediction of the output from Cell 2. This result again highlights the need for individual treatment of the

membrane state parameters, preferably based on physically relevant metrics. This would lead to a much better understanding of the actual membrane health, which clearly declined differently for each cell.

Extended Kalman Filter for Fuel Cell Membrane Parameters

First, it should be mentioned that not every state in the model was estimated with the EKF. For this investigation, the estimated states were limited to voltage parameters for the membranes and did not include the operating condition states (e.g. species masses, system temperature, etc.). This approach was selected for a number of reasons. Firstly, this limited the additional computational expense that would be necessary to estimate the 22 dynamic states in the distributed system model. Secondly, in the event that these states were in fact estimated, the observability of all the internal operating conditions, such as the species concentrations in the channels, would be extremely low with respect to the available measurements. As such, rather than estimating the internal states statistically, the distributed model was used to determine these states for use in the voltage parameter estimation process.

This brings the attention to which voltage parameters should be estimated. The decline in the effective membrane surface area (EMSA) as a result of agglomeration and platinum dissolution in the catalyst layer has been cited by number of studies [94, 95, 96], and is often considered to be the major contributor to the loss of performance in fuel cell stacks. The EMSA also gives a clear, physical definition of the state of health of the membrane, and a simple lower limit on could be defined to determine when a membrane

needed to be replaced (e.g. 50% of the original value). Looking at the voltage output equations presented in Chapter II, you can see that the EMSA affects all of the overpotential losses in the membrane as all of the overpotential losses are functions of the current density. These criteria make the EMSA a good candidate for state estimation as it has clear physical meaning and significantly affects the voltage output, which makes it easily observable with respect to the measurements.

General Extended Kalman Filtering Algorithm

Given the nonlinearity of the voltage equations for PEM fuel cells, an EKF was used to estimate the EMSA. The general EKF algorithm can be described by two major processes, a state propagation in time followed by a state update based on the measurements. The state propagation process is used to determine how the state alters between measurements using rate equations based on the current state of the system and any necessary inputs. Subsequently, the measurement update process provides the optimal estimate of the state in question based on a related system measurement and the value of the propagated state. This process has the following general form:

State Equations:

$$\dot{x} = f\left(x(t), u(t)\right) + G(t)w(t) \tag{99}$$

Measurements:

$$z(t) = h\left(x(t)\right) + v(t) \tag{100}$$

State Propagation Process:

$$\begin{aligned} x\left(t_{i+1}^{-}\right) &= x\left(t_i\right) + \dot{x}\left(t_i\right)\Delta t \\ P\left(t_{i+1}^{-}\right) &= P\left(t_i\right) + \dot{P}\left(t_i\right)\Delta t \end{aligned} \tag{101}$$

where the (-) designates the time immediately before the measurement, Δt is the amount of time between measurements, and P is the state covariance matrix whose rate of change is calculated as:

$$\begin{aligned} \dot{P}\left(t_i\right) &= F\left(x\left(t_i\right)\right)P\left(t_i\right) + P\left(t_i\right)F^T\left(t_i\right) + G\left(t_i\right)Q\left(t_i\right)G^T\left(t_i\right) \\ F\left(t_i\right) &= \frac{\delta f\left(x\left(t_i\right), u\left(t_i\right)\right)}{\delta x} \end{aligned} \tag{102}$$

where Q is the strength of the zero-mean white Gaussian process represented by *w* and matrix G.

Measurement Update:

$$\begin{aligned} x\left(t_i^{+}\right) &= x\left(t_i^{-}\right) + K\left(t_i\right)\left\{z_i - h\left[x\left(t_i\right)\right]\right\} \\ P\left(t_i^{+}\right) &= P\left(t_i^{-}\right) - K\left(t_i\right)H\left[x\left(t_i\right)\right]P\left(t_i^{-}\right) \end{aligned} \tag{103}$$

where the (+) designates the time immediately after the measurement, and K is the Kalman gain defined as:

$$K\left(t_i\right) = P\left(t_i^{-}\right)H^T\left[x\left(t_i^{-}\right)\right]\left\{H\left[x\left(t_i^{-}\right)\right]P\left(t_i^{-}\right)H^T\left[x\left(t_i^{-}\right)\right] + R\left(t_i\right)\right\}^{-1} \tag{104}$$

where H is a partial derivative matrix defined as:

$$H\left[x\left(t_i^{-}\right)\right] = \frac{\delta h\left(x\left(t_i\right)\right)}{\delta x} \tag{105}$$

In Eqn. (104), R is the strength of the white Gaussian process associated with the system measurements (i.e. measurement error or variance).

Extended Kalman Filtering Algorithm for Membrane State Estimates

It is assumed that the health of the membrane changes slowly relative to the time between measurements. Therefore, any membrane state that is investigated for estimation can be considered to be constant for state propagation processes spanning reasonably short durations. This fact in addition to the lack of models for the rate of degradation for specific membrane parameters effectively eliminates the state propagation step. However, to effectively account for the fact that the system parameters are known to slowly decline, the covariance needs to propagate in time between measurements to account for the increasing uncertainty in the value of the parameters between measurements. The resulting system equations for the case in which only the EMSA is estimated is as follows:

State Equations:

$$x = \begin{bmatrix} A_{fc,1} \\ \vdots \\ A_{fc,n} \end{bmatrix}$$

$$\dot{x} \approx [0] + w$$

$$\dot{P} = Q \tag{106}$$

It should be noted that since the rate of change of the states is essentially zero, matrix F in Eqn. (102) is also zero. The strength of the white noise variance of the states was estimated from previous degradation studies of PEM membrane assemblies. A number of studies have investigated this issue [97, 30], but often report degradation in terms of a voltage loss rate due to the number of possible contributors to this decay, rather than directly citing the decline of individual membrane parameters. To estimate the process noise strength, the value given by [30] for a membrane operated at 75°C and near 100%

humidity was used. They suggested that a 10% decline in voltage over 40,000 h was possible. As a conservative estimate of the process noise of the effective surface area, this was assumed to relate to two standard deviations in the EMSA as follows:

$$Q \approx \frac{\left(A_{fc,o} \cdot 0.1/2\right)^2}{40000 \cdot 60 \cdot 60} \tag{107}$$

This ensures that the covariance would propagate in such a way that after 40,000 hours, two standard deviations of the EMSA would encompass a 10% decline from the initial value.

Measurements:

$$z = \begin{bmatrix} V_{cell,1} & \cdots & V_{cell,n} \end{bmatrix} \tag{108}$$

The measurement update process proceeds according to Eqn. (103). The H matrix is defined by the model of the connection between the measurement and the states. In this case, the measurements are the individual cell voltages. The cell voltage modeled as:

$$\begin{aligned} V_{cell} &= V_{ideal}\left(P_{H_2}, P_{O_2}, T_{FC}\right) - V_{act} - V_{ohm} - V_{conc} \\ &= V_{ideal} - \left[V_0 + V_a\left(1 - e^{-c_1 \cdot \frac{I_{st}}{A_{fc}}}\right) + \frac{I_{st} \cdot t_m}{A_{fc}\left(b_{11}\lambda_m - b_{12}\right) exp\left(b_2\left(\frac{1}{303} - \frac{1}{T_{fc}}\right)\right)} + \frac{I_{st}}{A_{fc}}\left(c_2 \frac{I_{st}/A_{fc}}{i_{max}}\right)^{c_3} \right] \end{aligned} \tag{109}$$

Subsequently, for the case of tuning the EMSA, the H matrix is defined by differentiating Eqn. (109) with respect to the membrane states for each cell

$$H = \begin{bmatrix} H_{A_{fc,1}} & 0 & 0 \\ 0 & \ddots & 0 \\ 0 & 0 & H_{A_{fc,n}} \end{bmatrix} \tag{110}$$

where $H_{A_{fc,n}}$ is defined as:

$$H_{A_{fc,n}} = \frac{V_{a,n} I_{st} c_1 e^{-I_{st}c_1 / A_{fc,n}}}{A_{fc,n}^2} + \frac{I_{st} R_{ohm,n}}{A_{fc,n}^2} + \frac{I_{st}\left(\frac{I_{st}c_2}{A_{fc,n} i_{max}}\right)^{c_3}}{A_{fc,n}^2} - \frac{c_3 c_2 \left(\frac{I_{st}c_2}{A_{fc} i_{max}}\right)^{c_3 - 1}}{A_{fc,n}^3 i_{max}} \tag{111}$$

To complete the implementation, the initial conditions for the membrane states and covariance matrix needed to be defined. The initial membrane state for each cell was taken to be the nominal value for new membranes (27.85cm^2). For the covariance matrix, it was assumed that there were no cross-covariance relationships in this system (i.e. the EMSA of one cell does not affect that of another), so the matrix was diagonal, and all the off diagonal terms were set to 0. While it seems likely that the state of one membrane in the stack would not affect the state in another, it is unclear whether there is any relationship between the individual states in a given membrane (e.g. does the EMSA in a membrane inherently alter the electrical conductivity). Further understanding of the connection between the individual membrane states in the stack is of great interest and will be studied in the future.

For the diagonal terms, the initial covariance value should equal the square of the standard deviation for each state based on the initial guess for the uncertainty in the nominal values. The selection of the initial covariance is important as it ultimately determines the size of the initial step in the measurement update. In this case, it was known that the membranes had degraded significantly. Therefore, to allow for faster convergence of the EMSA from the initial value, the initial standard deviation was assumed to be 5% of the

nominal value for the EMSA after a trial-and-error study of the EKF stability with different initial standard deviations. The distributed model was incorporated by individually assigning the inputs for the voltage model (partial pressures, membrane water contents, etc.) based on their location in the CVs. Cells that were located entirely within a given CV were assigned the values calculated for that CV. Conversely, for cells that spanned multiple CVs, the assigned values were equal to an average between the two CVs weighted by the volume occupied by the cell in each CV.

Modification of the EKF for Additional Membrane State Estimates

To quickly test additional membrane parameters, the EKF would only need to be slightly adjusted. All of the states are assumed to be basically invariant over short time steps, which eliminates the state propagation step, and all cross-covariances are assumed to be 0, which makes it possible to handle the covariance propagations individually. As such only the EKF structure and H matrix need to be updated to include additional states. For instance, in the case that an ohmic loss gain wanted to be tuned in addition to the EMSA in keeping with the tuning method from Chapter II, the state equations would then become:

$$x = \begin{bmatrix} A_{fc,1} \\ \cdots \\ A_{fc,n} \\ K_{ohm,1} \\ \cdots \\ K_{ohm,n} \end{bmatrix} + w$$

$$\dot{x} \approx [0]$$

$$\dot{P} = Q \tag{112}$$

The H matrix would also need to be expanded to include terms for the new membrane state to be estimated:

$$H = \begin{bmatrix} H_{A_{fc,1}} & 0 & 0 & \dots & \dots & 0 \\ 0 & \ddots & 0 & \dots & \dots & \vdots \\ 0 & 0 & H_{A_{fc,n}} & \dots & \dots & \vdots \\ \vdots & \vdots & \vdots & H_{K_{ohm,1}} & \dots & \vdots \\ \vdots & \vdots & \vdots & \vdots & \ddots & \vdots \\ 0 & \dots & \dots & \dots & \dots & H_{K_{ohm,n}} \end{bmatrix} \tag{113}$$

To generalize the operation and make it relatively simple to test other state estimation schemes, the H matrix can also be calculated numerically using the complex-step derivative approximation method. This approximation method takes the following form [98]:

$$\frac{\delta f}{\delta x} \approx \frac{\mathrm{Im}\left[f\left(x + ih\right)\right]}{h} \tag{114}$$

where h is a small perturbation value. As this is a numerical differentiation method, there is no need to explicitly calculate the derivatives, which can be tedious in some cases or if various variables are to be investigated. Furthermore, as there are no difference operations, this method does not have any subtractive cancellation errors, which leads to advantages over typical finite difference approaches in terms of accuracy and computation time [98, 99]. This method was confirmed by comparing the results using the analytical derivative to the complex-step derivative and was implemented to estimate additional membrane states of interest (i.e. K_{ohm}, b_{11}, b_{12}, and b_2). For the case of estimates for both the EMSA and K_{ohm}, the diagonal terms for the H matrix would be calculated as:

$$H_{A_{fc,n}} = \frac{\mathrm{Im}\left[V_{cell,n}\left(u, A_{fc,n} + ih, K_{ohm,n}\right)\right]}{h}$$
$$H_{K_{ohm,n}} = \frac{\mathrm{Im}\left[V_{cell,n}\left(u, A_{fc,n}, K_{ohm,n} + ih\right)\right]}{h} \quad (115)$$

For the implementation in MATLAB/Simulink, h was taken to be 2.2204×10^{-16}, which is the smallest increment recognized in MATLAB. In Eqn. (115) *u* is comprised of the modeled states required to calculate the voltage output, namely the hydrogen and oxygen partial pressures, membrane water content, fuel cell temperature, cathode total pressure, and stack current. Ultimately it was determined that the EMSA alone lead to the best membrane health estimations given the limitations with regards to the load dynamics, as will be discussed later. However, this modeling technique could be useful for estimating more membrane parameters for potential future work.

HWFET EKF Tuning Results

The experiment using the approximation of the HWFET load profile was used to tune the EMSA for each cell using the EKF method described previously. This test was used as it was a less volatile profile than the FTP-75 approximation and contained more sections of steady current demand. The following figure shows the measured and modeled stack voltage response during the HWFET test as the EKF process is actively tuning the EMSA for each cell. The initial estimate for the EMSA for all the cells was the value that corresponds to a new membrane (27.85cm^2).

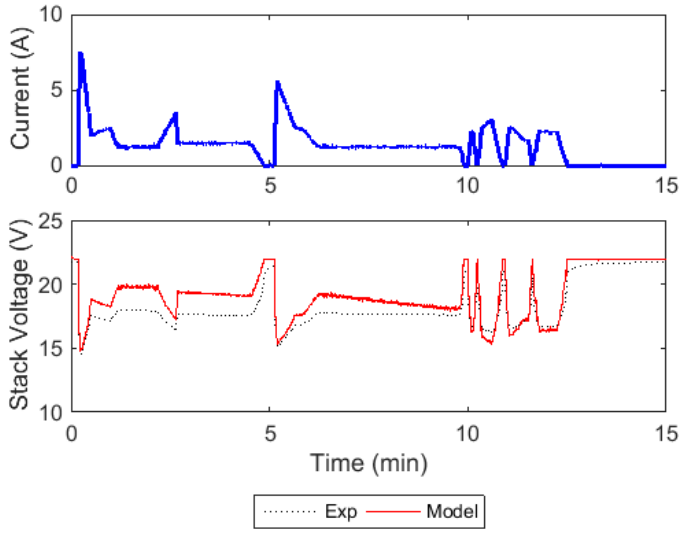

FIGURE 54: HWFET VOLTAGE RESPONSE DURING THE EKF TUNING PROCESS

Initially, the model overpredicted the output of the stack as was seen with the FTP-75 modeling results. However, as the EKF process continued, the agreement with the model slowly improved, and from approximately 10 minutes into the test onward the model closely matched the measured response. Also, using the EKF method on each cell allows for good agreement on a cell-by-cell basis as shown in Figure 55 and Figure 56. These figures show the measured and modeled voltage response from Cells 2 and 8 as the EKF tunes the EMSA starting from the new membrane value. Again, it can be seen that though there is initially a significant difference between the model and measurements, by the end of the test cycle, the agreement becomes very good for both cells by individually tuning the EMSA. This individualized information could be used to more properly inform controllers for online decision making.

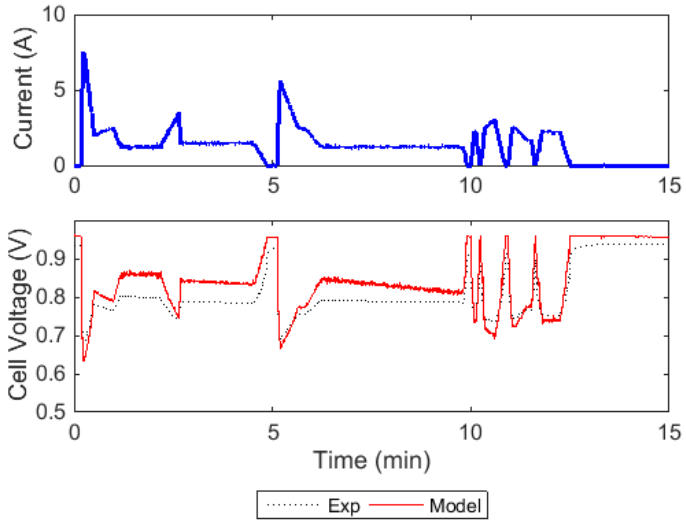

Figure 55: HWFET Voltage Response During EKF Tuning Cell #2

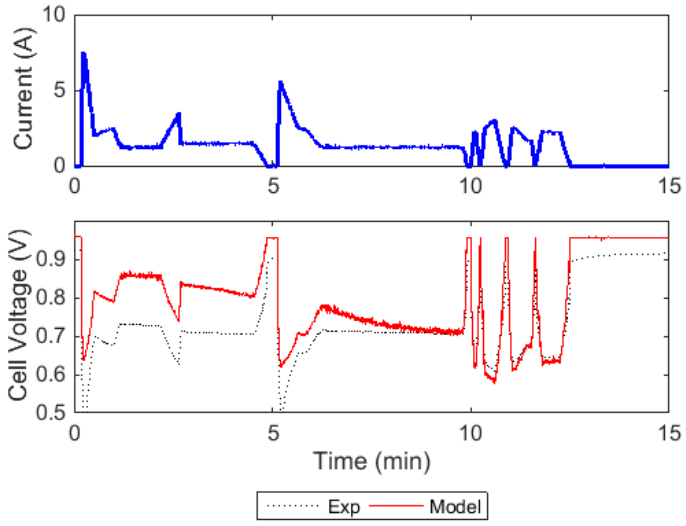

FIGURE 56: HWFET VOLTAGE RESPONSE DURING EKF TUNING CELL #8

Finally, the estimated EMSA seems to converge to a steady value for each cell. Figure 57 shows the changes in the EMSA made by the EKF algorithm over the course of the test for all 23 cells. As you can see, the estimated EMSA begins at the same initial value for all the cells, but over the course of the test, the EKF predicts varying degrees of

membrane health for each cell and Cell 8 as the least healthy membrane. This result will be discussed further later in this chapter.

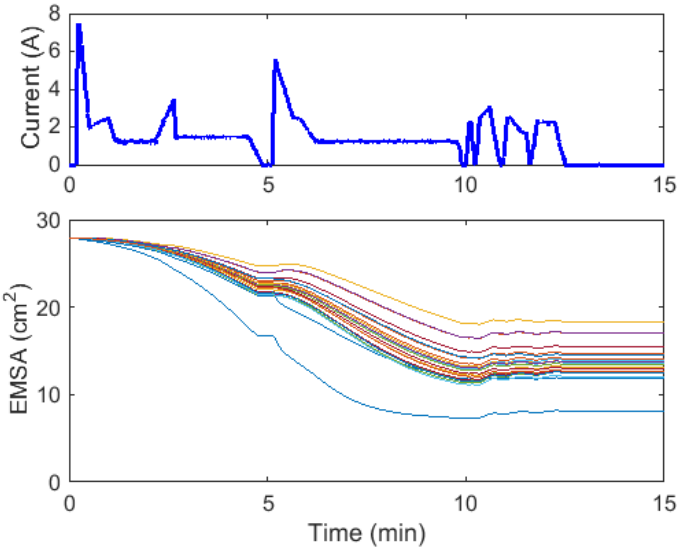

FIGURE 57: EMSA EKF TUNING DURING HWFET TEST CYCLE

FTP-75 EKF Tuning Validation

In general, changes to the membrane states are expected to occur slowly. Therefore, one would expect that the results of the EMSA estimation from the HWFET test would be applicable to the FTP-75 test as well because the two tests were run in quick succession. The following figures show the measured and modeled voltage outputs during the FTP-75 test with the EMSA for each cell fixed at the final estimates from the EKF tuning with the HWFET results.

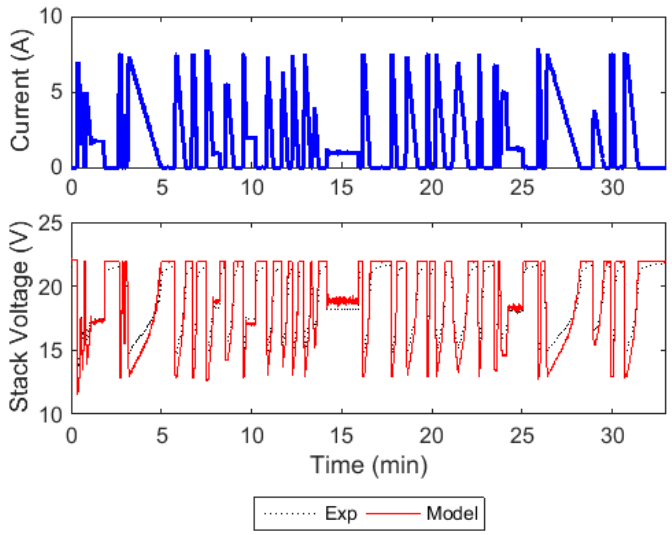

FIGURE 58: FTP-75 STACK VOLTAGE RESPONSE AFTER HWFET EKF TUNING

It can be seen that the overall agreement of the model is better than it was before tuning (Figure 48) and much better than when using the tuning parameters determined from previous tests (Figure 51). Using the EKF tuning method, the average RMS error for the stack voltage prediction reduced from 0.917V over the course of the test to 0.819V. More importantly however, the standard deviation of the RMS error for the individual cells decreased using the EKF tuning method. This shows the usefulness of the EKF in limiting the error of the voltage model for every cell in the stack. Table 11 provides a complete list of the error in the voltage model using the membrane parameters associated with new MEAs, the tuning parameters previously used in Chapter II to tune the voltage model, and with the EMSA adjustment predicted by the EKF during the HWFET test cycle. Though there are a few cells for which the EKF tuning slightly increased the RMS error, it is clear that on the whole the voltage response was improved, particularly for the cells that displayed the poorest performance (highlighted in Table 11). Also, it should be noted that

the maximum difference between the measured and modeled voltage decreased for all the cells using the EKF estimates of the EMSAs.

Table 11: Voltage Model Error Using Different Tuning Methods

	No Tuning			C1=76 & Kohm=3.35			EMSA EKF Tuning		
Cell #	RMS	Error	Max Absolute	RMS	Error	Max Absolute	RMS	Error	Max Absolute
Stack	0.917	-0.906	---	1.501	0.956	---	0.819	0.081	---
1	0.058	-0.058	0.906	0.045	0.025	0.252	0.021	-0.006	0.175
2	0.032	-0.025	0.262	0.084	0.058	0.342	0.040	0.005	0.185
3	0.023	-0.013	0.254	0.081	0.070	0.342	0.031	0.012	0.162
4	0.026	-0.018	0.265	0.079	0.065	0.343	0.034	0.011	0.158
5	0.046	-0.046	0.307	0.069	0.036	0.287	0.044	0.002	0.177
6	0.036	-0.036	0.294	0.068	0.046	0.305	0.037	0.005	0.167
7	0.030	-0.029	0.280	0.074	0.054	0.327	0.036	0.007	0.167
8	0.092	-0.092	0.734	0.039	-0.009	0.215	0.043	-0.011	0.242
9	0.031	-0.031	0.285	0.070	0.051	0.309	0.034	0.007	0.168
10	0.042	-0.042	0.286	0.070	0.039	0.290	0.041	0.002	0.170
11	0.043	-0.043	0.300	0.064	0.038	0.289	0.039	0.003	0.183
12	0.042	-0.042	0.303	0.065	0.039	0.292	0.039	0.004	0.181
13	0.038	-0.037	0.282	0.068	0.043	0.285	0.037	0.004	0.160
14	0.047	-0.047	0.306	0.064	0.034	0.277	0.039	-0.001	0.171
15	0.043	-0.043	0.301	0.063	0.037	0.274	0.038	0.003	0.170
16	0.035	-0.035	0.269	0.070	0.045	0.294	0.038	0.004	0.162
17	0.033	-0.032	0.262	0.065	0.047	0.273	0.033	0.009	0.163
18	0.039	-0.039	0.281	0.067	0.041	0.278	0.036	0.002	0.156
19	0.039	-0.039	0.269	0.065	0.041	0.272	0.036	0.003	0.160
20	0.048	-0.048	0.301	0.063	0.032	0.266	0.040	0.000	0.221
21	0.038	-0.038	0.278	0.060	0.041	0.259	0.033	0.006	0.152
22	0.029	-0.027	0.260	0.063	0.052	0.286	0.028	0.011	0.225
23	0.043	-0.043	0.269	0.065	0.035	0.260	0.038	0.002	0.159

EKF State Estimation Discussion and Aging Differences Between Cells

The FTP-75 modeling results suggest that the tuning method could be improved to increase the confidence in the membrane state estimates, as will be discussed here. It should be noted that the largest differences in the measured and modeled voltages after tuning the EMSA occur after sudden changes in the applied load, both with sharp increases in the load and when the load is swiftly removed. This could be due to a number of reasons. Firstly, given the number of possible membrane degradation mechanisms, it is possible that more membrane properties need to be estimated to fully capture the changes to the voltage output of the stack. For instance, the membrane thickness and other ohmic resistance

properties have been shown to change over time as well, and could affect the voltage response significantly. It is also possible that there are un-modeled voltage dynamics that are significant with fast dynamic load changes. This possibility will be discussed further below.

Regardless, as a result of the dynamic differences in the voltage responses, the state estimates from the EKF process in this scenario are affected by the dynamics of the applied load. This fact is highlighted by Figure 59, which shows the response of the state estimations with the EKF enabled during the FTP-75 test cycle. The initial state and covariance estimates were set to the final values from the EKF process during the HWFET test cycle for the state estimation process.

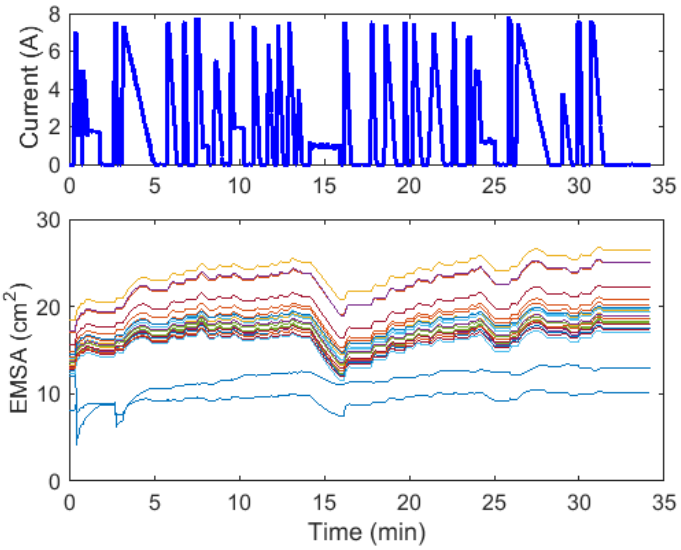

FIGURE 59: EMSA EKF TUNING DURING FTP-75 TEST CYCLE

Firstly, it can be seen that the prediction of the predicted relative state of health is consistent for both tests despite the significantly different load dynamics. In all cases, Cell 8 is found to be the least healthy membrane, and the ranking of the EMSA for each cell

remains the same besides. This suggests that the EKF method does give a good indication of the state of health. However, it can be seen that the EMSA state estimations tend to increase in response to swift load variations. When the load is held constant, the estimations decline and seem to approach the values estimated by the EKF during the HWFET process. This is likely due either to voltage dynamics that are not captured by the model or a lag in the voltage measurements from the test station. The EKF can be implemented continuously to maintain the accuracy of the voltage model, but the estimation of the state parameters themselves is contingent upon the fidelity of the model.

Though previous studies stated that the time constant for voltage variations is extremely short for a single cell [53], if these effects are in fact important in fuel cell stacks or become more significant as membranes age, the resulting discrepancy would reduce the accuracy of the estimated state value. The experimental results showed a slow rise of the voltage from the value while loaded to the OCV when the load was quickly removed, as shown in Figure 60.

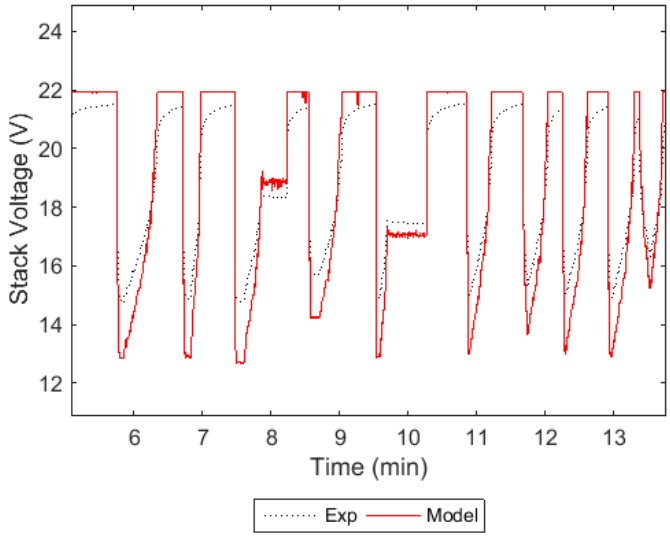

FIGURE 60: VOLTAGE DYNAMICS DURING FAST LOAD CHANGES IN THE FTP-75 TEST

This suggests that double layer capacitance (DLC) dynamics are in fact significant in this stack and that adding consideration of this to the model could improve the stability of the state estimations. Double layer capacitance effects essentially cause the activation and concentration overpotential losses to lag in response to swift load variations [53]. As a result, in reality the voltage response does not decline as swiftly as would be predicted by the model, which assumes that all the overpotential losses react instantaneously. This would explain the response of the state estimates to swift load dynamics as the modeled voltage would consistently be lower than the measurements during fast dynamics if DLC effects are in fact significant. This would cause the EKF to increase the EMSA state estimates to compensate for the low voltage prediction from the model. Though the addition of a DLC model could limit these issues, this would require an additional state with a small time constant for each cell in the stack, and is perhaps not a practically feasible option for real-time calculations on a large stack.

Regardless, the EKF estimations provide useful information on the health of membranes in the stack. Figure 61 shows the final estimated EMSA values for each cell in the stack during the HWFET and FTP-75 test cycles. In these plots, cells 1 and 23 correspond to the outlet and inlet of the stack, respectively.

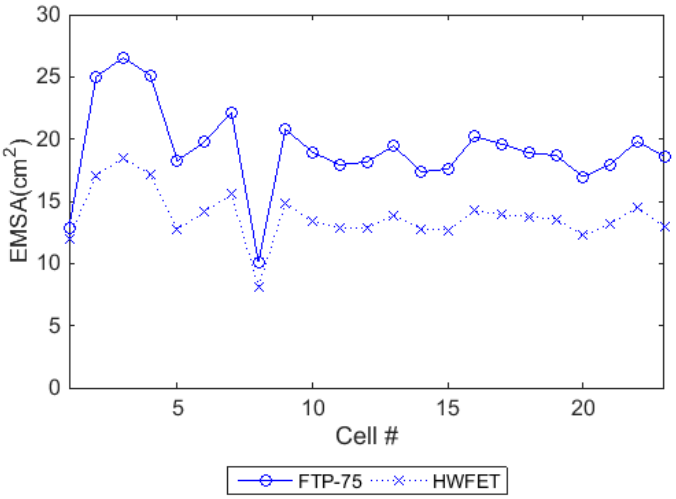

FIGURE 61: FINAL EMSA ESTIMATIONS FROM THE HWFET AND FTP-75 TESTS

As you can see, the trends in the estimated EMSA remained the same during both test cycles, despite the variations in the absolute value of the estimation, possibly due to the lack of DLC effects in the model as previously discussed. This suggests that the method does reveal information about the membrane health and performance as the relative estimations are consistent over a wide range of variations in the load and conditions. A rolling average of the EMSA estimation for each cell could be used to track long term membrane health degradation as well as to inform prognostics models to schedule preemptive maintenance operations. Implementing a low pass filter on the residual as suggested by Zhang et al. [65] could also be an effective method to limit the effect of fast

dynamics on the estimations. Care would have to be taken to tune the filter appropriately such that key dynamics are not lost. Furthermore, this issue would have to be addressed before the EKF could be used to estimate additional membrane parameters reliably.

It should also be noted that the value of the estimated EMSA was fairly consistent for both Cell 1 and Cell 8, which were the lowest performing cells in the stack. Therefore, it seems as if this method is effective in identifying particularly low performing membranes that are in need of replacement, regardless of the load dynamics.

Lastly, Figure 61 shows that there may be some correlation between the stack location and membrane health. Excluding Cell 1 and Cell 8, there is a general trend of increasing health going from the inlet (Cell 23) to the outlet (Cell 1). This could be due to the fact that the OCV decreases slightly along the length of the stack due to the drop in pressure associated with the flow of reactants through the channels. A number of studies have shown that Pt particle agglomeration and dissolution mechanisms are enhanced by high electrochemical potentials and load cycling [96, 88, 100, 101]. The slightly lower OCVs and decreased ohmic resistance typical in the latter cells would reduce the magnitude of the changes in cell voltage and may have contributed to limiting the EMSA loss. Though high humidities have also been shown to enhance particle growth [88, 89], this effect was most likely mitigated by the fact that many of the experiments run with these MEAs were performed with a low inlet RH to avoid flooding the membranes and RH sensors at the stack outlet. However, more investigation would be necessary to determine the consistency of this trend.

Ex-Situ Membrane Health Verification

To test the validity of the estimations made by the EKF algorithm, Cells 1, 2, and 8 were removed from the stack for further investigation by XRD and SEM analyses. These membranes were selected as they represented two poorly performing cells, and one of the high performing cells in the stack. XRD analysis was performed first, but no clear difference could be seen between the cells with this measurement technique. Subsequently, SEM analysis was performed to investigate the catalyst layers more closely. Samples from each MEA were taken from their center where they were in direct contact with the reactant gases while in operation. In preparing the samples, the Nafion membrane was removed so that the catalyst layer could be observed directly. It should also be noted that though the anode and cathode catalyst layers were scanned independently, no significant differences between the electrodes were noted within the same MEA. The following figure shows a representative image of the catalyst layers from Cell 8.

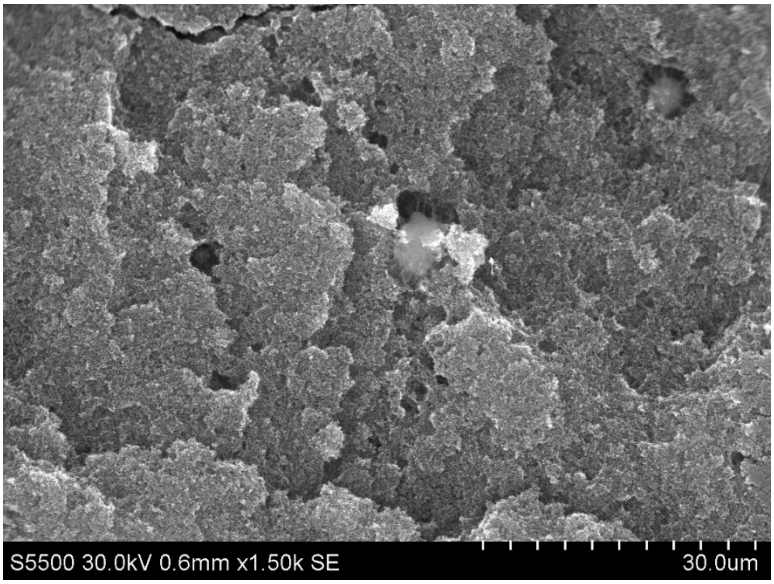

FIGURE 62: CELL 8 ANODE CATALYST OVERVIEW 1.50K MAGNIFICATION

Figure 62 shows the first signs of the source of poor performance in Cell 8. There were clear signs of pitting throughout the catalyst, which were perhaps the beginnings of membrane hotspot formations. Similar formations were noted in Cell 1 as shown in Figure 63, but these formations were not seen in the MEA from Cell 2.

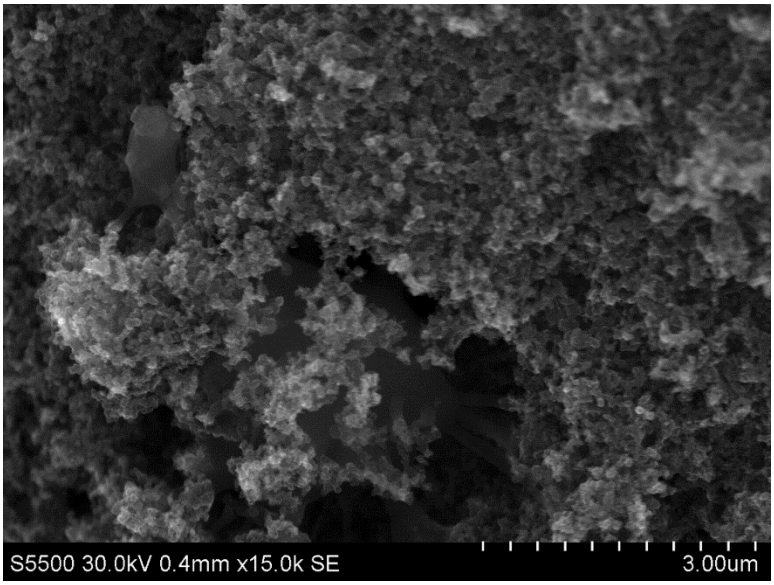

FIGURE 63: CELL 1 ANODE CATALYST PITTING 15.0K MAGNIFICATION

Though these pitting formations suggest degradation beyond just the EMSA of Cells 1 and 8, there were also indications of significant EMSA loss for these cells as well.

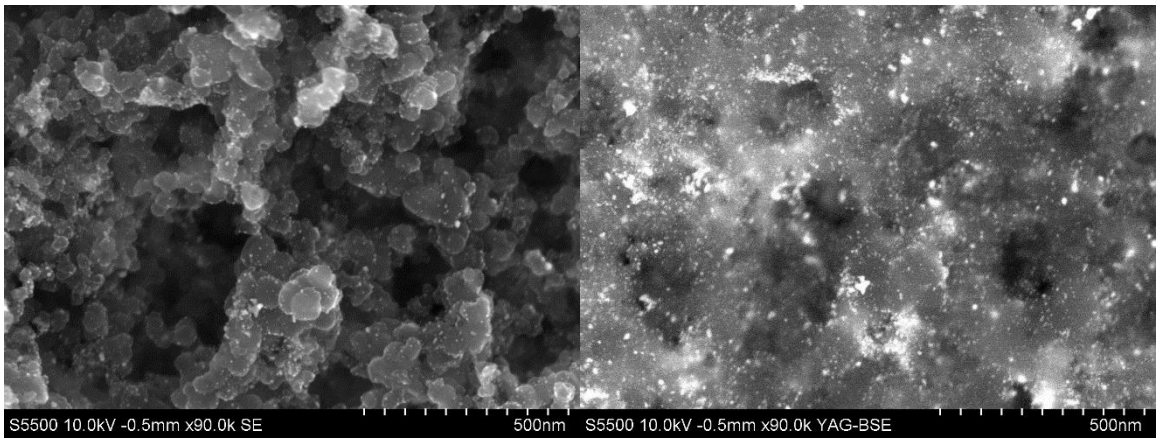

FIGURE 64: CELL 1 SE AND BSE IMAGE COMPARISON 90K MAGNIFICATION

The following figures show 90k magnification images of Cells 1 and 8 with their corresponding backscattered emission (BSE) images.

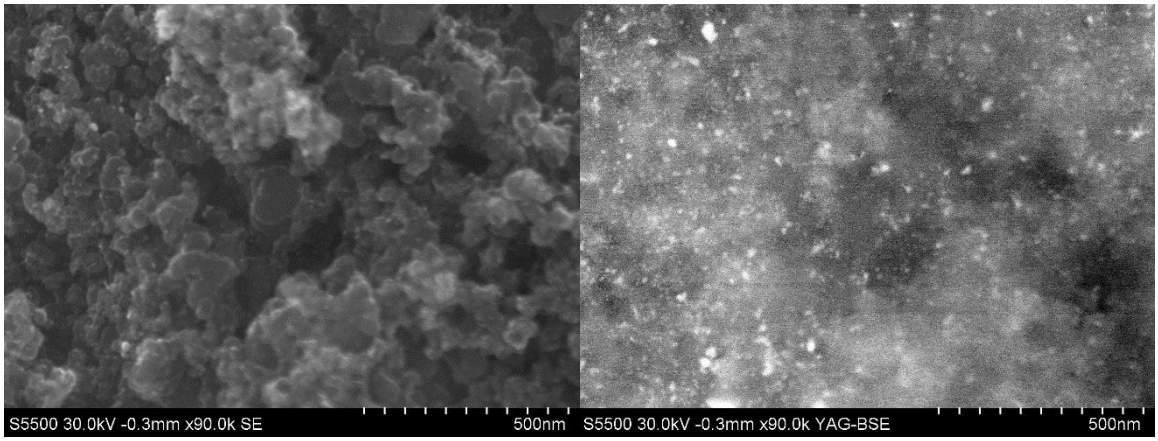

FIGURE 65: CELL 2 SE AND BSE IMAGE COMPARISON 90K MAGNIFICATION

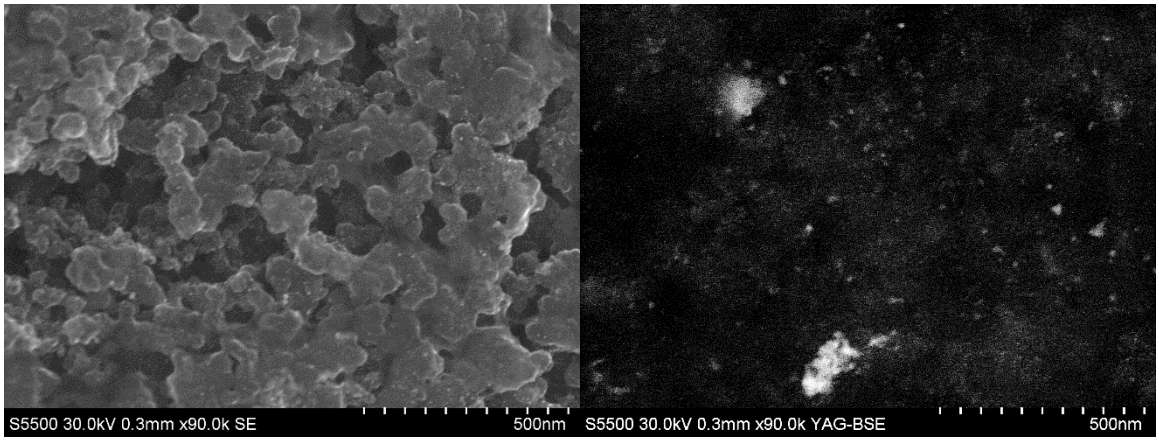

FIGURE 66: CELL 8 SE AND BSE IMAGE COMPARISON 90K MAGNIFICATION

Figures 64, 65, and 66 show a good indication of the relative aging patterns for Cells 1, 2, and 8, respectively. As it can be seen, Cells 1 and 8 formed a number of areas with very large agglomerations. While Cell 2 also did have a few larger particles, the severity and frequency of the agglomerations in Cells 1 and 8 seemed to be much higher.

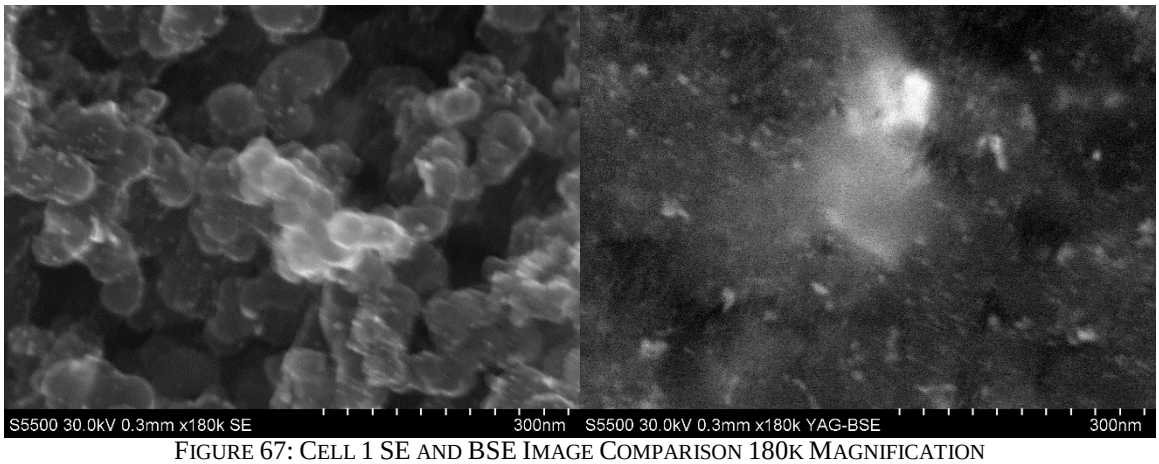

FIGURE 67: CELL 1 SE AND BSE IMAGE COMPARISON 180K MAGNIFICATION

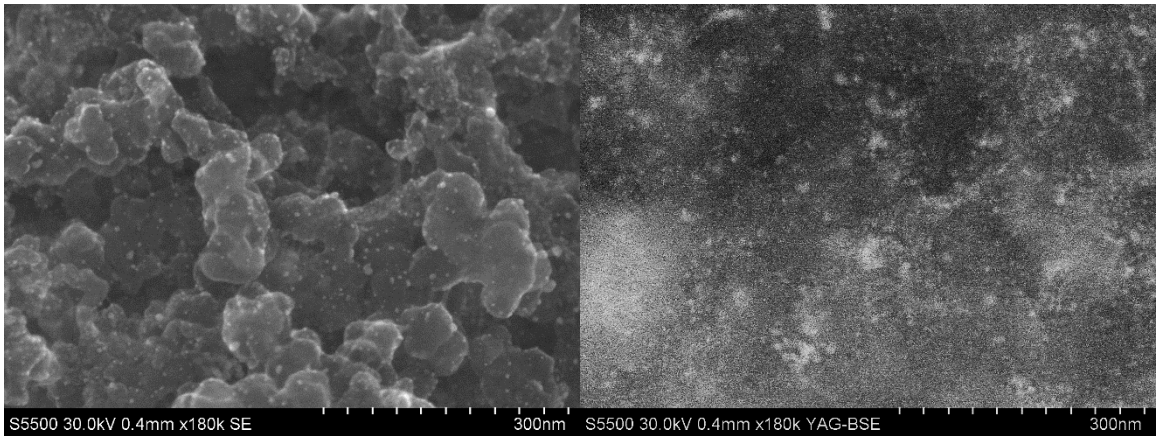

FIGURE 68: CELL 2 SE AND BSE IMAGE COMPARISON 180K MAGNIFICATION

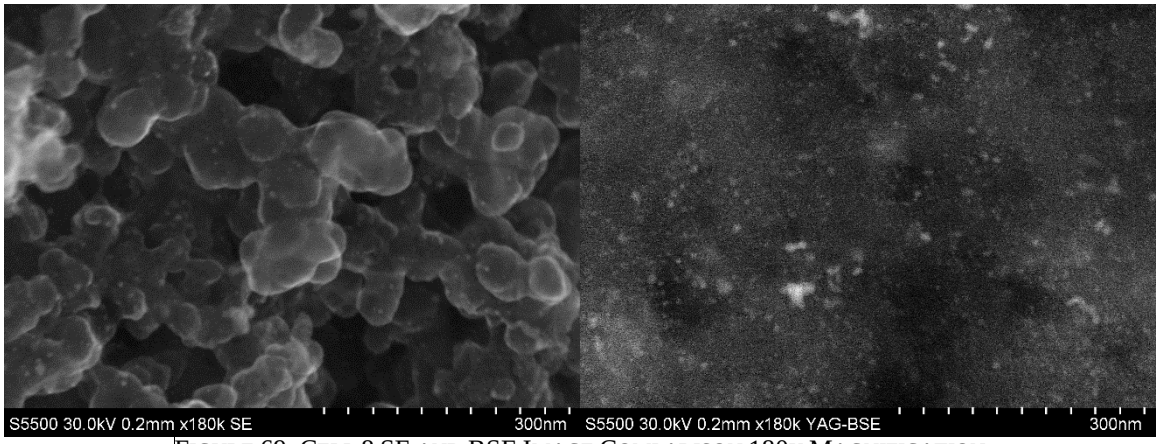

FIGURE 69: CELL 8 SE AND BSE IMAGE COMPARISON 180K MAGNIFICATION

Figure 67, 68, and 69 show more representative images of Cells 1, 2, and 8, respectively, from other areas of the MEAs and at higher magnifications. Cell 1 had a number of very large agglomerations. Cell 8 also showed some large agglomerations, and seemed to have less Pt present than the other cells in most areas, which could be a sign of larger agglomerations elsewhere in the membrane. Conversely, Cell 2 consistently had far more small Pt particles that were dispersed relatively evenly, though there were clearly some larger particles that formed in Cell 2 as well. This is highlighted in the following figure, which compares images from Cells 8 and 2 at 450k magnification.

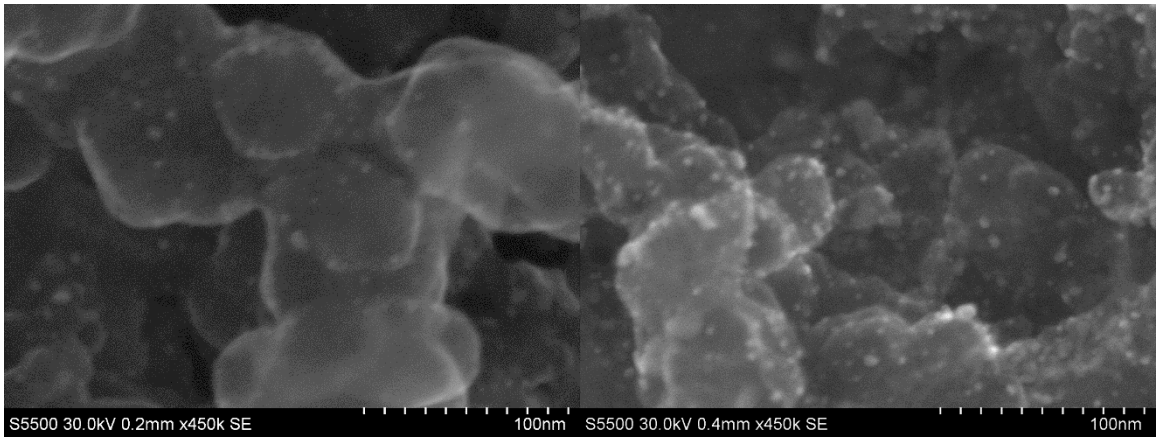

FIGURE 70: CELL 8 (LEFT) AND CELL 2 (RIGHT) SE COMPARISON 450K MAGNIFICATION

The SEM images collected from selected cells in the stack agree with the results of the EKF estimation, which predicted that Cells 1 and 8 had degraded more significantly than Cell 2. This is apparent from the Pt particles seen in the images, in addition to the pitting that was seen throughout both Cells 1 and 8. Again, though the pitting phenomena may not directly correlate to a loss in the EMSA of the membranes, they are further indications as to why Cells 1 and 8 would perform more poorly than Cell 2. As such, the EMSA estimations should be viewed as an indicator of the overall health of the MEA, rather than just as a direct membrane parameter.

Chapter VI: Conclusions

Though many advancements have been made with PEM fuel cells in the last few years, many technical challenges still remain before this technology can reach its full potential. The major hurdles that still remain are in the areas of control, particularly of humidity levels in the stack, and MEA durability. To combat these issues, control systems need to be designed that can properly account for the changing operating conditions across the stack to optimize system performance and minimize membrane wear. A necessary prerequisite to such control designs are accurate dynamic models that can operate in real time. The intent of this work was to advance reduced order modeling methods for PEM fuel cells to fulfill this requirement, as well as to develop state estimation techniques to dynamically tune stack voltage models and track the health of membranes in the stack.

This study focused on three major tasks. Firstly, the development and experimental validation of a physics-based, real-time model that incorporates voltage, temperature, and humidity dynamics was created. Particularly, the cathode water dynamics were focused on as experimental validation of models for this key operating condition had not been published in the literature previously. Secondly, this study sought to improve the fundamental understanding of the distribution of operating conditions in the stack through analytical solutions of the energy and mass balance equations to create methods to improve modeling accuracy and computation times. And finally, a method to track the health of MEAs in the stack was created to provide a means to account for long-term aging effects in fuel cell stacks.

CONTROL ORIENTED FUEL CELL MODEL DEVELOPMENT AND VALIDATION

For optimal fuel cell control, it is important to understand the dynamic behavior of the operating conditions and stack output in response to changes in the applied load and stack inputs. A particular concern for PEM fuel cells has been humidity control, as both low and high humidity operation have major negative effects on stack performance. Accurate flooding prediction is especially important because cathode flooding is a major issue during high load operation for deployed systems. To model this system in a way that could be used for real time control, a reduced order model based on conservation of energy and species in the stack was created. Initially, a fully lumped (i.e. one CV) model was implemented. However, through the course of the study it was found that the distribution of vapor in the stack was a significant consideration as this model was incapable of predicting the stack vapor concentration at the outlet.

To rectify this issue, a multi-CV modeling approach was adopted in which a series of six, evenly sized CVs were used to represent the cathode channel. Six CVs were chosen for use through a trial-and-error study, which suggested that this level of discretization provided a good combination of accuracy and computational expense. As the outlet of one CV acts as the inlet of the subsequent CV, the distributed model is able to compensate for the accumulation of water vapor towards the end of the channel due to water generation and advection downstream. Experimental validation showed that this technique greatly improved the accuracy of the relative humidity and voltage simulations, particularly when the stack was subjected to high loads. This model allow will for improved control designs for PEM fuel cells as it can predict both the low humidity conditions at the stack inlet and

flooding conditions at the stack outlet simultaneously and can be processed fast enough for real-time control applications.

System Analysis and Model Optimization

The modeling results from the first set of experiments showed that the distribution of water vapor in the stack was not linear in many cases. As such, evenly sized CVs may not lead to the most efficient use of computational power. Recall, the intent of this research is not only to create an accurate system model, but to do so in a way that can be used for real-time control. Therefore, the model should be optimized to limit the computational expense as much as possible while satisfying any accuracy requirements of the application in question. Additionally, while six CVs seemed to work well for our 30 cell system, this number cannot simply be scaled up for much larger stacks that can have upwards of 300 cells because the computational expense and number of system states would be too much for an onboard controller. To combat these issues, this research sought to develop techniques to size models appropriately for various systems.

Given the strong dependency of the relative humidity on the local temperature, the thermal model was addressed first. Starting from energy conservation principles in the cathode channel, including convection to the fuel cell body, heat generation, and advection through the channel, an analysis was performed to find the profile of the temperature along the cathode channel. Based on the temperature profile and a critical temperature difference between the model and the profile, an algorithm was created to define the CV lengths in the model. Since the temperature profile was non-linear, the resulting CVs were unevenly

sized, with more and smaller CVs located in the section of the stack with the largest gradients in the temperature with respect to the channel location.

Previously, the model contained individual temperature states for all six CVs because of the close tie to the relative humidity. However, the analysis of the energy equation revealed that in the flow scenarios required for our test station, convection to the fuel cell body was the dominant mode of heat transfer, and the temperature of the gases in the channel would rise to the fuel cell body temperature very quickly (within ~25% of the length of the first channel). Therefore, to reduce the computational intensity of the model, the eight temperature states (fuel cell body, anode channel, and six for the cathode channel) were reduced to a single temperature for the fuel cell body. This reduced the computation time of the model by as much as 80% and was shown to still yield accurate relative humidity estimations.

An analysis of the vapor conservation equation was performed as well. As was the case with the energy equation, the intent was to find an analytical result for the relative humidity profile in the cathode channel and use this knowledge to properly size CVs. This analysis started from the mass conservation equation for vapor in the cathode channel, including diffusion and electro-osmotic drag through the membrane, vapor generation, and bulk flow through the channel. This analysis was done in a generic fashion, such that the profile could vary freely in response to changing flow rates, anode vapor concentrations, and applied currents. Again, the resulting equation was shown to be nonlinear, which would lead to uneven CV sizes to optimize computational efforts.

Additionally, the value of this analysis was shown by using the RH profile to augment a one CV PEM fuel cell model. Previously, it had been shown that the one CV model could not accurately predict the vapor dynamics at the stack outlet as it could not account for the accumulation of vapor towards the end of the channel, particularly with high load operation. However, using the profile information, the difference between the vapor content calculated by the one CV model (weighted average of the profile) and profile value at the end of the channel was calculated and added to the one CV model prediction. Doing this led to very accurate results for the outlet dewpoint calculation, even during the peak load periods. In this way, it was shown that a one CV model could be used for accurate flooding predictions if knowledge of the RH profile in the channel is properly applied. In cases where very low computational expense is needed, a fully lumped system model could still yield accurate flooding predictions using this method.

EKF MEMBRANE STATE ESTIMATIONS

The experiments conducted for this research spanned a long period of time, and the membranes were often unused in between experiments. When experiments were performed, it was often found that the state of the membranes had changed significantly since the previous set of experiments. Early on in the course of this research, this was addressed using a general parameter tuning method in the MATLAB/Simulink package. However, continued deterioration of the membranes from the time that this tuning was executed to subsequent experiments suggested that a more robust and physically significant method would be preferred. Additionally, the development of such a technique would be

an asset to PEM fuel cell research in general as membrane state of health prognostics has become an area of increasing interest in the field.

To this end, an Extended Kalman Filter (EKF) was applied to the six CV model to estimate the effective membrane surface area (EMSA) of each cell in the stack. The EMSA was selected for estimation because this is often cited as the major contributor to the loss of membrane performance in these systems. A series of experiments based on standard drive test cycles was conducted to test the EKF implementation and verify the accuracy of the resulting voltage predictions. The EKF accurately identified the cells that had the worst performance during the tests. It also showed that cells closer to the stack inlet deteriorated more than cells at the outlet. This could be due to the fact that the OCV and ohmic resistance at the inlet cells would generally be higher during operation because of the drop in pressure due to the flow of reactants and lower local humidity, respectively. These conditions have been cited as leading to faster deterioration in the EMSA of membrane electrolyte assemblies. Further investigation would be necessary to corroborate these results.

SEM analysis of select membranes from the stack was used to validate the EKF estimator. It was shown that the cells predicted to have a low EMSA from the EKF process (1 and 8) had a number of physical characteristics that would lead to poor performance. Large agglomerations and pits formed in both these cells, and there were far fewer small Pt particles than were seen in Cell 2, which was predicted to have a relatively high EMSA.

The method developed here could be used to inform prognostics models of the rate of membrane deterioration to lead to more accurate time-to-failure predictions. Also, the

ability of the EKF for identify problematic cells during operation shows that this could be used to flag membranes for replacement or other maintenance procedures. Furthermore, the EKF can be easily extended to estimate other membrane parameters that are thought to be important to the state of health of the system.

FUTURE WORK

Dynamic System Modeling

Though significant advances in modeling of vapor dynamics resulted from this research, there are still more areas that could be improved to increase the overall usefulness of control-oriented models for PEM fuel cells. Firstly, liquid water modeling, both in the channel and potentially in the membranes themselves, would be a useful addition. The experiments that were performed for this research had to be run with a low inlet RH to avoid flooding the RH sensors at the stack outlet. Furthermore, the control goal has been to completely avoid flooding of the end cells up to this point. However, it is unclear whether this would in fact lead to the optimal performance of the stack or even of the end cells. It is possible that the formation of a limited amount of liquid would in fact improve the performance of the end cells, and small liquid volumes would not lead to significant membrane blockages or voltage losses. As such, an investigation should be carried out as to what the truly optimal operating conditions are, and how to control liquid levels effectively. This would require considerations of the liquid mobility, droplet formation, and evaporation mechanisms in the system. Though this would be a significant

undertaking, it could loosen the current control objective for water in the stack and lead to better performance overall.

Secondly, though algorithms have been developed for optimizing CV sizes in the model, this technique has not yet been validated. Ideally, as the RH profile in the system is highly dependent on the load and inlet flow rate, the CV sizes would be able to vary dynamically to remain optimal in all cases. This implies that the model would incorporate moving boundaries, with the target location of the boundaries being defined by the optimal CV lengths calculated by the algorithm presented in Chapter IV. Though it seems that this may not yield a significant improvement in the accuracy of the model for the 2kW system tested for this research, this method could be extremely advantageous for larger stacks such as those used for automotive applications where accuracy is desired but controller sizes are limited.

Membrane State Estimates and Prognostics

The work shown in Chapter V offers a physically relevant voltage tuning method that also yields good estimates of the state of health of the membranes in the system. However, this could potentially be improved by adding considerations of the double layer capacitance (DLC) to the model. This would reduce the influence of the load dynamics on the value of the state estimate by accounting for the natural lag of the activation and concentration overpotentials to swift load changes. Also, more membrane parameters could be included in the EKF estimations, as number of mechanisms for changes to the membrane thickness, GDL effectiveness, etc. have been identified in literature, and could

have a significant impact on performance. It should be noted though that the estimation of any membrane parameters would be contingent upon the accuracy of the model dynamics to some degree. Therefore, the DLC or any other dynamic effects that are considered to be significant to the dynamics of the system would need to be considered first to yield more reliable results. It could also be beneficial to implement a low pass filter on the residual for the EKF process to limit the effect of inaccurately modeled fast dynamics.

References

[1] S. Peighambardoust, S. Rowshanzamir and M. Amjadi, "Review of the proton exchange membranes for fuel cell applications," *International Journal of Hydrogen Energy,* vol. 35, no. 17, pp. 9349-9384, 2010.

[2] C. K. Dyer, "Fuel cells for portable applications," *Journal of Power Sources,* vol. 106, no. 1, pp. 31-34, 2002.

[3] Y. Wang, K. S. Chen, J. Mishler, S. C. Cho and X. C. Adroher, "A review of polymer electrolyte membrane fuel cells: technology, applications, and needs on fundamental research," *Applied Energy,* vol. 88, no. 4, pp. 981-1007, 2011.

[4] C. Thomas, "Fuel cell and battery electric vehicles compared," *International Journal of Hydrogen Energy,* vol. 34, no. 15, pp. 6005-6020, 2009.

[5] E. Patterson, "Better Fuel Cell Membrane Materials," 1663 Science and Technology Magazine | Los National Alamos Laboratory, November 2010. [Online]. Available: http://www.lanl.gov/science/1663/november2010/story8.shtml.

[6] N. Rauh, T. Franke and J. F. Krems, "Understanding the impact of electric vehicle driving experience on range anxiety," *Human Factors: The Journal of the Human Factors and Ergonomics Society,* p. 0018720814546372, 2014.

[7] J. Neubauer and E. Wood, "The impact of range anxiety and home, workplace, and public charging infrastructure on simulated battery electric vehicle lifetime utility," *Journal of Power Sources,* vol. 257, pp. 12-20, 2014.

[8] W. Sierzchula, S. Bakker, K. Maat and B. van Wee, "The influence of financial incentives and other socio-economic factors on electric vehicle adoption," *Energy Policy,* vol. 68, pp. 183-194, 2014.

[9] "Hyundai Tucson Fuel Cell," Hyundai Motor America, 2015. [Online]. Available: https://www.hyundaiusa.com/tucsonfuelcell/. [Accessed June 2015].

[10] M. Pehnt and S. Ramesohl, "Fuel cells for distributed power: benefits, barriers and perspectives".

[11] A. Elgowainy, M. Wang and others, "Fuel cycle comparison of distributed power generation technologies.," 2008.

[12] K.-A. Adamson, "Are Fuel Cells the Future for Distributed Generation?," Cleantech , September 2008. [Online]. Available: http://www.cleantechinvestor.com/portal/fuel-cells/1368-are-fuel-cells-the-future-for-distributed-generation.html. [Accessed June 2015].

[13] O. Egbue and S. Long, "Barriers to widespread adoption of electric vehicles: An analysis of consumer attitudes and perceptions," *Energy Policy,* vol. 48, pp. 717-729, 2012.

[14] M. Lifsher, "California to spend $20 million on building part of 'hydrogen highway'," LA Times, 22 February 2015. [Online]. Available: Conversely, low membrane humidity increases membrane resistance, causing reduced

efficiency due to ohmic losses. Membrane dehydration can also cause hot spots and irreparable damage to the membrane itself [9, 10] with high currents. Given these issues, co. [Accessed June 2015].

[15] M. Lee, "Hydrogen Highway inches closer," The San Diego Union-Tribune, 29 August 2014. [Online]. Available: http://www.utsandiego.com/news/2014/aug/29/california-opens-hydrogen-highway/. [Accessed June 2015].

[16] K. Hall-Geisler, "Honda's latest fuel cell vehicle has an improved power train and more room for passengers," Popular Science, 13 January 2015. [Online]. Available: http://www.popsci.com/2015-detroit-auto-show-honda-fcv-concept-more-power-more-space. [Accessed June 2015].

[17] J. Cobb, "Toyota Announces East Coast 'Hydrogen Highway' for 'Mirai" FCV," hybridCARS.com, 16 November 2014. [Online]. Available: http://www.hybridcars.com/toyota-announces-east-coast-hydrogen-highway-for-mirai-fcv/. [Accessed June 2015].

[18] C.-J. Yang, "An impending platinum crisis and its implications for the future of the automobile," *Energy Policy,* vol. 37, no. 5, pp. 1805-1808, 2009.

[19] C. He, S. Desai, G. Brown and S. Bollepalli, "PEM fuel cell catalysts: Cost, performance, and durability," 2005.

[20] B. D. James and A. B. Spisak, "Mass Production Cost Estimation of Direct H2 PEM Fuel Cell Systems for Transportation Applications: 2012 Update," 2012.

[21] Fuel Cell Technical Team, "Fuel Cell Technical Team Roadmap," U.S. DRIVE Partnership, 2013.

[22] M. Paquin and L. G. Fréchette, "Understanding cathode flooding and dry-out for water management in air breathing PEM fuel cells," *Journal of Power Sources,* vol. 180, no. 1, pp. 440-451, 2008.

[23] A. Bazylak, "Liquid water visualization in PEM fuel cells: a review," *International Journal of Hydrogen Energy,* vol. 34, no. 9, pp. 3845-3857, 2009.

[24] Z. Qi and A. Kaufman, "Improvement of water management by a microporous sublayer for PEM fuel cells," *Journal of Power Sources,* vol. 109, no. 1, pp. 38-46, 2002.

[25] K. Wong, K. Loo, Y. Lai, S.-C. Tan and K. T. Chi, "A theoretical study of inlet relative humidity control in PEM fuel cell," *international journal of hydrogen energy,* vol. 36, no. 18, pp. 11871-11885, 2011.

[26] F. N. Büchi and S. Srinivasan, "Operating proton exchange membrane fuel cells without external humidification of the reactant gases fundamental aspects," *Journal of the Electrochemical Society,* vol. 144, no. 8, pp. 2767-2772, 1997.

[27] M. V. Williams, H. R. Kunz and J. M. Fenton, "Operation of Nafion{\textregistered}-based PEM fuel cells with no external humidification:

influence of operating conditions and gas diffusion layers," *Journal of Power Sources,* vol. 135, no. 1, pp. 122-134, 2004.

[28] J. Zhang, Y. Tang, C. Song, X. Cheng, J. Zhang and H. Wang, "PEM fuel cells operated at 0% relative humidity in the temperature range of 23-120 C," *Electrochimica Acta,* vol. 52, no. 15, pp. 5095-5101, 2007.

[29] A. Shah, K. Luo, T. Ralph and F. Walsh, "Recent trends and developments in polymer electrolyte membrane fuel cell modelling," *Electrochimica Acta,* vol. 56, no. 11, pp. 3731-3757, 2011.

[30] F. De Bruijn, V. Dam and G. Janssen, "Review: durability and degradation issues of PEM fuel cell components," *Fuel cells,* vol. 8, no. 1, p. 3, 2008.

[31] A. Collier, H. Wang, X. Z. Yuan, J. Zhang and D. P. Wilkinson, "Degradation of polymer electrolyte membranes," *International Journal of Hydrogen Energy,* vol. 31, no. 13, pp. 1838-1854, 2006.

[32] H. Tang, S. Peikang, S. P. Jiang, F. Wang and M. Pan, "A degradation study of Nafion proton exchange membrane of PEM fuel cells," *Journal of Power Sources,* vol. 170, no. 1, pp. 85-92, 2007.

[33] W. Schmittinger and A. Vahidi, "A review of the main parameters influencing long-term performance and durability of PEM fuel cells," *Journal of Power Sources,* vol. 180, no. 1, pp. 1-14, 2008.

[34] X. Yang, F. Zhang, A. Lubawy and C. Wang, "Visualization of liquid water transport in a PEFC," *Electrochemical and Solid-State Letters,* vol. 7, no. 11, pp. A408--A411, 2004.

[35] F. Zhang, X. Yang and C. Wang, "Liquid Water Removal from a Polymer Electrolyte Fuel Cell," *Journal of The Electrochemical Society,* vol. 153, p. A225, 2006.

[36] U. Pasaogullari and C. Wang, "Liquid water transport in gas diffusion layer of polymer electrolyte fuel cells," *Journal of The Electrochemical Society,* vol. 151, no. 3, pp. A399--A406, 2004.

[37] Y. Wang, S. Basu and C.-Y. Wang, "Modeling two-phase flow in PEM fuel cell channels," *Journal of Power Sources,* vol. 179, no. 2, pp. 603-617, 2008.

[38] D. Chen and H. Peng, "A thermodynamic model of membrane humidifiers for PEM fuel cell humidification control," *Journal of dynamic systems, measurement, and control,* vol. 127, no. 3, pp. 424-432, 2005.

[39] S. Ahmed, J. Kopasz, R. Kumar and M. Krumpelt, "Water balance in a polymer electrolyte fuel cell system," *Journal of Power Sources,* vol. 112, no. 2, pp. 519-530, 2002.

[40] H. Li, Y. Tang, Z. Wang, Z. Shi, S. Wu, D. Song, J. Zhang, K. Fatih, J. Zhang, H. Wang and others, "A review of water flooding issues in the proton exchange membrane fuel cell," *Journal of Power Sources,* vol. 178, no. 1, pp. 103-117, 2008.

[41] G. Lin and T. Van Nguyen, "A two-dimensional two-phase model of a PEM fuel cell," *Journal of The Electrochemical Society,* vol. 153, no. 2, pp. A372--A382, 2006.

[42] V. Gurau, H. Liu and S. KakaÃ§, "Two-dimensional model for proton exchange membrane fuel cells," *AIChE Journal,* vol. 44, no. 11, pp. 2410-2422, 1998.

[43] S. Um, C.-Y. Wang and K. Chen, "Computational fluid dynamics modeling of proton exchange membrane fuel cells," *Journal of the Electrochemical society,* vol. 147, no. 12, pp. 4485-4493, 2000.

[44] R. M. Rao, D. Bhattacharyya, R. Rengaswamy and S. Choudhury, "A two-dimensional steady state model including the effect of liquid water for a PEM fuel cell cathode," *Journal of Power Sources,* vol. 173, no. 1, pp. 375-393, 2007.

[45] Y. Shan and S.-Y. Choe, "A high dynamic PEM fuel cell model with temperature effects," *Journal of Power Sources,* vol. 145, no. 1, pp. 30-39, 2005.

[46] L. You and H. Liu, "A two-phase flow and transport model for the cathode of PEM fuel cells," *International Journal of Heat and Mass Transfer,* vol. 45, no. 11, pp. 2277-2287, 2002.

[47] H. Ju, H. Meng and C.-Y. Wang, "A single-phase, non-isothermal model for PEM fuel cells," *International Journal of Heat and Mass Transfer,* vol. 48, no. 7, pp. 1303-1315, 2005.

[48] F.-B. Weng, C.-Y. Hsu and C.-W. Li, "Experimental investigation of PEM fuel cell aging under current cycling using segmented fuel cell," *international journal of hydrogen energy,* vol. 35, no. 8, pp. 3664-3675, 2010.

[49] T. Nguyen and R. White, "A water and heat management model for Proton-Exchange-Membrane fuel cells," *Journal of the Electrochemical Society,* vol. 140, no. 8, pp. 2178-2186, 1993.

[50] D. Di Penta, K. Bencherif, M. Sorine and Q. Zhang, "A reduced fuel cell stack model for control and fault diagnosis," *Journal of fuel cell science and technology,* vol. 3, no. 4, pp. 384-388, 2006.

[51] C. Wang, M. Nehrir and S. Shaw, "Dynamic models and model validation for PEM fuel cells using electrical circuits," *Energy Conversion, IEEE Transactions on,* vol. 20, no. 2, pp. 442-451, 2005.

[52] A. J. del Real, A. Arce and C. Bordons, "Development and experimental validation of a PEM fuel cell dynamic model," *Journal of Power Sources,* vol. 173, no. 1, pp. 310-324, 2007.

[53] J. Pukrushpan, "Modeling and control of fuel cell systems and fuel processors," *UMI Dissertations,* 2003.

[54] J. C. Amphlett, R. Baumert, R. F. Mann, B. A. Peppley, P. R. Roberge and T. J. Harris, "Performance modeling of the Ballard Mark IV solid polymer

electrolyte fuel cell I. Mechanistic model development," *Journal of the Electrochemical Society,* vol. 142, no. 1, pp. 1-8, 1995.

[55] C. Kunusch, P. F. Puleston, M. A. Mayosky and J. J. Mor{\'e}, "Characterization and experimental results in PEM fuel cell electrical behaviour," *International Journal of Hydrogen Energy,* vol. 35, no. 11, pp. 5876-5881, 2010.

[56] K. Tüber, D. Pócza and C. Hebling, "Visualization of water buildup in the cathode of a transparent PEM fuel cell," *Journal of Power Sources,* vol. 124, no. 2, pp. 403-414, 2003.

[57] E. Endoh, S. Terazono, H. Widjaja and Y. Takimoto, "Degradation study of MEA for PEMFCs under low humidity conditions," *Electrochemical and Solid-State Letters,* vol. 7, no. 7, pp. A209--A211, 2004.

[58] D. Chen and H. Peng, "Modeling and simulation of a PEM fuel cell humidification system," in *American Control Conference, 2004. Proceedings of the 2004*, 2004.

[59] S. D. Knights, K. M. Colbow, J. St-Pierre and D. P. Wilkinson, "Aging mechanisms and lifetime of PEFC and DMFC," *Journal of power sources,* vol. 127, no. 1, pp. 127-134, 2004.

[60] A. Debenjak, M. Ga{\v{s}}perina and J. Petrov{\v{c}}i{\v{c}}a, "On-line Tracking of Fuel Cell System Impedance Using Extended Kalman Filter," *CHEMICAL ENGINEERING,* vol. 33, 2013.

[61] I. H. Kazmi and A. I. Bhatti, "Parameter estimation of proton exchange membrane fuel cell system using sliding mode observer," *International Journal of Innovative Computing, Information and Control,* vol. 8, no. 7B, pp. 5137-5148, 2012.

[62] X. Zhang and P. Pisu, "An Unscented Kalman Filter based on-line Diagnostic approach for PEM fuel cell Flooding," *International Journal of Prognostics and Health Management,* vol. 5, no. 1, 2014.

[63] O. Bethoux, M. Hilairet and T. Azib, "A new on-line state-of-health monitoring technique dedicated to PEM fuel cell," in *Industrial Electronics, 2009. IECON'09. 35th Annual Conference of IEEE*, 2009.

[64] M. Jouin, R. Gouriveau, D. Hissel, M. C. P{\'e}ra and N. Zerhouni, "PEMFC aging modeling for prognostics and health assessment," *IFAC-PapersOnLine,* vol. 48, no. 21, pp. 790-795, 2015.

[65] X. Zhang and P. Pisu, "An unscented kalman filter based approach for the health-monitoring and prognostics of a polymer electrolyte membrane fuel cell," *a a,* vol. 1, p. 1, 2012.

[66] A. J. Headley, B. Hadisujoto, D. Chen and T. Moon, "Development and Validation of a Dynamic Thermal Model for a Polymer Electrolyte Membrane Fuel Cell," in *ASME 2013 11th International Conference on Fuel Cell Science, Engineering and Technology collocated with the ASME 2013 Heat Transfer*

Summer Conference and the ASME 2013 7th International Conference on Energy Sustainability., Minneapolis, MN, 2013.

[67] A. J. Headley, "Dynamic subdivided relative humidity model of a polymer electrolyte membrane fuel cell," UT Digital Repository, 2013.

[68] I. S. Hussaini and C.-Y. Wang, "Visualization and quantification of cathode channel flooding in PEM fuel cells," *Journal of Power Sources,* vol. 2, no. 187, pp. 444-451, 2009.

[69] J. T. Pukrushpan, Control of fuel cell power systems: principles, modeling, analysis and feedback design, Springer, 2004.

[70] S. Dutta, S. Shimpalee and J. Van Zee, "Numerical prediction of mass-exchange between cathode and anode channels in a PEM fuel cell," *International Journal of Heat and Mass Transfer,* vol. 44, no. 11, pp. 2029-2042, 2001.

[71] R. T. Meyer and B. Yao, "Modeling and simulation of a modern PEM fuel cell system," *Proceedings of Fuel Cell,* pp. 19-21, 2006.

[72] J. d. J. Rubio, "Stable and optimal controls of a proton exchange membrane fuel cell," *International Journal of Control,* vol. 87, no. 11, pp. 2338-2347, 2014.

[73] J. d. J. Rubio and A. G. Bravo, "Optimal Control of a PEM Fuel Cell for the Inputs Minimization," *Mathematical Problems in Engineering,* vol. 2014, 2014.

[74] Z. Wang, C. Wang and K. Chen, "Two-phase flow and transport in the air cathode of proton exchange membrane fuel cells," *Journal of Power Sources,* vol. 94, no. 1, pp. 40-50, 2001.

[75] D. Chen and H. Peng, "A thermodynamic model of membrane humidifiers for PEM fuel cell humidification control".

[76] A. J. Headley, V. Yu, R. Borduin, D. Chen and W. Li, "Development and Experimental Validation of a Physics-based PEM Fuel Cell Model for Cathode Humidity Control Design," *IEEE Journal of Mechatronics,* 2015.

[77] Z. Zhang, L. Jia, X. Wang and L. Ba, "Effects of inlet humidification on PEM fuel cell dynamic behaviors," *International Journal of Energy Research,* vol. 35, no. 5, pp. 376-388, 2011.

[78] J. Pukrushpan, A. Stefanopoulou and H. Peng, "Control of Fuel Cell Power Systems," *Springer-Verlag, Telos,* 2004.

[79] T. E. Springer, T. Zawodzinski and S. Gottesfeld, "Polymer electrolyte fuel cell model," *Journal of the Electrochemical Society,* vol. 138, no. 8, pp. 2334-2342, 1991.

[80] Vaisala, "Humidity Conversion Formulas: Calculation Formulas for Relative Humidity," Vaisala Oyj, Helsinki, Finland, 2012.

[81] G. Escobedo, K. Raiford, G. S. Nagarajan and K. E. Schwiebert, "Strategies for mitigation of PFSA polymer degradation in PEM fuel cells," *ECS Transactions,* vol. 1, no. 8, pp. 303-311, 2006.

[82] D. Liu and S. Case, "Durability study of proton exchange membrane fuel cells under dynamic testing conditions with cyclic current profile," *Journal of Power Sources,* vol. 162, no. 1, pp. 521-531, 2006.

[83] H. Nakayama, T. Tsugane, M. Kato, Y. Nakagawa and M. Hori, "Fuel cell seminar abstracts," *Courtesy Associates, Hawaii,* 2006.

[84] D. Seo, J. Lee, S. Park, J. Rhee, S. W. Choi and Y.-G. Shul, "Investigation of MEA degradation in PEM fuel cell by on/off cyclic operation under different humid conditions," *International Journal of Hydrogen Energy,* vol. 36, no. 2, pp. 1828-1836, 2011.

[85] J. Healy, C. Hayden, T. Xie, K. Olson, R. Waldo, M. Brundage, H. Gasteiger and J. Abbott, "Aspects of the chemical degradation of PFSA ionomers used in PEM fuel cells," *Fuel cells,* vol. 5, no. 2, pp. 302-308, 2005.

[86] J. Yu, T. Matsuura, Y. Yoshikawa, M. N. Islam and M. Hori, "Lifetime behavior of a PEM fuel cell with low humidification of feed stream," *Physical Chemistry Chemical Physics,* vol. 7, no. 2, pp. 373-378, 2005.

[87] R. L. Borup, J. R. Davey, F. H. Garzon, D. L. Wood and M. A. Inbody, "PEM fuel cell electrocatalyst durability measurements," *Journal of Power Sources,* vol. 163, no. 1, pp. 76-81, 2006.

[88] M. F. Mathias, R. Makharia, H. A. Gasteiger, J. J. Conley, T. J. Fuller, C. J. Gittleman, S. S. Kocha, D. P. Miller, C. K. Mittelsteadt, T. Xie and others, "Two fuel cell cars in every garage," *Electrochem. Soc. Interface,* vol. 14, no. 3, pp. 24-35, 2005.

[89] R. Nicolas, "The different driving cycles," Car-Engineer.com, 5 January 2013. [Online]. Available: http://www.car-engineer.com/the-different-driving-cycles/.

[90] "2015 Toyota Corolla - Features & Specs," Edmunds.com, [Online]. Available: http://www.edmunds.com/toyota/corolla/2015/features-specs/. [Accessed October 2015].

[91] "Vehicle Coefficient of Drag List," Ecomodder.com, [Online]. Available: http://ecomodder.com/wiki/index.php/Vehicle_Coefficient_of_Drag_List. [Accessed October 2015].

[92] "Road Loads," thecartech.com, [Online]. Available: http://www.thecartech.com/subjects/auto_eng/Road_loads.htm. [Accessed October 2015].

[93] E. Guilminot, A. Corcella, M. Chatenet, F. Maillard, F. Charlot, G. Berthom{\'e}, C. Iojoiu, J.-Y. Sanchez, E. Rossinot and E. Claude, "Membrane and active layer degradation upon PEMFC steady-state operation I. Platinum dissolution and redistribution within the MEA," *Journal of The Electrochemical Society,* vol. 154, no. 11, pp. B1106--B1114, 2007.

[94] J. Xie, D. L. Wood, K. L. More, P. Atanassov and R. L. Borup, "Microstructural changes of membrane electrode assemblies during PEFC durability testing at high humidity conditions," *Journal of The Electrochemical Society,* vol. 152, no. 5, pp. A1011--A1020, 2005.

[95] P. Ferreira, Y. Shao-Horn, D. Morgan, R. Makharia, S. Kocha, H. Gasteiger and others, "Instability of Pt/ C electrocatalysts in proton exchange membrane fuel cells a mechanistic investigation," *Journal of The Electrochemical Society,* vol. 152, no. 11, pp. A2256--A2271, 2005.

[96] M. W. Fowler, R. F. Mann, J. C. Amphlett, B. A. Peppley and P. R. Roberge, "Incorporation of voltage degradation into a generalised steady state electrochemical model for a PEM fuel cell," *Journal of Power Sources,* vol. 106, no. 1, pp. 274-283, 2002.

[97] J. R. Martins, P. Sturdza and J. J. Alonso, "The complex-step derivative approximation," *ACM Transactions on Mathematical Software (TOMS),* vol. 29, no. 3, pp. 245-262, 2003.

[98] L. I. Cerviño and T. R. Bewley, "On the extension of the complex-step derivative technique to pseudospectral algorithms," *Journal of Computational Physics,* vol. 187, no. 2, pp. 544-549, 2003.

[99] T. Patterson, "Fuel cell technology topical conference proceedings," in *AIChE Spring National Meeting, New York,* 2002.

[100] P. Yu, M. Pemberton and P. Plasse, "PtCo/C cathode catalyst for improved durability in PEMFCs," *Journal of Power Sources,* vol. 144, no. 1, pp. 11-20, 2005.

[101] A. J. Headley, "Dynamic subdivided relative humidity model of a polymer electrolyte membrane fuel cell," 2013.

[102] A. J. Headley and D. Chen, "Critical Control Volume Sizing For Improved Transient Thermal Modeling Of Pem Fuel Cells," *International Journal of Hydrogen,* no. 10.1016/j.ijhydene.2014.12.123, 2015.

[103] A. J. Headley and D. Chen, "Control Oriented Discretized Cathode Control Volume Method for Improved PEM Fuel Cell Modeling," in *ASME 2015 13th International Conference on Fuel Cell Science, Engineering and Technology collocated with the ASME 2015 Power Conference, the ASME 2015 9th International Conference on Energy Sustainability and the ASME 2015 Power Conference,* San Diego, CA, 2015.

Vita

Alexander Headley attended West Jessamine High School, Nicholasville, KY. In 2004, he enrolled at the University of Kentucky, Lexington, KY, to pursue a mechanical engineering degree. Upon graduation in 2008, he worked for a few years in the Advanced Technology group at Lexmark International Inc. before enrolling at the University of Texas at Austin in 2011. Here he received his M.S. in 2013 and graduated with a Ph.D. in mechanical engineering in 2016.

Email Address: ajhead2@gmail.com

This dissertation was typed by Alexander John Headley